Soft physics in p+p collisions at $\sqrt{s} = 62.4$ GeV and $\sqrt{s} = 200$ GeV

Atle Jorstad Qviller

University of Oslo
Department of Physics
June 2007

Thesis presented for the degree Master of Science

Acknowlegdements

5 years of studying physics at the University of Oslo is coming to an end, as I am about to hand in my master thesis on high energy nuclear physics. This time has been both challenging and rewarding. I want to express my gratitude for the scientific discussions and the social environment provided by my family, co-students, research group members, the BRAHMS collaboration and in particular my main supervisor Trine Tveter. She has been very helpful during the entire master study and has always pointed me in the right direction when stuck. Also, a big thanks to my co-supervisor Gunnar Løvhøiden for his inspiring speeches about heavy ion physics and its connection with the early universe, which made this subject catch my interest.

Also, a special thanks goes to my skilled, pedagogical and kind research colleague Ionut Cristian Arsene, for his extensive help with the analysis software and for teaching me all those subtle details which make a big difference in the final results.

The more you see the less you know
The less you find out as you go
I knew much more then than I do now

U2, "City of Blinding Lights", first strophe

Contents

1 Introduction

Man has always wondered his origin and the nature of matter surrounding him. The ancient Greeks believed that the entire Cosmos was composed by the fundamental elements fire, water, air and matter, created by the Gods. In the mid-19th century, Dimitri Mendeleev placed all by then known elements into the periodic table, and in the 1890s, many physicists believed that most about nature was known. This belief was gradually shattered by several discoveries. A very notable one occured in 1911, when Ernest Rutherford discovered the atomic nucleus. Later experimentation mapped out a diverse and strange subatomic world, where the everyday "common sense" has stopped to apply, and the dynamics are governed by relativity and quantum mechanics. Today, Man learns about his origin and the inner workings of matter by smashing subatomic entities like elementary particles and heavy ions into each other. The following chapter is a brief summary of motivations, history and current status of a part of this fascinating subject, namely the study of proton and heavy ion collisions.

1.1 Why study collisions between nuclei or protons?

What is the point of colliding nuclei head on at relativistic speeds? There are numerous things we can learn from these experiments that will complement our view of nature. Arguably, the most important are nonperturbative aspects of Quantum Chromodynamics (QCD) [1]. The equations of QCD are unsolved at low energy scales like inside atomic nuclei or any other hadronic matter. This results from the strong coupling constant $\alpha_s(q^2)$ not being constant, instead running as a function of the transferred momentum $|\vec{q}|$ and diverging at low momenta. Although analytically unproven, the result is confinement of colored quarks and gluons into colorless hadrons, easily demonstrated in lattice calculations. For higher energy scales/momenta, the coupling weakens, and quarks and gluons will propagate freely [2]. This is called deconfinement and is in some form believed to happen within a heavy ion collision at sufficiently high energies. Deconfinement is important in at least two astrophysical phenomena: A fraction of a second (10^{-6} to 10^{-4}, literature dependant) after the Big Bang, the energy density was so high that quarks and gluons propagated freely in the universe. Also the enormous pressure within neutron stars will cause quarks to "forget" which hadron they belonged to, so a deconfined state might also exist within remnants of heavy stars. Proton-proton collisions provide a reference for heavy-ion collisions

Accelerator	y_{max}	Max $\sqrt{s_{NN}}$ (GeV)	Projectiles
AGS/BNL	3.4	5	Au, Si
SPS/CERN	6.0	27.5	p+p, Pb+Pb
Sp$\bar{p}$S/CERN	6.9	900	p+$\bar{p}$
ISR/CERN	4.2+4.2	31.5+31.5	p+p
RHIC/BNL	5.4+5.4	250+250, 100+100	p+p, d/Au+Au, Cu+Cu
Tevatron/Fermilab	7.6+7.6	1000+1000	p+$\bar{p}$
LHC/CERN	9.6+9.6	7000+7000, 5400+5400	p+p, Pb+Pb

Table 1.1: Earlier and current hadron and heavy ion accelerators. Note that LHC and RHIC has higher y_{max} and $\sqrt{s_{NN}}$ for proton beams than ion beams

Often represented as a simple system consisting of three valence quarks, our knowledge about the proton is far from complete. While hadron masses can be parametrized using phenomenological constituent quark masses and mass splittings from chromomagnetic spin-spin interaction, hadron masses, excited states or structure cannot yet be calculated from first principles. Proton collisions can be modeled, but the replication of experimental data is far from perfect, even for such an "elementary" reaction. Further experimentation is needed to understand more about proton structure and reaction dynamics. Chapter 2 deals with history, phenomenology and theory of proton collisions. First, however, comes a summary of some of our knowlegde of quarks and gluons and a statement about what this thesis contains.

1.2 Quarks and gluons: A brief summary

In the 1950s and later, a growing "zoo" of strongly interacting elementary particles started appearing in experiments. Today, we recognize them as the members of the $SU(3)_{flavour}$ symmetric baryon decuplet for the $J = \frac{3}{2}$ baryons, baryon octet and singlet for $J = \frac{1}{2}$ and meson octet and singlets for $J = \ 0, 1, ...$states. To bring order in the chaos, Murray Gell-Mann and Georg Zweig proposed the *quark model* in 1963. This model stated that each baryon consisted of three quarks with three possible *flavours*, today known as the *light flavours* u, d and s.

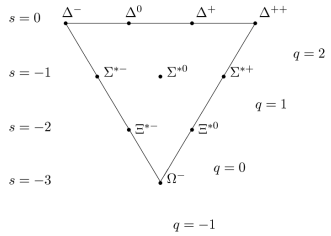

Figure 1.1: The $J = \frac{3}{2}$ baryon decuplet.

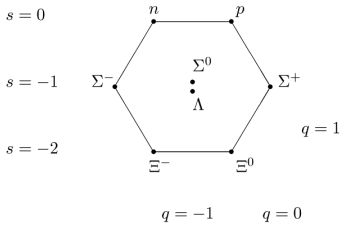

Figure 1.2: The $J = \frac{1}{2}$ baryon octet and singlet.

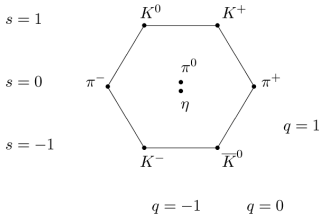

Figure 1.3: The $J = 0$ meson octet and singlet.

A problem appeared soon: Δ^{++} is a baryon with three spin up and three identical quarks inside and this defies the Pauli exclusion principle. Another intrinsic $SU(3)$ degree of freedom, the *color* was therefore proposed in 1965 and turned out to be correct. No free quarks or or other colored particle have ever been seen directly. Evidence for their existence turned up in high energy experiments at SLAC like deep inelastic scattering of electrons onto protons (1969). The electrons scattered electromagnetically like they hit a free, pointlike particle within the proton (Bjorken scaling). Ten years later at DESY, the PETRA experiment recorded three-jet events originating from e^+e^- collisions (both phenomena discussed in [3]. The already known two-jet events were explained as a quark pair created and fragmenting into two jets. The three-jet events were interpreted as the same reaction, with a *gluon* radiated in the final state, fragmenting into the third jet.

$$\begin{aligned} e^+e^- &\rightarrow q\bar{q} \\ e^+e^- &\rightarrow q\bar{q}g \end{aligned}$$

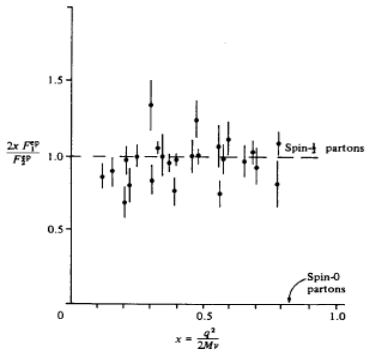

Figure 1.4: Evidence for quarks: Bjorken scaling shows that electrons scatter on pointlike contituents in DIS experiments. Figure from [3].

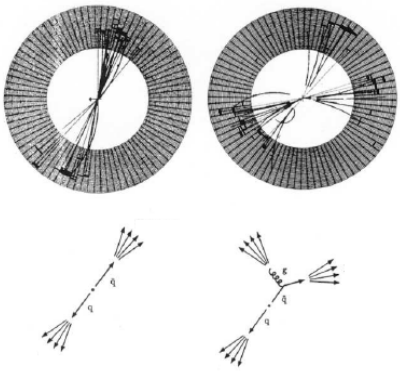

Figure 1.5: Evidence for gluons:3-Jet event ($e^+e^- \rightarrow q\bar{q}g$) recorded by the JADE detector at PETRA,DESY. A 2-Jet event ($e^+e^- \rightarrow q\bar{q}$) is also shown. Figure from [3].

Quarks and gluons are together called *partons*, a term coined by Richard Feynman. Today, 6 quarks are known.

Name	Symbol	Charge	Generation	MS-bar mass (MeV)
Up	u	$\frac{2}{3}$	1	1.5 – 4.0
Down	d	$-\frac{1}{3}$	1	4 – 8
Charm	c	$\frac{2}{3}$	2	1150 – 1350
Strange	s	$-\frac{1}{3}$	2	80 – 130
Top	t	$\frac{2}{3}$	3	170900 ± 1800
Bottom	b	$-\frac{1}{3}$	3	4100 – 4400

Table 1.2: Quark masses from Particle Data Group,except Top, which is from Tevatron Electroweak Working Group [5].

All matter around us are made of up and down valence quarks, together with electrons. The quarks form stable nuclei consisting of neutrons and protons. Up, down and strange quarks hadronize to form long-lived particles that will be seen in many particle detectors. Some ($\pi^{\pm}, K^{\pm}, K^0_L$) have long enough half lives to travel several meters in high energy experiment detectors. Charm and bottom quarks are more massive and therefore short lived. Silicon strip detectors can see the paths of charmed and bottomed hadrons some hundred micrometres before they decay. Top quarks are extremely unstable and will not even hadronize before they decay. Allowed composite particles that have been observed all either consists of three quarks (baryons), three antiquarks (antibaryons) or consists of a quark and an antiquark (mesons). While in theory possible, more complex

parton combinations like pentaquarks and glueballs have not been convincingly detected yet.

1.3 What will be studied within this thesis?

The Run-5 p+p $\sqrt{s}$ = 200 GeV and the Run-6 p+p $\sqrt{s}$ = 62.4 GeV datasets from BRAHMS experiment at RHIC, BNL will be analyzed. Identified particle spectra will be extracted, yields and ratios studied as a function of rapidity and compared with each other and with ISR p+p, SPS p+p and TEVATRON p+$\bar{\text{p}}$ data.

2 Proton - Proton collisions

Before new knowledge about Nature can be gained, it is necessary to understand what is already known and how it was discovered. This chapter reviews theory and phenomenology of the strong interaction and physics at hadron colliders in general. Observable quantities in proton-proton collisions and the string picture of such a collision are also discussed. See Appendix A for a definition of the kinematical quantities used in the discussion.

2.1 Color force and strong nuclear force

To understand a strongly interacting system of quarks and gluons, one must understand the forces between them. The strong nuclear force is the force that binds two nucleons (protons/neutrons) together inside a nucleus. It is the residual (Van der Waals-equivalent) strong interaction, mediated by virtual mesons. Only phenomenological descriptions of the strong nuclear force is possible today, but it can be studied in *lattice* calculations. The fundamental strong interaction is the color force that binds quarks and gluons together, mediated by gluons and described by QCD. QCD and its Lagrangian formalism is described in Appendix C. A phenomenological parametrization from [6] that can be used for the color force is:

$$V(r) = -\frac{4\alpha_s}{3r} + kr \tag{1}$$

where r is the separation between two quarks, α_s is the strong coupling constant and k determines the field energy per unit of separation length ("string tension") which is responsible for the confinement.

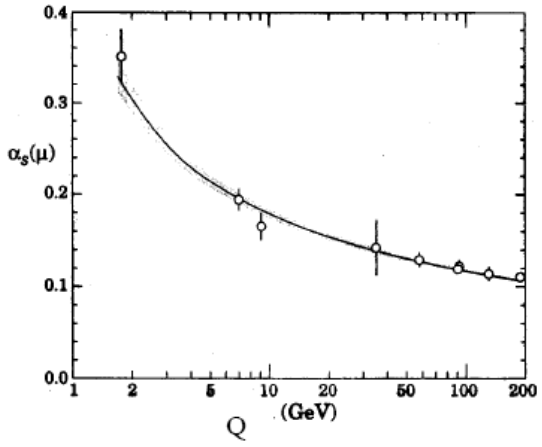

Figure 2.1: α_s as a function of Q. Figure from [3].

2.2 Physics at hadron colliders

To resolve the structure of an object of a given size, radiation with a corresponding length scale must be scattered onto it. A visible light microscope can be used down to the μm scale. X-ray diffraction and electron microscopes have been used to investigate structures at the molecular or atomic length scales. To probe the structure of nuclei, nucleons or the possibly structureless electrons, quarks, and gluons, particle accelerators must be used. For beam energies much larger than the projectile mass, the resolution is inversely proportional to the beam energy:

$$\lambda \sim \frac{\hbar}{E} \tag{2}$$

One of the most important magnifying glasses into the subatomic world today are provided by hadron colliders. Structures down to about 10^{-20} m can be probed at the LHC, and experiments operating today (RHIC, Tevatron) have an order of magnitude worse spatial resolution. These distances correspond to CM energies of TeVs and hundreds of GeVs. Circular accelerators for light particles, like e^+e^-, have high synchrotron radiation losses. This is a consequence of the particles being continuously accelerated towards the center of the circle. Hadron colliders utilizing much heavier (anti)protons are not as much affected and can provide much higher beam energies at a given circumference.

Hadron colliders are thus useful to discover new physics, while lepton colliders are used for precision measurements. Uncertainties at hadron colliders stem from the composite nature of the hadron projectiles. Inside a proton or antiproton, three valence quarks reside, but also virtual quark-antiquark pairs called sea quarks, gluons, photons

etc. A proton can therefore collide with another proton and quark-antiquark annihilation can take place. Gluon fusion can also occur. Valence quarks, sea quarks and gluons carry different amounts of the momentum and the distributions are themselves a function of the total momentum of the hadron [3]. $f(x, Q^2)$ is the probability of a parton to have a momentum fraction x of the hadrons momentum relative to the CM system at a resolution $\lambda = \frac{\hbar}{\sqrt{Q^2}}$. $Q^2 = -q^2$ (DIS terminology) is the squared 4-momentum transfer. A result is that large amounts of the beam energy will not contribute to scatterings, especially hard scatterings as the maxima of distributions are shifted to lower-x for beam momenta (denoted "parton tyranny" by particle physicists).

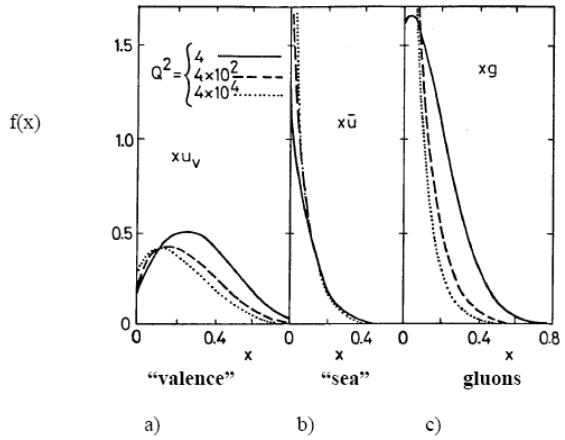

Figure 2.2: Momentum PDFs of a) valence quarks, b) sea quarks, c) gluons. Figure from [3].

Probability distribution functions (PDFs) of the parton momenta within a proton, the structure functions have been measured precisely at DESY. Gluons carry about half the proton momentum, while valence and sea quarks carry nearly all of the remaining.

Particle production in strong interactions is usually divided into two realms: "Hard" processes have momentum transfers $\vec{q}$ much higher than 1 GeV/c. These are successfully described by perturbative QCD (pQCD), as the strong coupling $\alpha_s(q^2)$ is weak enough at these $\vec{q}$ for perturbation theory to be applied. At these $\vec{q}$, quarks and gluons scatter almost as free particles. It is not true that hard processes are calculated from first principles, as both structure functions and fragmentation functions (the probability of a parton to fragment into a given hadron) must be experimentally measured. pQCD is tested to an order of a few percent and is thought to be a correct theory of nature.

The "soft" region consists of particles produced at being $\vec{q}$ below 1 GeV/c where $\alpha_s(q^2)$ is large. This implies that partons in hadrons are tied together by strong gluonic fields. The soft region cannot be treated by pQCD. Effective theories like string fragmentation, Gribov-Regge theory or the Schwinger mechanism can be used for describing

production of $q\bar{q}$ pairs from color field. A treatment of these methods can be found in [2]. They reproduce some, but not all of the data. Statistical models describe quite well yields and the spectrum shapes at low p_T. Even more difficult is the task to join together the hard and soft realms. Next-to-leading order (NLO) pQCD can be used down to about $\vec{q}$ =1 GeV/c, but the replication of experiment is not complete.

2.3 Phenomenology of a p+p collision

The total cross section of proton-proton collisions is a slowly varying function of $\sqrt{s}$:

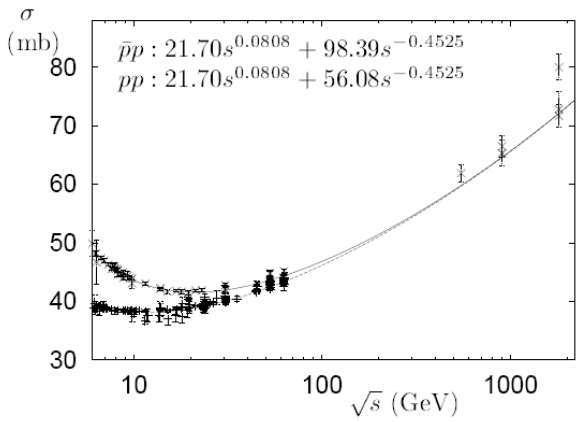

Figure 2.3: p+p (lower curve) and p+$\bar{\text{p}}$ (upper curve) cross sections as a function of $\sqrt{s}$. Figure from [7].

Some of this cross section is elastic, also called nondiffractive, in which protons do not break up or are excited. Most of the cross section is inelastic, where single-diffractive or double-diffractive processes cause one or both, respectively, of the protons to break up or excite. More complex processes can also occur. In the diffractive processes, the force is mediated by an colorless *effective particle* of unclear structure composed by at least two gluons and having the quantum numbers of the vacuum known as a *pomeron* [7]. Also, hard parton scatterings can occur, causing the destruction of the incident protons. Hard scatterings and double-diffractive processes are together called non-single-diffractive (NSD).

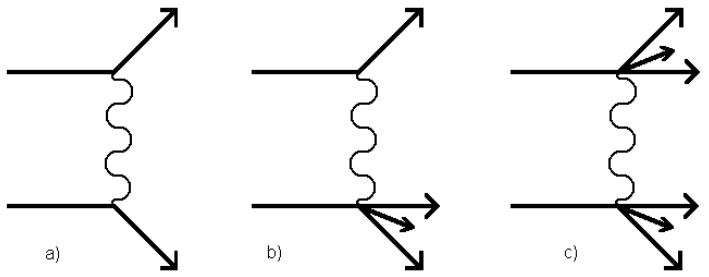

Figure 2.4: a) Nondiffractive scattering, b) single diffractive scattering, c) double diffractive scattering, all by pomeron exchange.

Inelastic processes are characterized by a substantial energy loss that goes into particle production and one or both of the incident protons are destroyed (single-diffractive and non-single-diffractive processes respectively).

Most of the produced particles are pions (80-90%). Kaons, protons, neutrons and other mesons and baryons consisting of light quarks (u,d,s) make up most of the rest, together with their antiparticles. A few hadrons with heavy quarks pairs created in hard scatterings also occur. The multiplicity of charged particles, which most detectors are sensitive only to, is increasing roughly as $ln(\sqrt{s})$. Charged pions are the most commonly detected particles. There are two charged pion and one neutral, which will go undetected in charged particle detectors.. The total multiplicity is well approximated by multiplying the charged multiplicity with $\frac{3}{2}$, assuming equal production of all three pion species .

A typical p+p inelastic scattering at high energies involve a hard scattering between two partons and the rest of the incident particles flying away as fragments. These fragments will often hadronize into a "leading particle" that carry away large amounts of momentum and appear near beam rapidity. Leading particles are absent in e^+e^- annihilations, as these point particles are annihilated as they interact. About 50% of the incident projectile energy is carried away with the leading particle, while the remaining 50% goes into particle production in the midrapidity region. A consequence is that average e^+e^- annihilations have about twice the multiplicity of average p+p collisions at a given $\sqrt{s}$ [8].

2.4 String picture of p+p collisions

Transverse and longitudinal momentum distributions of produced particles are interesting in order to understand the reaction dynamics and projectile structure. Typically measured is the multiplicity as a function of the rapidity or pseudorapidity of the produced particles in a reaction ($\frac{dN}{dy}$, $\frac{dN}{d\eta}$). At previously studied p+p momenta, the rapidity distribution of the particles is Gaussian around zero. The corresponding pseudorapidity

distribution has Gaussian-like tails at high pseudorapidity, but is two-humped. An interesting phenomenon is predicted to occur at higher at higher energies, the Gaussian falloff is preserved at higher/lower pseudorapidities, while at midrapidity, a plateau evolves in which the particle yield is nearly constant over several units of pseudorapidity. This should happen in both heavy ion and p+p collisions to a different extent, and is interpreted as a color field tube being stretched between the strongly interacting projectiles.

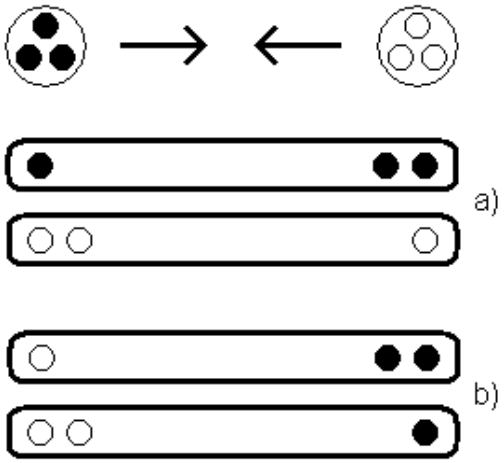

Figure 2.5: Two types strings formed in a p+p collision: a) Longitudinally excited string. b) Color exchange produces a string with partons from both projectiles.

As they move apart from each other, the field energy increases towards field strengths where quark-antiquark pair production is favorable instead of stretching the string further. A force of the form

$$F_{qq}(x) = -k_S \tag{3}$$

where k_S is about 1 GeV/fm, is used as a phenomenological description. It should not be confused with the classical spring force $F(x) = -kx$. Eventually, the string hadronizes into a cloud of mainly pions. Several models for this *string fragmentation* exists, with a $q\bar{q}$ pair being produced at each breaking point.

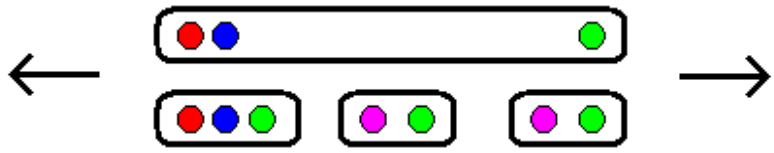

Figure 2.6: A longitudinally excited string, fragmenting into two mesons and a baryon. Colors and anticolors are shown.

It is interesting to study strangeness production in a string model. The following reactions require only one $s\bar{s}$ pair produced.

$$udu(p) \rightarrow uds(\Lambda) + \bar{s}u(K^+)$$

$$uud(p) \rightarrow uus(\Sigma^+) + \bar{s}d(K^0)$$

while

$$udu(p) \rightarrow udu(p) + u\bar{s}\ (K^-) + \bar{s}u(K^+)$$

requires two quark-antiquark pairs produced $s\bar{s}$ and $u\bar{u}$. Thus, an overweight of K^+ relative to K^- and more K^+ close to string ends is expected, and this is indeed seen.

A meson at rest can have only one string configuration: Two valence quarks with a gluonic string in between. In contrast, a baryon at rest consisting of three valence quarks can naively have a quark-quark-quark linear configuration, a quark-diquark configuration, a triangle (Δ-delta) configuration and a Y configuration, which was proposed by Veneziano [9].

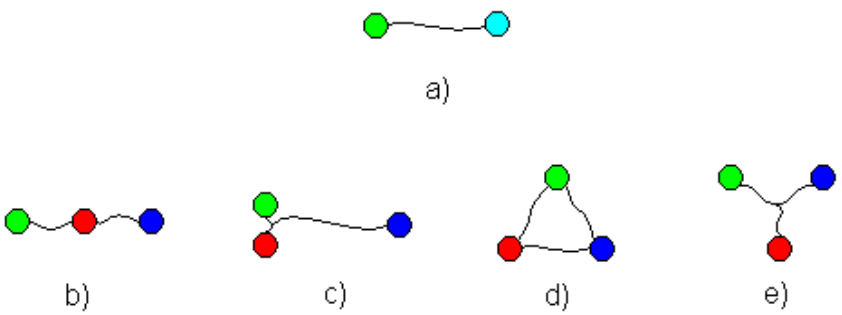

Figure 2.7: a) Meson configuration. Baryons: b) Linear configuration, c) Diquark-quark , d) Δ-configuration, e) Y-configuration

2.5 The midrapidity region and the fragmentation region

As strongly Lorentz contracted collision partners pass each other, a region with small net matter density, but filled with strong color fields is created. Further expansion causes the fields to transform into particle-antiparticle pairs, following the string fragmentation picture. These particles have little longitudinal momentum, and pair production is therefore dominant source of particles at midrapidity.

The baryon number

$$\frac{1}{3}(N_q - N_{\bar{q}}) = N_B - N_{\bar{B}} \tag{4}$$

has never been observed to be violated in any process, and this naive picture implies that the rate of $\frac{\pi^-}{\pi^+}$, $\frac{K^-}{K^+}$ and $\frac{p^-}{p^+}$ at midrapidities should be exactly one, when starting with pure color fields and no net quarks. Experimentally, this holds well for pions. Negative kaons vs positive kaons have a somewhat smaller ratio and antiprotons vs protons a significantly smaller ratio. There should naively also be no "net protons" p-$\bar{\text{p}}$. Experimentally, a significant number of net-protons are seen at midrapidity, implying that there is some mechanism transporting baryon number towards smaller rapidities. It has been suggested that the baryon number actually is associated with gluonic configurations, and not with valence quarks [12]. Gluon configurations can much more easily than quarks be transported over a large rapidity interval, by reactions as depicted in figure 2.8.

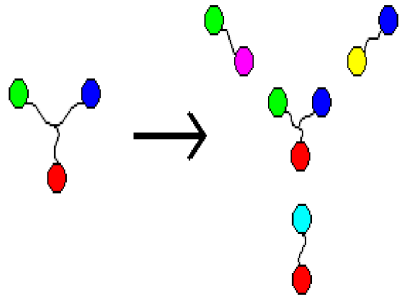

Figure 2.8: A Y-configured baryon fragmenting into three mesons and a new baryon.

A very different picture applies in the regions seen at forward rapidities. This is called the fragmentation region, as fragments of the original projectiles, valence quarks, are abundant. Obviously, this region has an overweight of u over d valence quarks, as the proton (uud) projectiles are isospin asymmetric. A consequence is that the $\frac{\pi^-}{\pi^+}$ ratio drops at more forward rapidities. $\frac{K^-}{K^+}$ and $\frac{\bar{p}}{p}$ also drops towards smaller values than at midrapidity. The fragmentation region behaves approximately similar at different $\sqrt{s}$, a phenomenon known as *limited fragmentation*. This occurs because the valence quarks

govern the dynamics in this region. To see whether limited fragmentation holds, one can plot measured quantities from different y_{beam} as a function of $y - y$ or $\eta - y_{beam}$, clearly seen in figure 2.9.

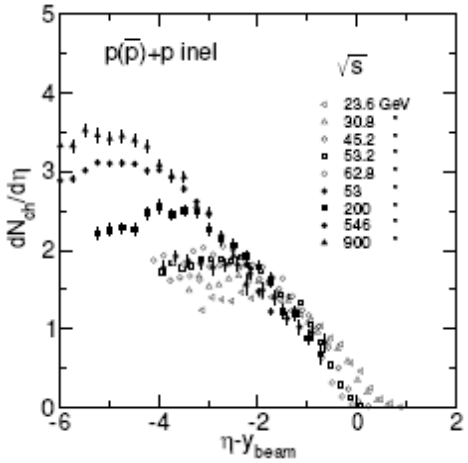

Figure 2.9: $\frac{dN}{d\eta}$ as a function of $\sqrt{s_{NN}}$ for several different beam $\sqrt{s_{NN}}$. The fragmentation region is seen to behave identically at several different $\sqrt{s_{NN}}$.Data from [10],[11].

2.6 Stopping

The *absolute* stopping is measured as the difference between beam rapidity and average net baryon rapidity in the final state.

$$\delta y = y_b - \langle y \rangle \tag{5}$$

where

$$\langle y \rangle = \int_0^{y_b} y \frac{dn}{dy} dy \Big/ \int_0^{y_b} \frac{dn}{dy} dy \tag{6}$$

y_b is the beam rapidity and $\frac{dn}{dy}$ is the number of net-baryons (baryons - antibaryons) per rapidity interval.

A heavy ion collision has a beam energy dependant stopping reaching $\delta y \approx 2$ at RHIC energies, and perhaps already saturating at $\sqrt{s_{NN}} \geq 62\ GeV$, while a proton-proton collision has a stopping of $\delta y \approx 1$, almost $\sqrt{s}$ independent [13].

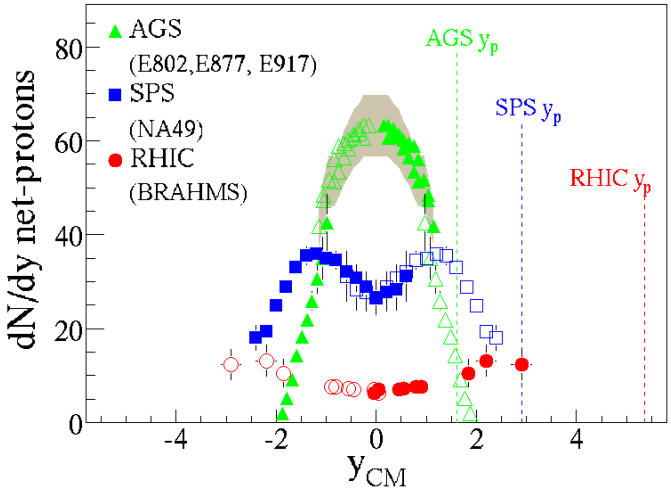

Figure 2.10: Net-baryon $\frac{dN}{dy}$ in heavy ion collisions at different energies (Au+Au at RHIC, AGS, Pb+Pb at SPS). Figure from [14].

3 Heavy ion collisions

A "heavy ion" in nuclear physics is anything heavier than a helium nucleus, consisting of two protons and two neutrons. This thesis will concentrate on the soft physics in proton-proton collisions at two different CM energies. These results are the reference for understanding collective effects when systems of hundreds of protons and neutrons collide at once in a heavy ion collision. Comparisons of p+p and A+A collisions are crucial in understanding the nature of deconfinement, the different phases of quark matter and the role of system size for collective effects/bulk effects in a strongly interacting system. A brief treatment of heavy ion collisions is therefore included.

3.1 Phase diagram of nuclear matter

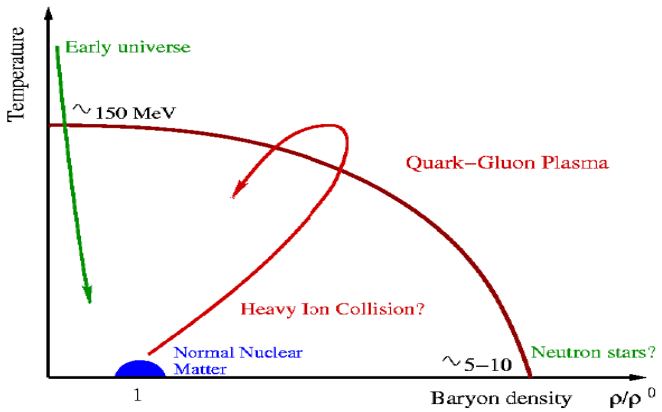

Figure 3.1: The phase diagram of nuclear matter. Figure from [15].

All the matter we see around us is "cold" nuclear matter surrounded by electron clouds. The quarks and gluons are confined within protons and neutrons, and protons and neutrons mostly are bound together into nuclei. Neutrons are unstable outside a nucleus with a half life of 11 minutes. As in other systems, phase transitions in nuclear matter may occur when temperature or pressure/chemical potential or both are increased.

If the temperature is increased for normal nuclear matter, fragments of nuclei will boil off. A typical heavy nucleus has the binding energy of about 8 MeV/nucleon. Heated under this threshold, the nucleus will split into larger fragments, while above, complete fragmentation into nucleons occur. Excited nucleon states in angular momentum or spin, like delta resonances, appear at higher energies. Eventually, thermally produced pions from inelastic hadron collisions will dominate. This phase is known as a *hadron gas* (HG), which has a low net baryon density, and also contains strange mesons like kaons and some strange baryons. At a critical temperature $T_{crit} \sim 170\ MeV$, some sort of phase transition into a deconfined state is believed to occur, easily demonstrated in lattice calculations by an abrupt rise in the energy density $\varepsilon(T)$ [16].Thermally formed $q\bar{q}$ pairs between hadrons will be indistinguishable from quarks inside hadrons and the hadrons cease to exist as bound structures. Effectively, quarks and gluons are now deconfined, and the phase is denoted the *Quark-Gluon plasma* (QGP). It is probably similar to the state of matter in the early universe.

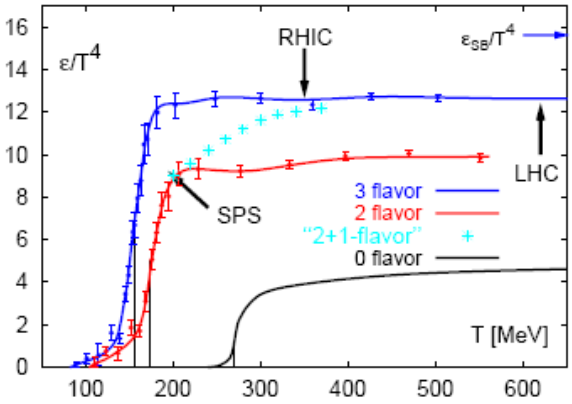

Figure 3.2: Lattice calculations reveal an abrupt phase transition at T_{crit}. Figure from [16].

Following the other route towards deconfinement, the pressure is increased and at some point the wavefunctions of quarks and gluons are overlapping between the individual hadrons. At some point they overlap so much that the partons "forget" which hadron they belong to and a liquid-like state will result. It might be color superconducting and reside within neutron stars, or even denser proposed objects, quark stars. Objects like this will have a density 5-30 times ordinary nuclear matter. To map out the phase diagram can be extremely hard, especially the high-pressure parts, difficult to create on Earth.

3.2 Collision evolution, Bjorken and Landau picture.

First, nuclei and nucleons break apart and hard partons scatterings take place. A deconfined state with freely propagating quarks and gluons is created, possibly reaching thermal and chemical equilibrium. After a short time interval, soft fragmentation of stretched color strings into hadrons take place. Hadron production from a QGP can also take place by quark coalescence or by fragmentation of fast single partons. The partonic matter and later hadron gas expands and cools. Finally, unstable particles decay into the particles seen in detectors.

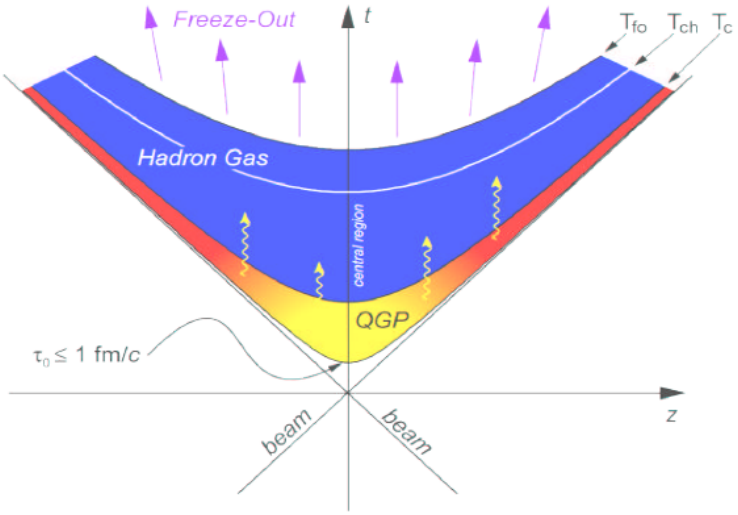

Figure 3.3: Possible space-time evolution in a heavy ion collision. Figure from [17].

If the two participant slabs of nuclear matter projectiles collide, come to rest in the CM system, and then hydrodynamically expand again, the collision follows the Landau picture. The hydrodynamical expansion gives a Gaussian $\frac{dN}{dy}$ distribution around zero rapidity. Such a behavior is known to be consistent with experimental observations at $\sqrt{s_{NN}}$ of some tens of GeV or less. The nature of this matter can be both a HG or a QGP.

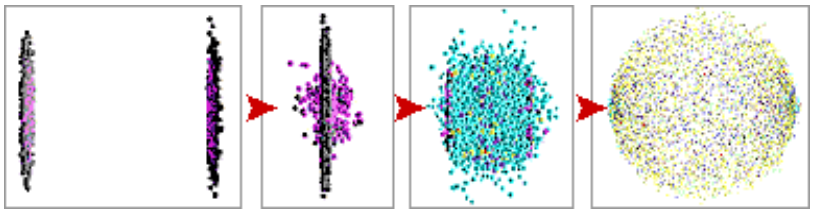

Figure 3.4: A Bjorken-like heavy ion collision. Figure from [24]

A contrasting model is the Bjorken picture [18]: Slabs of nearly transparent nuclear matter pass through each other, creating a highly excited color field in between with few net-baryons, probably similar to the Big Bang QGP. The flux tube field energy will go into creating many light particles, mostly pions, being seen at midrapidity. Baryon rich fragments from the projectiles propel at more forward rapidities, know as the fragmentation region. Also in this case, stopping and baryon transport are interesting problems to study. Transparency is increasing with energy and the Bjorken model predicts a wide plateau in $\frac{dN}{dy}$ around midrapidity at LHC energies.

Bjorken estimated the initial state energy density in a fully central collision:

$$\epsilon = \frac{1}{\pi R^2 \tau} \frac{d\langle E_T \rangle}{dy} = \frac{1}{\pi R^2 \tau} \langle m_T \rangle \frac{dN}{dy} \tag{7}$$

where πR^2 is the area of the nuclei and τ is the plasma formation time. A nucleus with a A nucleons has a radius given by the following relation:

$$R \approx R_0 A^{\frac{1}{3}},\ R_0 = 1.2\ fm \tag{8}$$

The mean transverse mass $\langle m_T \rangle$ and $\frac{dN}{dy}$ of observed particles can easily be measured. Heavy ion collisions have a rather well defined R and τ is expected to be about 1 fm/c. A conservative estimate for a central Au+Au collision at top RHIC energies for this system gives $\epsilon = 5\ GeV/fm^3$. This is 30 times more than the nuclear energy density of 0.16 GeV/fm^3 , ten times typical energy densities within hadrons, and five times more than the energy densities at deconfinement in lattice calculations, $\varepsilon_{crit} = 1\ GeV/fm^3$.

3.3 Indicators of QGP formation

To distinguish the deconfined QGP from a hadron gas, many possible experimental indicators are available. Arguably the most important signatures will be discussed in the following.

3.3.1 Jet quenching and high-p_T suppression

It was early seen that the ashes of hadron collisions did not have a perfect spherical shape. As energy was ramped up, "jets" with high transverse momentum were discovered. These are narrow solid-angle showers of hadrons with a leading fragment. Today, it is known that they are the result of hard scatterings between partons. A medium of deconfined color charges will strongly interact with other color charges. If a QGP is formed, fewer jets and a lower fraction of high-p_T particles should be seen, as high-momentum partons lose much energy in the medium [19]. Analogies like "gluonic" X-ray production (though a few hard collisions) or "Bethe-like" loss of energy (continuous energy loss during the passage through the medium) have been proposed. Indeed, a strong high-p_T suppression is seen at all rapidities in central Au+Au collisions, while not seen in more peripheral collisions or d+Au collisions (where there should not be hot enough nuclear matter to create a QGP). The different behavior of the two systems shows a final state medium effect to be present in the Au+Au collisions. To quantify the suppression of high-p_T particles, the "nuclear modification factor" is defined:

$$R_{AA} = \frac{d^2 N^{AA}/dp_T dy}{\langle N_{bin} \rangle\, d^2 N^{NN}/dp_T dy} \tag{9}$$

where the mean number of binary collisions in the A+A system, $\langle N_{bin} \rangle$, is obtained from the Glauber model. $d^2N/dp_T dy$ is the differential yield (in A+A or N+N collisions) of a particle species at a given transverse momentum and rapidity interval. If an A+A

collision is merely a superposition of elementary N+N collisions, this ratio should be about 1 at higher p_T, where hard processes dominate. At low p_T where soft processes are responsible for particle production, there is scaling with the number of participating nucleons and R_{AA} falls below $\langle N_{bin} \rangle$ scaling. Often unidentified charged hadrons are studied and pseudorapidity is used in the differentials. RHIC experiments have measured both unidentified hadron R_{dAu} and R_{AuAu} at $\sqrt{s_{NN}} = 200\ GeV$, by comparing d+Au and Au+Au spectra with p+p reference spectra.

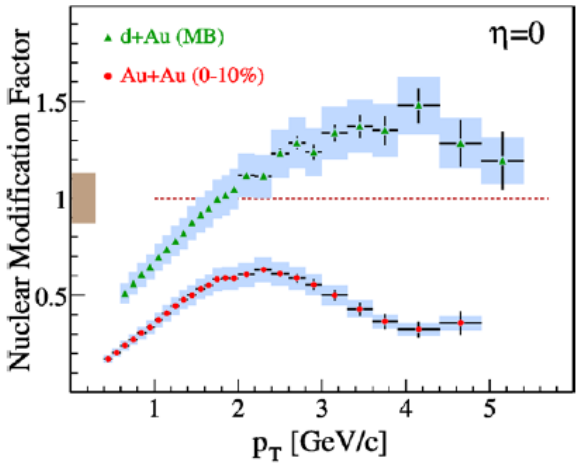

Figure 3.5: Behaviour of the nuclear modification factor in d+Au and Au+Au collisions at $\sqrt{s_{NN}} = 200\ GeV$ [23]

Both the d+Au and the Au+Au exhibit falling R_{AA} for lower p_T as expected. An enhancement caused by multiple scatterings in the initial partonic state is seen in d+Au collisions.. The effect is known as the Cronin enhancement. A very large suppression is seen in central Au+Au collisions at high-p_T at RHIC energies, consistent with, but not proving the idea that a QGP is created in such collisions. The effect is absent in the d+Au control experiment, which has the same initial state for the incoming Au nucleus. This confirms that the suppression seen in Au+Au is a final-state effect.

Jets are usually resulting from a hard QCD scattering, creating a pair of partons propagating nearly 180 degrees back to back in the azimuthal direction. If one jet is formed near the surface of the fireball, it will escape mostly unattenuated, while the other jet will be hampered by the hot soup of freely moving colored partons. Back-to back jet correlations do indeed reveal a strong suppression in central Au+Au and absence of suppression in d+Au collisions.

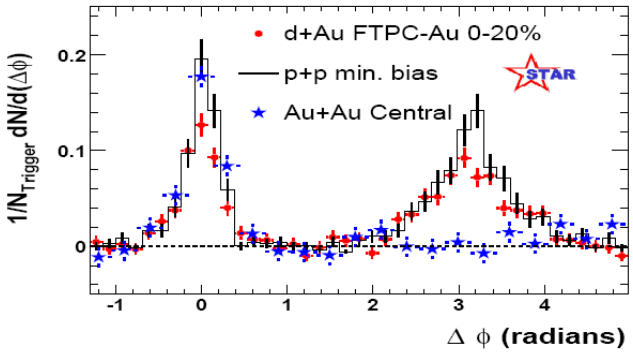

Figure 3.6: Back-to-back jet correlations for p+p, d+Au and Au+Au collisions seen in STAR. Figure from [21],

Also observed in semi-central collisions is a significant suppression of high-p_T particles in the normal direction to the reaction plane, while the suppression in the plane is far less [22]. This is interpreted as a path length effect since the semiaxis of the almond shaped interaction region is larger out of plane than in plane.

3.3.2 Flow

If hydrodynamics is assumed to be valid for the hot, strongly interacting matter, concepts like flow can be invoked to describe the collision evolution. The spatial anisotropy is often parametrized as a series expansion in $cos\left[n(\phi - \phi_r)\right]$.

$$E\frac{d^3N}{d^3p} = \frac{1}{2\pi}\frac{d^2N}{p_T dp_T dy}\left[1 + \sum_{n=1}^{\infty} 2v_n\left[n(\phi - \phi_r)\right]\right] \tag{10}$$

ϕ_r is the angle of the reaction plane and ϕ is the angle of the emitted particle. Each n term have a v_n parameter. Ordinary thermal radial flow is absorbed in the constant term. It has a flow velocity of 0.70-0.75 c. Such a large flow velocity must result from an extremely dense source. v_1 is a collective directed motion of produced particles and nuclear fragments, strongest at high $|y|$, close to the fragmentation region. When two nuclei collide with a nonzero impact parameter (b), the result will be that the spectactor nucleons continue on their path, while an almond shaped fireball of participant nucleons form. The pressure will be greatest along the shorter axis and the expansion will be anisotropic. A large v_2 parameter, the elliptic flow, results. It has been measured for several particle species and indicates strong collective motion. Recent results (2004) from RHIC indicate that the deconfined state is near a perfect liquid and less like a conventional gas/plasma [25]. Scaling properties of the elliptic flow, as function of number of valence quarks, indicate that the flow develops during the partonic stage [26].

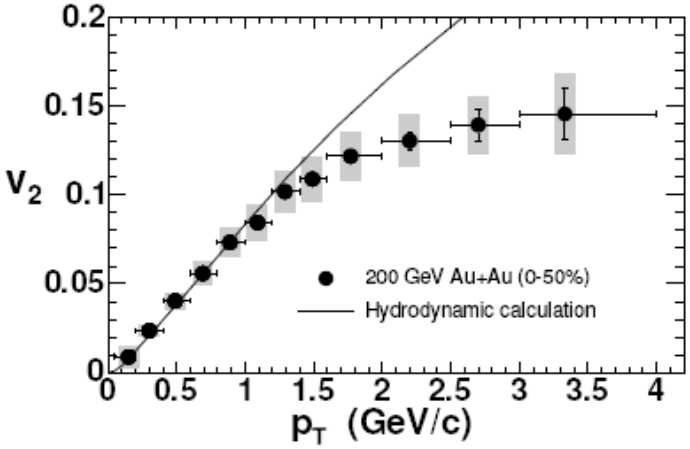

v_2 as a function of p_T at midrapidity for 50% most central $\sqrt{s} = 200$ GeV Au+Au collisions. Figure from [27].

3.3.3 J/Ψ suppression

Heavy quark-antiquark pairs are expected to form in the early stages in the collision, mostly from the reaction $gg \rightarrow q\bar{q}$. The most abundant quarkonium species at SPS and RHIC is the J/Ψ particle, charmonium, a $c\bar{c}$ state. At the LHC, the corresponding heavier Υ meson, bottonium, a $b\bar{b}$ state, is expected to be important as well. These particles often decay electromagnetically into a e^+e^- or $\mu^+\mu^-$ pair with a characteristic invariant mass, very easy to see in a detector with large solid angle acceptance. A deconfined medium with free color charges will screen the quarks from each other, preventing charmonium or bottonium to form. Less decays will then be seen, and this effect was first discovered at the SPS [28]. The STAR and PHENIX experiments have measured J/Ψ suppression at RHIC, and the suppression is seen to increase in larger systems, in which a QGP are more likely to be formed. The level of suppression is about the same as at SPS, despite a denser medium. A possible explanation can be J/Ψ regeneration, by $c\bar{c}$ coalescence.

3.3.4 Strangeness enrichment

In a QGP, three mechanisms can produce $s\bar{s}$ pairs in lowest order QCD [20]. These are: a) quark-antiquark annihilation, b) gluon fusion and c) thermal gluon decay. If the QGP has a significant content of net light quarks from the original baryons, the $u\bar{u}$ and $d\bar{d}$ pair production will be suppressed by u and d quarks already present, in phase space by a factor $e^{-\frac{\mu_B}{3T}}$.Formation of $s\bar{s}$ quark pairs is reduced by a factor $e^{-\frac{m_s}{T}}$, as the strange quark has a larger mass than up and down quarks. These suppression factors are of the

same magnitude, but it is possible that QGP produced in a heavy-ion collision has such a short lifetime that chemical equilibrium is not reached. If, though, the equilibration is sufficient, $\bar{u}$, $\bar{d}$ and $\bar{s}$ will have similar abundances. This should facilitate easy production of multi-strange antibaryons, but this also requires a fast freeze-out (coalescence).

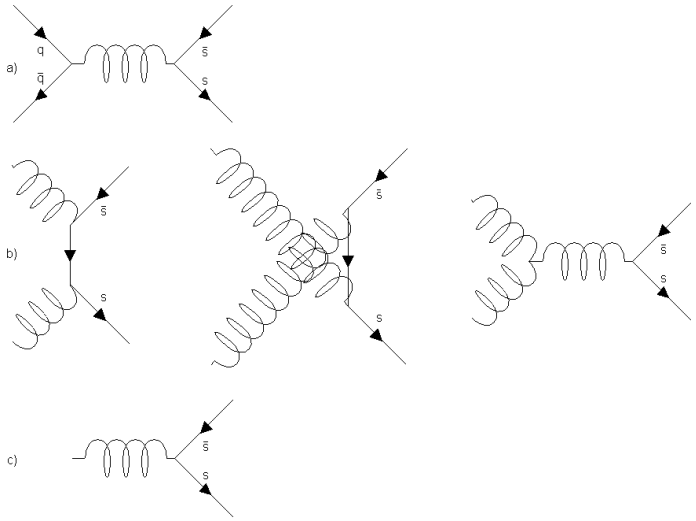

Figure 3.8: Strangeness producing reactions in a QGP: a) Quark-antiquark annihilation, b) gluon fusion, c) thermal gluon decay. Figure from [20].

Contrasting, in a HG, the strange particle yields are determined by: a) strangeness producing reactions, b) strangeness redistribution reactions and c) annihilation reactions [20]. Strangeness producing reactions such as $\pi\pi \rightarrow K\bar{K}$, $\pi N \rightarrow K\bar{K}$, , , , , are slow, as they involve the annihilation of a quark-antiquark pair into a gluon, which then decays into a $s\bar{s}$ pair (thus violating the OZI rule) and have high energy thresholds.. Strangeness redistribution is much faster, as these reactions correspond diagrams with continuous quark lines and are highly exotermic. The quick redistribution gives a fast strangeness relative equilibration time in a HG. Both considerations hamper the production of multistrange antibaryons, as multiple unlikely reactions must occur to form them and their strange quarks are quickly redistributed to other hadrons. An increased yield of multistrange antibaryons is therefore an indicator of a QGP being formed.

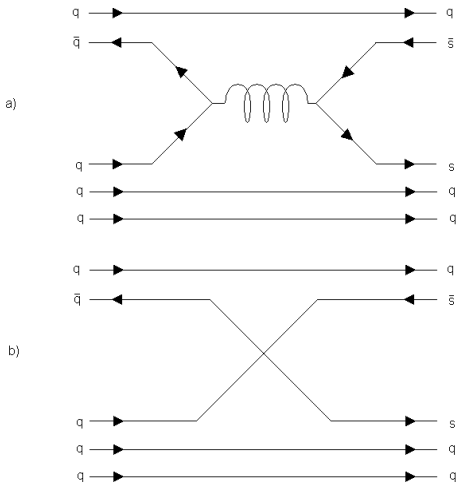

Figure 3.9: Reactions involving strange quarks in a hadron gas: a) Meson-Baryon reaction producing a strange quark pair. b) Meson-Baryon strangeness redistribution reaction. Incoming baryons can contain more than one s-quark. Figure from [20].

4 Experimental setup

Accelerators and detectors are the physicists' microscope into the subatomic world. In order to effectively and correctly utilize these powerful tools and know their strengths and limitations, a good understanding of the experimental setup is required. This chapter provides a discussion of the BRAHMS experiment at RHIC, with special emphasis on the detectors used in analysis in this thesis.

4.1 The RHIC accelerator

The RHIC accelerator [29] is situated at Brookhaven National Laboratory, Long Island. It is a set of two hexagonal storage rings with a circumference of 3824 meter, the blue and the yellow ring. 1740 superconducting magnets are holding the beams into place. There are six intersections points where beams can collide. Such a setup provides nearly total freedom in projectiles used.

Protons start in the 200 MeV linear accelerator (Linac), while heavy ions are stripped for some of their electrons in the Tandem Van de Graaf. They leave it with about 1 MeV nucleon (MeV/A) and a charge of +32. Through the tandem to booster transfer line, they arrive in the booster synchrotron and are further accelerated to 95 MeV/A and

further stripped for electrons. In the Alternating Gradient Synchrotron (AGS), ions are totally stripped for electrons and accelerated to 10.8 GeV/A. Injection into RHIC takes place through the AGS to RHIC transfer line (ATR). A switching magnet sends different bunches into each storage ring, and two beams rotating against each other are created. Further acceleration until desired beam energy is then done. The maximal possible energy for proton beams is 250 GeV, while beams of gold nuclei can be accelerated to 100 GeV/A, translating into maximal $\sqrt{s_{NN}}$ = 500 GeV and$\sqrt{s_{NN}}$ = 200 GeV/A, respectively.

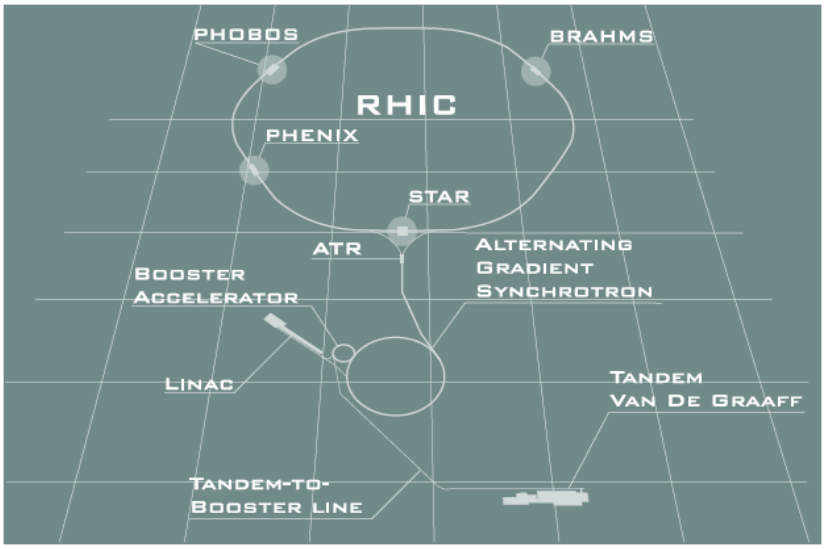

Figure 4.1: Schematic overview of the RHIC complex. Figure from [17].

RHIC has 4 larger experiments: STAR, PHENIX, PHOBOS and BRAHMS. PHOBOS and probably BRAHMS have stopped taking data, while the other two are being upgraded. While the Large Hadron Collider at CERN, Geneva will exceed RHIC in CM energy, RHIC will still be the most powerful particle accelerator in operation capable of colliding spin-polarized protons. A luminosity upgrade (RHIC-II) and a nuclei-electron collider upgrade (eRHIC) are being planned.

Several different projectiles have been collided and studied at RHIC. BRAHMS took data at the following runs:

Run	Species	$\sqrt{s_{NN}}$ (GeV)
1	Au+Au	130
2	Au+Au, p+p	200
3	d+Au, p+p	200
4	Au+Au, p+p	200, 62.4 (only Au+Au)
5	Cu+Cu, p+p	200, 62.4 (only Cu+Cu)
6	p+p	62.4

Table 4.1: Runs where BRAHMS took data.

Au+Au collisions provide the primary system in which a deconfined partonic state is expected to be seen in the hot nuclear medium. p+p collisions are used as a nucleon-nucleon reference to study the collective dynamics of the heavier systems colliding. p+p collisions are also interesting on their own, as it is the simplest strongly interacting projectile, it can be used to study other aspects of the strong interaction. d+Au is a heavy-light system that is "colder" than Au+Au. It consists mostly of Au spectator matter and is not supposed to leave the hadron-gas phase. It can be used to decide whether the effects seen in Au+Au are final state medium effects or resulting from the initial state, for instance gluon shadowing or saturation. Cu+Cu is a system of intermediate size, but large enough to allow QGP formation, studied to map out the system size dependence of various phenomena.

4.2 The BRAHMS experiment

BRAHMS is an acronym for Broad RAnge Hadron Magnetic Spectrometer and is designed to do momentum precision measurements of identified charged hadrons over a wide range of rapidities [30]. Electrons and muons will also give a signal in most detectors. BRAHMS is situated in the 2 o'clock position of the ring.

Name	Quark content	Symbol	Charge	Mass (MeV)
Electron/positron	–	e^-, e^+	$-1, 1$	0.511
Muon/antimuon	–	μ^-, μ^+	$-1, 1$	105.66
Positive Pion	$u\bar{d}$	π^+	1	139.57
Negative Pion	$\bar{u}d$	π^-	-1	139.57
Positive Kaon	$s\bar{d}$	K^+	1	493.667
Negative Kaon	$\bar{s}d$	K^-	-1	493.667
Proton	uud	p	1	938.272
Antiproton	$\bar{u}\bar{u}\bar{d}$	$\bar{p}$	-1	938.272

Table 4.2: Particles detected by BRAHMS. In addition, ZDCs can see neutrons. Shorter lived particles are not seen.

BRAHMS consists of two movable spectrometers, the Forward Spectrometer (FS) and the Mid-Rapidity Spectrometer (MRS), able to take data simultaneously. The FS

is then again divided into the Front Forward Spectrometer (FFS) and the Back Forward spectrometer (BFS). In addition, global detectors are present to characterize the events, determine the interaction vertex position and provide a start for the Time of Flight (TOF) systems.

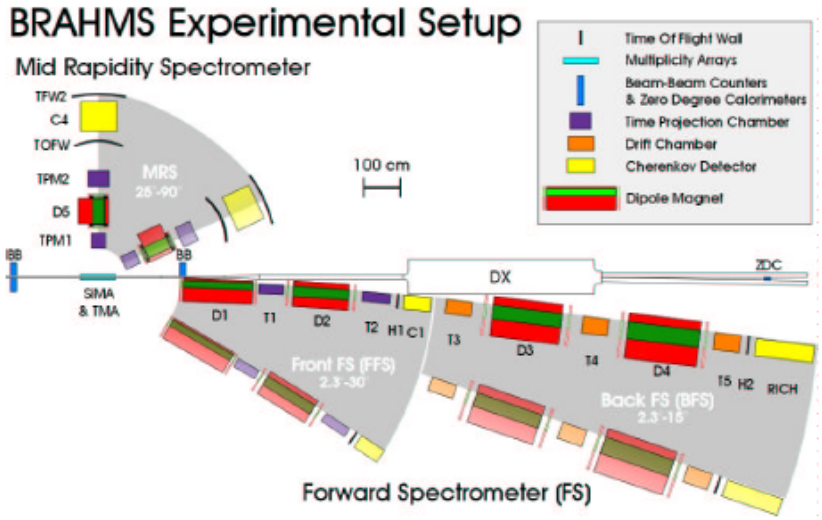

Figure 4.2: The BRAHMS experimental setup. Figure from [17].

The solid-angle coverage is small, but the spectrometers are movable and can therefore identify particles over a large range of rapidities ($y = -0.2$ to $y = 4$, corresponding to momenta of some hundred MeV to 25-30 GeV/c). Other experiments at RHIC cannot do charged particle identification (PID) above $|y| \approx 2$. Thus, BRAHMS can study physics at forward rapidities, the small-x region of target structure functions (large-x valence quarks in one projectile will probe small-x gluons in the collision partner). BRAHMS can also see the fragmentation region that has a high net baryon density from the valence quarks present in the colliding beam nucleons, thus enabling BRAHMS to study net baryon transport from higher to lower rapidities.

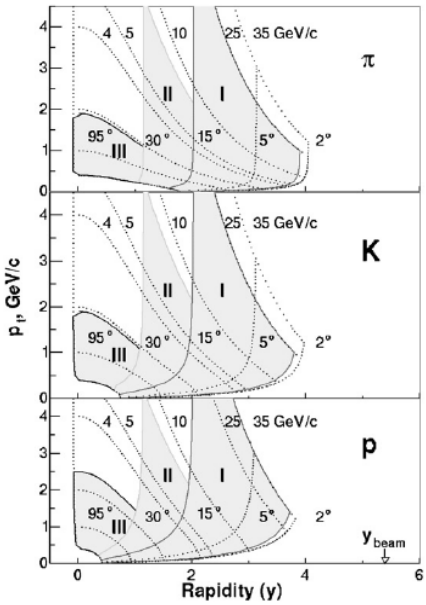

Figure 4.3: BRAHMS acceptance
for different particle species.
Figure from [30].

4.2.1 Global detectors

Global detectors are used for characterizing events with multiplicity/centrality and providing event vertex. Some triggers also get their signal from here.

4.2.2 Multiplicity array

Two detectors formed as hexagonal barrels make up the multiplicity array. The inner one is silicon strip detectors, the outer one is made of plastic scintillator tiles. Event multiplicity is not directly measured. Instead, deposited energy from charged particles is measured. Within an error of 5-10%, the multiplicity can be calculated from the deposited energy. In heavy-ion collisions, this is taken as a measure for the centrality of the collision. Segmentation allows measuring the multiplicity distribution as a function of the pseudorapidity. Angular coverage is between $12.6° < \theta < 167.4°$ implying that particles with $\eta < |2.2|$ around the nominal vertex position are detected. The multiplicity/centrality has not been given further attention in p+p collisions measured in BRAHMS.

4.2.3 Zero-Degree calorimeters

All RHIC experiments share common Zero Degree Calorimeters (ZDCs). Situated at ± 18 meters away from the nominal interaction vertex, they measure spectactor neutrons at high longitudinal momenta. ZDCs provide information about centrality, vertex and most importantly, they can provide common event characterization in all RHIC experiments, as they have identical designs in all four setups.

4.2.4 Beam-Beam counters

The Beam-Beam counters are used to determine event vertex, provide minimum bias trigger and a start for the time of flight systems for A+A collisions. They consist of two arrays, sitting at ± 220 cm from the nominal interaction vertex, at $|\eta| = 3.1$, 3.4 and 3.6. Consisting of both small and large Cherenkov elements, they are read out by photomultiplier tubes. The vertex position resolution is more precise than 1.5 cm. The Beam-Beam counters are not used in d+Au or p+p, as the final state multiplicity is too low. Instead, CC detectors are used.

4.2.5 CC detectors

The CC detectors are Cherenkov light detectors, placed around the interaction region at ± 1.9 and ± 6.4 meters, thus covering the pseudorapidity region $3.25 < |\eta| < 5.25$. Used in p+p run 5 and 6, they superseded the INEL inelastic collision vertex detectors and minimum bias trigger. Coincidental hits in CC detectors on both sides are required. This means that the event sample collected by BRAHMS will be NSD events (double-diffractive and more central events). Event vertex is also provided with a resolution of 1.6 cm.

4.2.6 Trigger slats and triggers

Many detectors continuously give signals or noise, and to record all this data would be impossible and uninteresting. Triggers provide a way to do this: A "trigger" is a combination of signals resulting from a charged particle being detected in one or more detectors in order to select only interesting *events* (signals clearly coming from an interesting physical process). A minimum bias trigger is needed to normalize the detected particle yields to statistical yield-by-event. For p+p at $\sqrt{s} = 62.4$ GeV, the CC counters are measured to see $33 \pm 3\%$ inelastic cross section of 36 mb. The corresponding number for p+p at $\sqrt{s} = 200$ GeV is simulated to be $70 \pm 5\%$ of the inelastic cross section at 41 mb. At least one hit in both left and right CC is required for an event to have a valid minimum bias trigger. A selected trigger signal (here CC, but need in general not be identical to the minimum bias trigger) also provides a start time for all TOF systems. Scintillator slats sits in front of the FS (TrFs) and the MRS (TrMrs) to select events with good tracks in the corresponding spectrometers.

Trigger	Coincidence required	Number
Minimum Bias	CC-RC	5
MRS track	TrMrs-TOFW-RC	3
FS track	TrFs-H1-H2-RC	2
FFS track	TrFs-H1-RC	6

Table 4.3: Trigger definitions in p+p Run 5 & 6

RC is the RHIC clock. (NB: Minimum bias trigger is numbered 4 for runs 14000 - 14130 in run 5 p+p $\sqrt{s} = 200$ GeV)

4.3 Spectrometer detectors

Several types of detectors are present in the spectrometer arms. A discussion of their purpose and design follows.

4.3.1 Tracking detectors

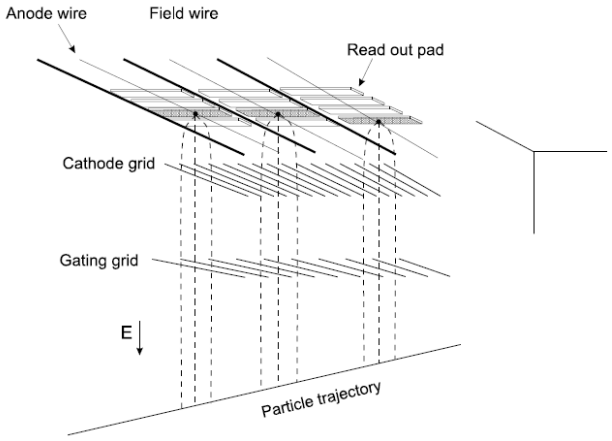

Figure 4.4: Schematic view of particle tracking in a TPC. Figure from [17].

TPM1, TPM2, T1 and T2 are gas-filled time projection chambers (TPCs). Charged particles transversing them will ionize the gas into electron-ion pairs that are separated by an electrostatic field. The electrons drift in the y-direction following the $\vec{E}$ field to a (x,z) plane of anode wires and readout pads. Charges are induced on the readout pads giving information on the (x,z) position. The drift time on the y direction is measured to give y coordinate of track, as the drift velocity is known. Three-dimensional tracks can then be reconstructed. A mixture of 90% Ar and 10% CO_2 is used. This mixture has a slow drift velocity and therefore a high precision is obtained for position determination in the y-direction.

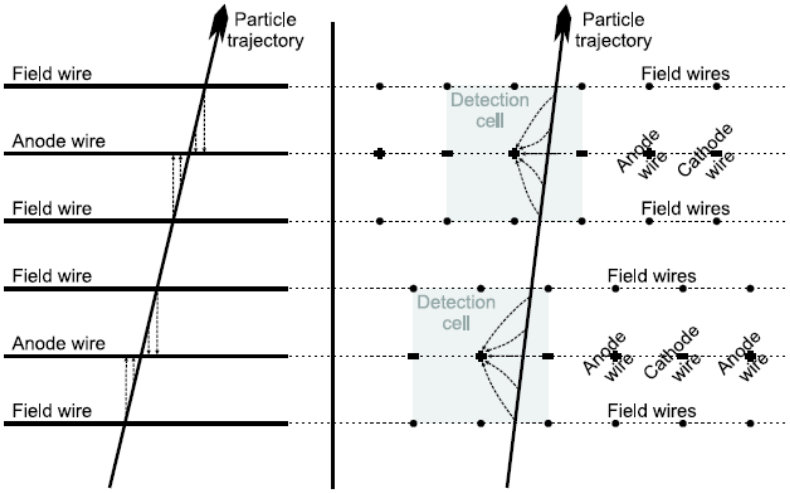

Figure 4.5: Particle tracking in a drift chamber. Figure from [17].

The rest, T3, T4, T5 are multiwire drift chambers (DCs). These DCs are divided into three modules, each consisting of 10 wire planes (T3) or 8 planes (T4,T5). Electrons freed by charged particles ionizing the gas fill are drawn towards anode wires and give a signal. Each wire plane gives only 2D-info: (x,z) from vertical wires and (y,z) from horizontal wires. Spurious combinatorial matchings from (x,y) views are removed by having 2 sets of additional planes with slightly rotated views (u, v directions). Left-right ambiguities are resolved by having slightly staggered anode wires for same view in consecutive planes.

4.3.2 Time of flight systems

A time of flight detector exploits the fact that particles of different mass with equal momenta will have different speeds. Their resolution increase with flight distances. A stopwatch analogy can be used. Start time is a valid CC (BB, ZDC, INEL in other systems) signal. The signal from a particle transversing a TOF slat is the stop time. Two time of flight detectors, H1 and H2 are used for PID at intermediate rapidities in the FS. They consist of plastic scintillator slats (40 and 32 respectively). The scintillator slats are in two staggered rows to minimize the number of particles hitting two or no slats. One photomultiplier tube (PMT) is situated at each end of the scintillator. A "hit" must have a signal in both PMTs. H1 is situated 8.6 m and H2 is situated 19.6 m away from the vertex. H1 will nominally separate π/K up to 3.3 GeV/c and K/p up to 5.7 GeV/c. H2 nominally separates π/K up to 5.8 GeV/c and K/p up to 8.5 GeV/c.

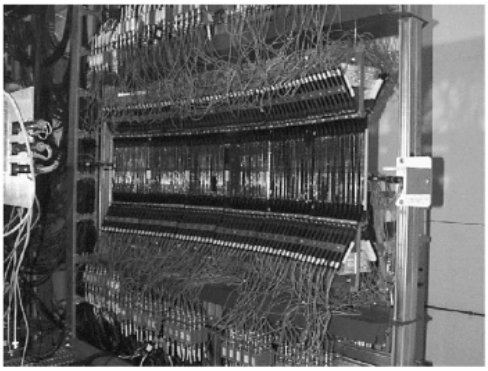

Figure 4.6: Photo of TOFW from [30]

Due to the relatively low momenta seen in the MRS, only time of flight detectors are used. TOFW has been augmented and is now 125 slats wide, sitting 4.3 meter from vertex. TOFW can nominally separate π/K up to 2 GeV/c and K/p up to 3.5 GeV/c.[1] A second time of flight wall (TFW2) has been installed in the MRS. It is further from the interaction point and has therefore better momentum resolution, but its geometrical size is smaller, so acceptance and statistics will go down. TFW2 is not used in this analysis as this trade-off is unfavorable for the datasets analyzed, since the focus is on the low-p_T part of the spectra.

4.3.3 Cherenkov detectors

Just as a sonic boom is heard when an airplane overtakes the speed of sound, a "sonic light boom" is created if a charged particle overtakes the speed of light within a material (the radiator). Light is emitted from the electromagnetic disturbance wavefronts, and this is called the Cherenkov effect. A light cone with opening-angle θ will be created, with θ being a function of the velocity and the refractive index n of the radiator

$$cos\theta = \frac{1}{\beta n} \tag{11}$$

At BRAHMS, the Cherenkov radiators are fluorinated hydrocarbons. Having a n close to 1, particles in the GeV/c region can be separated.

A threshold Cherenkov detector detects the emission of Cherenkov light. It is used as a veto counter (Latin: Veto = I deny), to discriminate between particles which have equal momenta but different velocities due to different masses, so that the one species creates a light cone, while the other fails to do so. One such detector, C1, sits in the end of the FFS and can be used as a veto counter to extend $\pi/K/p$ separation in H1,

[1] Note that the actual achieved separation for most detectors will depend upon particle ratios and statistics, and also somewhat calibration.

by vetoing pions. Filled with C_4F_{10}, it has a pion threshold of 2.6 GeV/c and a kaon threshold at 9.3 GeV/c ($n \approx 1.0014$). C1 is not used in this analysis.

Figure 4.7: The RICH. Photo from [30].

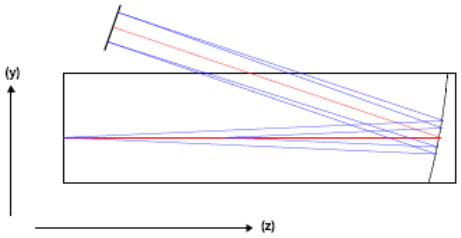

Figure 4.8: Light focussing in RICH. Figure from [31].

The Ring-Imaging Cherenkov (RICH) [32] detector is a more sophisticated device. It measures the radius of rings of reflected Cherenkov light, which is a function of the cone opening angle and thus of the velocity. From that, direct particle identification can be done over a substantial range of high momenta. Light cones impact onto a spherical mirror with 3 meter curvature radius. They are further focussed onto an array of 80 photomultipliers, sitting in four rows of 20 tubes. Each tube is divided in 4 pixels for a total of 320 pixels. They are sitting at a focal length of 150 cm away from the mirror, which is rotated with 8 degrees off the axis. Filled with a radiator composed by C_4F_{10} and C_5F_{12} at 1.25 atm, RICH can separate π/K up to about 20 GeV/c and K/p to at least 30 GeV/c. RICH can also be used as a veto counter to extend $\pi/K/p$ separation in H2, and in fact this is done at the 4 and 6 degree low-field settings. The RICH performs in general very well, but due to pressure variations, the refractive index ($n \approx 1.0018$) of the radiator can change during a run. Data must therefore be inspected and the actual refractive index be used in PID.

4.4 MRS and FS Spectrometer design

Including just one magnet D5 between two time-projection tracking chambers (TPM1, TPM2) for momentum determination and two time of flight detectors (TOFW, TFW2) the MRS is a rather simple setup designed to measure lower-momentum particles from the midrapidity region. It covers the angles between 95 degrees and 30 degrees relative to the beam axis. Geometrical acceptance for the MRS is 6.5 msr. D5 has an aperture 10×35 cm^2 1.9 meters away from the vertex. Particle tracking and momentum is obtained from the magnet and the tracking chambers, while PID is done with TOFW or

TFW2. A threshold Cherenkov detector (C4) is sitting in the MRS, behind the TOF walls. It is not used in this analysis.

FS is a more complex detector than the MRS, in order to provide precision measurements at forward rapidities. The angular coverage of the FS is 30 to 2.3 degrees relative to the beam and its solid angle acceptance is 0.8 msr. The forward spectrometer is separated into two subsystems, the FFS consisting of D1, T1, D2, T2, H1 and C1 and the BFS consisting of T3, D3, T4, D4, T5, H2 and RICH. FFS covers 2.3 to 30 degrees, while BFS covers 2.3 to 15 degrees. D1 is the first magnet in the FS. It is designed to bend particles out of the beam, and with a maximum field of 1.3 T, particles up to at least 25 GeV/c will be extracted into the FS, actually, even higher momenta are seen. The magnet current in D1 is used in the label of FS data settings. Currents up to 3450 amperes are used. The magnetic field in D1 affects the momentum interval of the particles seen, and consequently the PID method that must be used. FS can operate in two modes: high and intermediate momentum mode, using the entire FS or only the FFS respectively. In the high momentum mode, D1 and D2 bend particles out of the beam and into T2 which together with the drift chambers track the particle. This corresponds to very forward angles where track densities may be so high that T1 is not useful for tracking. Momenta are determined from D3 and D4 combined with tracking information to give maximum precision. Intermediate momentum mode utilizes D1 to bend out particles, T1 and T2 together with D2 to provide tracks and momentum.

5 Analysis of the p+p $\sqrt{s} = 62.4$ GeV and $\sqrt{s} = 200$ GeV datasets

Experimental data analysis in high-energy physics is a demanding task and the chain from measured data to physics results is long. This chapter documents the analysis from data selection to final, corrected spectra. In more detail, this chapter will discuss event selection, track reconstruction, run selection, PID, cuts, corrections and spectra generation. The procedure from DST level to final $y - p_T$ spectra for identified particles is specified. A software package named BANAPP has been used in this thesis.

5.1 Data used

To study soft physics in both datasets, these settings were selected in the analysis of p+p $\sqrt{s} = 200$ GeV:

Settings used for p+p $\sqrt{s} = 200$ GeV Run 5	
Angle	Magnet current (Amperes)
2.3	$861(A/B), 1723(A/B), 3450(A/B)$
4	$861\ (A), 1219(A/B), 1723(A/B), 2442(A/B), 3450(A/B)$
45	$1050(A/B), 700(B)$
90	$350(A), 700(A), 1050(A/B)$

Table 5.1: Settings analyzed for p+p Run 6

The following settings were selected in the p+p $\sqrt{s} = 62.4$ GeV analysis:

Settings used for p+p $\sqrt{s} = 62.4$ GeV Run 6	
Angle	Magnet current (Amperes)
2.3	$1723(A/B)$
3	$1723(A/B)$
4	$608(A/B)$
6	$861(A/B)$
45	$700(B), 1050(B)$
90	$350(A), 700(A/B), 1050(A)$

Table 5.2: Settings analyzed for p+p Run 5

Settings with A polarity will extract almost exclusively negative particles into the FS, while B settings select positive particles. In the MRS, A and B settings contain both positive and negative particles at once. The p+p $\sqrt{s} = 200$ GeV run 5 is a high statistics run, while the p+p $\sqrt{s} = 62.4$ GeV run 6 has lower statistics.

5.2 Global event characterization and selection

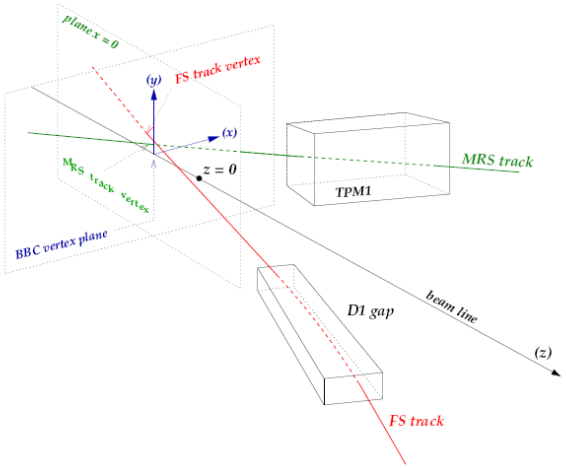

Figure 5.1: BRAHMS global coordinate system and FS and MRS track back-projection coordinates. A right-handed coordinate system with x-axis orthogonal to the beam line in direction of MRS, vertical y-axis and z-axis following the beam line pointing in direction of the FS is used. Figure from [31].

As mentioned, the CC counters are used to determine the interaction vertex. They are hit by particles travelling essentially at the speed of light. The z-coordinate of the vertex can therefore be deduced from

$$z = \frac{c}{2}(t_L - t_R) \tag{12}$$

where the t_L and t_R are the times of hit in the left and right detector, respectively. The nominal interaction vertex is at $z = 0$. No cuts on multiplicity/"centrality" is done. In this analysis, events with vertices inside $z = \pm 30$ cm are used. The vertex bins are 5 cm wide. Yields are normalized according to the number of CC vertices, the minimum bias trigger, as described better in section 4.8. Global tracks have to satisfy FS/MRS track trigger (requirements for all triggers are tabulated in table 4.3). The FS track trigger should not be confused with the less restrictive FFS track trigger, which is not used in this analysis.

Both BRAHMS spectrometers cover a very small solid angle and most events having a CC vertex will not leave tracks in them. If all these events should be stored, immense amounts of uninteresting data would be recorded. Therefore, *scaledown* factors are used. The minimum bias trigger, only requiring a hit in the left and right CC has a large scaledown S_{MB} of several hundred to a few thousand, varying from run to run. FS and MRS track triggers in p+p have a small S_{Tr} scaledown factor, always 1 in these

datasets, meaning that all events satisfying them are stored. Mathematically expressed, the multiplicative normalization factor in a run R for spectrometer tracks originating from a specific CC vertex bin v in a setting s is given by

$$S_{norm\ v,s} = \frac{1}{\sum_R S^R_{MB^s} N^R_{CC\ v,s}} \tag{13}$$

where $N_{CC\ v,s}$ is the total recorded number of events with CC vertex in the setting and vertex bin of interest. As the scaledown factors are not constant, a sum over runs are taken.

5.3 Track reconstruction

A magnet with field vector in the y-direction will bend the trajectories of incoming charged particles in the (x, z) plane. The motion is helical if particle has a momentum component in the y-direction and conserves absolute momentum.

$$\vec{F}_{mag} = q\vec{v} \times \vec{B} \tag{14}$$

Tracking detectors placed on each side of the magnet will measure linear track segments that can be connected by an helical arc. From the change in direction of the track given as entrance and exit angle relative to the magnet axis (Ψ_b, Ψ_f in figure 5.1), the momentum can be determined using the following relation:

$$p = \frac{qB\Delta L}{sin\Psi_b - sin\Psi_f} \frac{1}{\sqrt{1-\alpha_y^2}} \tag{15}$$

where α_y is the track slope in the y direction.

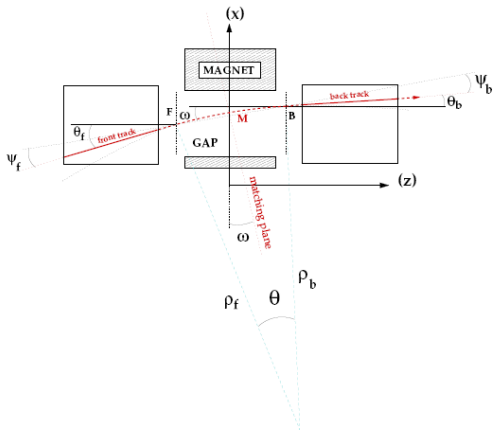

Figure 5.2: Charged particle trajectory, top view. Figure from [31].

Spectrometer	First tracking detector	Magnet	Second tracking detector
MRS	TPM1	D5	TPM2
FFS	T1	D2	T2
BFS	T2 or T3	D3	T4
BFS	T4	D4	T5

Table 5.3: Tracking stations

Local tracking is simply the tracking inside a single tracking detector, which gives a linear track segment which can be either front or back track relative to a magnet. The matching of front track and back track through a magnet has to fulfill the following criteria, defined by 3 matching parameters, shown in table 5.3.

Parameter	Explanation	Physical reason
$\Delta\Psi = 0$	Constant track curvature	$\vec{F}_{mag}$ conserves momentum
$\Delta a_y = 0$	Constant slope in the y-direction	$\vec{F}_{mag}$ has no y-component
$\Delta y = 0$	No track shift in the y direction	Continuous track

Table 5.4: Track matching parameters

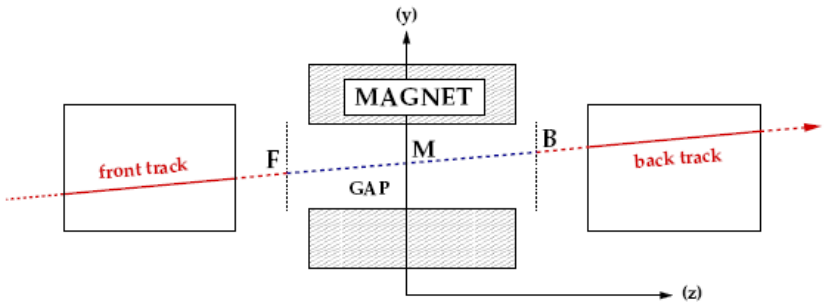

Figure 5.3: Side view of a tracking station. Figure from [31].

Of course, there are statistical errors in the measurements, and the matching parameters have near-Gaussian distributions around centroids with small offsets from zero. Elliptic cuts are done on the matching parameters:

$$\left(\frac{\Delta\Psi - \Delta\Psi_{off}}{\sigma_\Psi}\right)^2 + \left(\frac{\Delta a_y - \Delta a_{yoff}}{\sigma_{a_y}}\right)^2 + \left(\frac{\Delta y - \Delta y_{off}}{\sigma_{\Delta y}}\right)^2 < n_\sigma^2 \qquad (16)$$

where n_σ is the number of standard deviation (unknown numerical value).

In the MRS, there is only one tracking detector combination, while in the FS, three different combinations will provide three different measurements of momentum. For

global tracking, the back track from the matching of local tracks through one magnet, has to be identical to the front track in the matching through the next magnet. Track refits are finally done using all available information to give the best possible FS trajectory and momentum and the χ^2 is calculated for the fitted track relative to associated hits in tracking detectors.

5.4 Track selection and cuts

Only primary tracks coming directly from the interaction region are wanted in the final $y - p_T$ map. Secondary tracks or tracks having undergone dramatic interactions are removed with several constraints, commonly denoted *cuts. Fiducial cuts* are necessary to ensure an accurate geometrical acceptance correction. They also remove tracks too close to magnet or detector walls, as these areas might have undergone scatterings with the detector walls, or have been subject to inhomogenities in electric/magnetic fields. *Pointing cuts* remove tracks not pointing back close enough to the interaction vertex. *Track cuts* are conditions on the quality of the track fit. A cut will always generate some sort of correction for the good primary tracks falling outside the cut and thus being removed.

5.4.1 Vertex and trigger

A CC vertex is always required for a track in this analysis. The CC vertex should be within ±30 cm from the nominal interaction point. FS or MRS track triggers must also be satisfied for tracks in the respective spectrometers.

5.4.2 Magnet cuts

1 cm fiducial cuts are done on the D5 walls. Also, the "*SwimStatus*" of a track through D5 in the MRS or D1 in the FS must be 1. The "SwimStatus" is an extrapolation of a known particle trajectory, checking whether it will pass freely (=1) or be obstructed (=0). No fiducial cut is done on D1, D2, D3 or D4, as more restrictive fiducial cuts are done on T5 and RICH, which ensures that other fiducial cuts would be automatically satisfied.

5.4.3 Main fiducial cut on FS and MRS

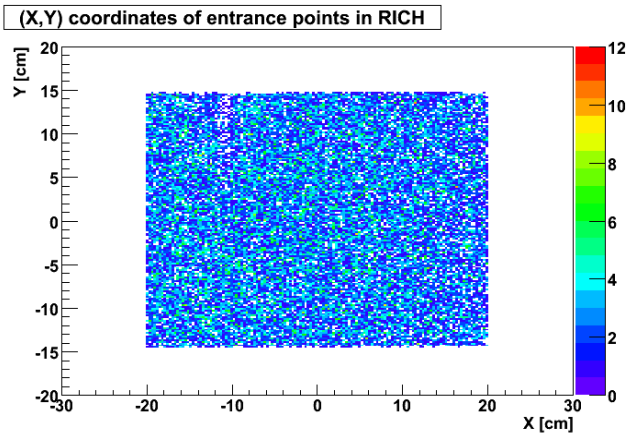

Figure 5.4: The cut on entrance points of FS tracks at the back of RICH. Setting: 2B1723, p+p $\sqrt{s} = 62.4$ GeV

The narrowest part of the spectrometers is normally cut, to ensure that no tracks that could have scattered in the detector/magnet walls will be included, and also to ensure good geometrical acceptance corrections. In the MRS, the cut is done on the back of TPM2. For the Y coordinate $Y = [-5, +8]$ cm is used. For the X coordinate, two different cuts are used: $X = [-26, +18]$ cm for negative particles in A settings/positive particles in B settings and $X = [-18, +32]$ cm for negative particles in B settings/positive particles in A settings. In the forward spectrometer, the limiting geometrical entities are RICH and T5. The RICH has a lower ring reconstructing efficiency close to the walls, so a fiducial cut $X = [-20, +20]$ cm, $Y = [-15, +15]$ is done on incoming tracks projected from T5. A fiducial cut is also done on T5: $X = [-24.5, +24.5]$ cm and $Y = [-14, +14]$ cm. Together these two cuts are restrictive enough to make other fiducial cuts on the FS superfluous and are included in the acceptance maps.

5.5 Pointing cuts

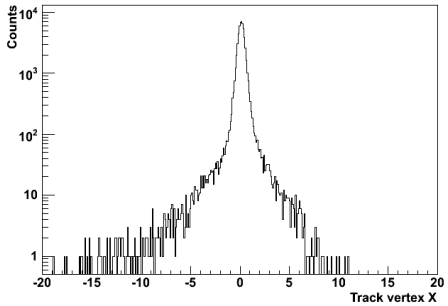

Figure 5.5: Vertex back projection, x-direction. Setting: 2B1723, p+p $\sqrt{s} = 62.4$ GeV.

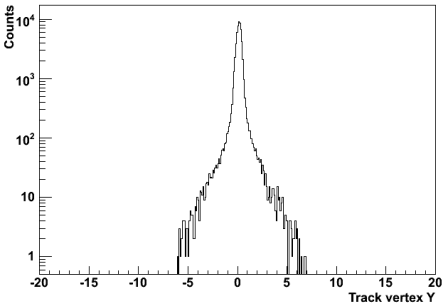

Figure 5.6: Vertex back projection, y-direction. Setting: 2B1723, p+p $\sqrt{s} = 62.4$ GeV.

The back projection of tracks to the vertex is a very sharp Gaussian-like distribution in both directions normal to the track. In the FS, the projection is done towards the (x, y) plane with constant $z = z_{CC}$. The distributions of the intersection points in x and y directions are Gaussian-like, with centroids x_{mean} and y_{mean}, and is slightly wider in the x-direction due to uncertainties in CC vertex location and in track extrapolation in the bending direction. Tracks pointing outside a given number of standard deviations (5σ) from the centroids are removed. Mathematically, the condition in the FS can be expressed:

$$\left(\frac{x - x_{mean}}{\sigma_x}\right)^2 + \left(\frac{y - y_{mean}}{\sigma_y}\right)^2 < n_\sigma^2 \tag{17}$$

with $n_\sigma = 5$

In the MRS, the back-projection is done to the (y, z) plane where $x = 0$, the Gaussian distributions are in y and z coordinates and the condition is:

$$\left(\frac{y - y_{mean}}{\sigma_y}\right)^2 + \left(\frac{(z - z_{CC}) - (z - z_{CC})_{mean}}{\sigma_z}\right)^2 < n_\sigma^2 \tag{18}$$

This partially eliminates multiply scattered tracks, weak decay products and knockout-protons in the beam pipe. As the Gaussians x (z) and y need not have the same standard deviation, pointing cuts are also called *elliptic cuts*.

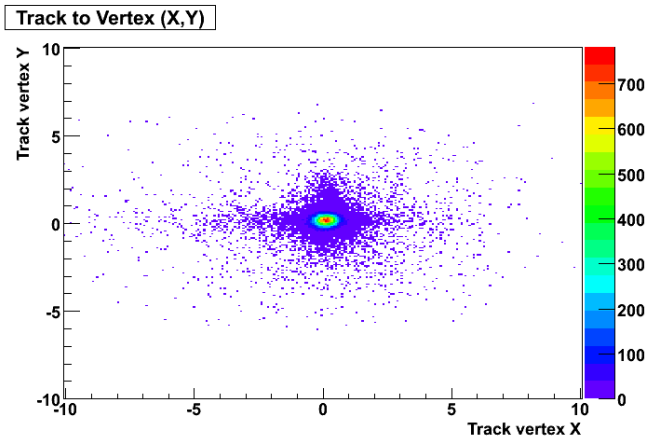

Figure 5.7: Track to vertex back projection in (x,y). Setting: 2B1723, p+p $\sqrt{s} = 62.4$ *GeV*.

There is a slight momentum dependence in the width of the Gaussians, so the flat cut is taken relatively wide in order not to discriminate low-p_T particles.

5.5.1 χ^2 cut

In both spectrometers, a cut is done on the χ^2, which is calculated during final track refit.

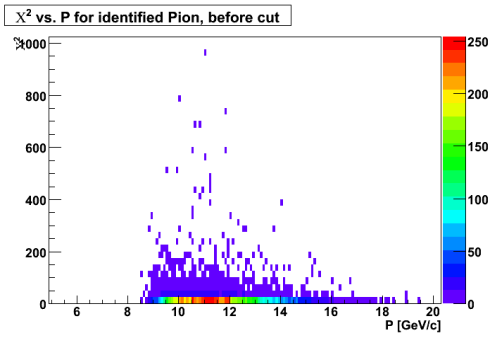

Figure 5.8: χ^2 vs p, before cut. Setting: 2B1723, p+p $\sqrt{s} = 62.4$ GeV

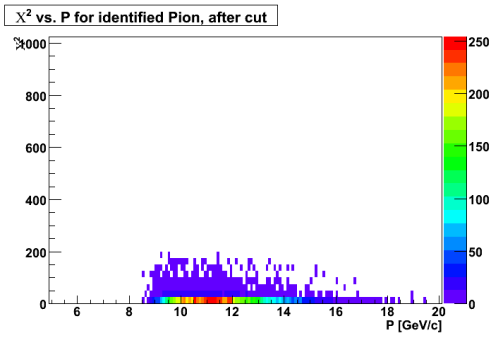

Figure 5.9: χ^2 vs p, after cut. Setting: 2B1723, p+p $\sqrt{s} = 62.4$ GeV

Such tracks might result from in-flight decays, overlapping/unresolved tracks and multiple scatterings, giving a continuous tail in χ^2. Two different formulas are used, depending on spectrometer.

In the MRS the requirement is:

$$\chi^2(p) < 10 \times (A_{MRS} + \frac{B_{MRS}(m^2 + p^2)}{p^4}) \tag{19}$$

In the FS:

$$\chi^2(p) < 4 \times (A_{FS} + \frac{B_{FS}}{p}) \tag{20}$$

where A and B are empirical constants. These parameters are calculated from GEANT simulations with all physics turned on. Few tracks are affected by this cut, as the pointing cuts applied before already take care of most of the tracks that have undergone scatterings or decays. The momentum dependence reflects the fact that low momentum tracks are more prone to scatterings or in-flight decays.

5.5.2 TOF related cuts

In TOFW and H2, there are dead scintillator slats, causing geometrical areas without sensitivity. These are not always the same and are usually marked and removed in the acceptance map. In figure 5.10, a slat with low efficiency, but not completely dead, can be seen close to slat number 50. Such slats are not marked as dead and will distort the spectra. To minimize this problem, a cut in the slat range was imposed in both datasets. Slats $[33, 113]$ is used in the p+p $\sqrt{s} = 62.4$ GeV analysis, and slats $[46, 94]$ in p+p $\sqrt{s} = 200$ GeV analysis.

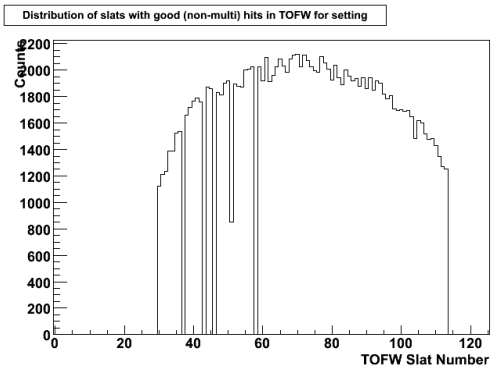

Figure 5.10: Dead slats in TOFW.
Setting: 90A700, $\sqrt{s} = 62.4$ GeV

Tracks extrapolated from tracking detectors to point at a slat in the horizontal direction, but not giving a signal in this same slat, are removed. This loss will have to be corrected for (the pointed slat correction). As mentioned, the TOF slats have a PMT at each end, and therefore the y-coordinate of a hit can be determined from the time difference between the upper and lower tube. If a sufficient mismatch between the pointed y-coordinate and the measured y-coordinate is seen, the track is discarded.

5.6 Particle identification

While some measurables like high-p_T suppression can be studied from unidentified charged hadron spectra, identified particle spectra have more features. The trade-off is a smaller $y - p_T$ range covered, as PID detectors have a limited momentum range in which they can properly separate hadron species.

5.6.1 Particle identification by RICH

All particle identification in this analysis is based upon the fact that hadrons of different masses have different velocities at the same momentum:

$$p = \gamma m v = \frac{m\beta c}{\sqrt{1-\beta^2}} \tag{21}$$

which can be rearranged:

$$\frac{1}{\beta} = \sqrt{\frac{m^2}{p^2} + 1} \tag{22}$$

The Cherenkov radiation generates a lightcone, whose opening angle is related to the refractive index n and the velocity β as:

$$cos\theta = \frac{1}{\beta n} \tag{23}$$

and this cone is projected on the focal plane of the RICH detector, forming a ring of radius

$$r = Ftan\theta \tag{24}$$

where F is the focal length. Combining all above equations and solving for the ring radius r as function of p, n and m:

$$r = Ftan(arccos(\frac{1}{n}\sqrt{\frac{m^2}{p^2} + 1})) \tag{25}$$

With experimental ring radius and momentum uncertainties, it becomes

$$r = Ftan(arccos(\frac{1}{n}\sqrt{\frac{m^2}{(p \pm dp)^2} + 1})) \pm dr \tag{26}$$

The uncertainties dr and dp are found from visual inspection of data, and are tabulated in table 5.3.

dr $(all,\ cm)$	Pion dp (GeV/c)	Kaon dp (GeV/c)	Proton dp (GeV/c)
0.45	0.4	0.6	0.8

Table 5.5: RICH PID parameters

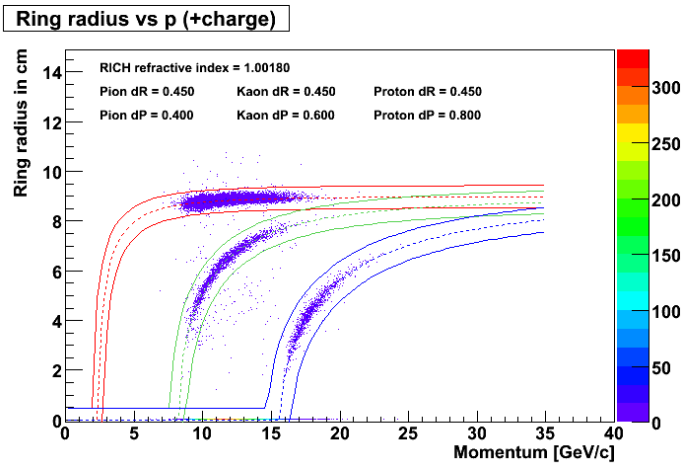

Figure 5.11: Pion (red), kaon (green) and proton (blue) distributions. Particles within respective curves and momentum limits stated below are identified. Setting: 2B1723, p+p $\sqrt{s} = 62.4$ GeV

As mentioned, the RICH is used as a particle identification detector (PID) in the FS spectrometer at small angles. Ring radius is plotted versus momentum. A band of particles appear around the theoretical curve, and two new curves with characteristic errors are drawn above and below. All particles inside these curves and the momentum PID limits are taken to be of the species corresponding to the theoretical curve, as long as PID distributions for different species don't overlap.

Curves and particle distributions must be inspected, as the RICH refractive index is sensitive to the RICH gas mixture and pressure, which can vary between runs. In these datasets, $1.00155 < n < 1.00180$. The threshold velocity for having a Cherenkov cone is $\theta = 0$ or $cos\theta = 1$ and therefore $\beta_{Thr} = \frac{1}{n}$. A refractive index of 1.00180 gives $\beta_{Thr} = 0.9982$, equivalent to a Lorentz factor $\gamma_{Thr} = \frac{1}{\sqrt{1-\beta^2}} = 16.7$. Using the relativistic momentum relation $p = \gamma m \beta c$ gives the momentum threshold for a given particle mass:

Particle	Mass (MeV)	γ_{Thr}	p_{Thr} (GeV/c)
$e^{\pm}$	0.511	16.7	0.00085
$\mu^{\pm}$	105.66	16.7	1.76
$\pi^{\pm}$	139.57	16.7	2.33
$K^{\pm}$	493.667	16.7	8.22
$p, \bar{p}$	938.272	16.7	15.6

Table 5.6: RICH momentum thresholds

These thresholds are relatively insensitive to a change in n within the limits seen in this analysis.

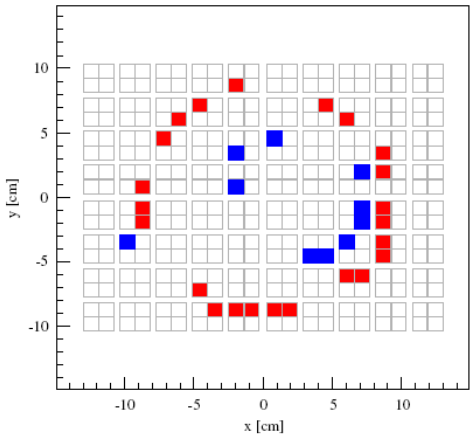

Figure 5.12: Example of two reconstructed rings in RICH. Pixels hit by Cherenkov light are colored. Figure from [32].

A few GeV/c above this threshold, there is a 97% ring reconstruction efficiency [32], this is the "direct" PID. In the intermediate region just above the threshold, the response is less than 97% efficient. Protons will have a high threshold for direct PID and a lot of low momentum protons will not generate a ring. Sufficiently far above pion and kaon thresholds, these might be identified indirectly as protons (very few deuterons will appear at momenta below the proton threshold). Any particle under the upper RICH curve until 20 GeV is taken as a proton. Indirect PID protons are contaminated with 3% of pions and 3% of kaons not generating a ring, and this RICH contamination correction has to be estimated and subtracted from the ringless particles. At some point, ring distributions for different species will intersect and PID high limits are set here. Few particles have momenta over 30 GeV. The above considerations translate into the following PID limits for RICH:

Species	Low limit (GeV/c)	High limit (GeV/c)
Pions	5	20
Kaons	10	20
Protons (direct)	15	30
Protons (indirect)	10	20

Table 5.7: RICH PID limits

With a more sophisticated RICH PID algorithm, π/K separation could be accomplished even beyond $p = 20GeV/c$, but the achieved separation was considered sufficient

for this analysis. Note that the high field settings 2A/B 3450 and 4A/B 3450 were only used for proton PID, as most of the pions and kaons are above the PID limits.

5.6.2 Particle identification by TOFW

Starting from the same relation

$$p = \gamma m v = \frac{m\beta c}{\sqrt{1-\beta^2}} \tag{27}$$

squaring

$$p^2 = \frac{m^2\beta^2 c^2}{1-\beta^2} \tag{28}$$

and rearranging, gives

$$\frac{p^2}{c^2}(\frac{1}{\beta^2} - 1) = m^2 \tag{29}$$

It is seen that at higher momenta, the uncertainty in m^2 vs p grows for higher p, due to a finite timing resolution. When distributions of species overlap too much, PID cannot be done. For protons, multiple scattering also cause a broadening at $p < 1.0$ GeV/c, clearly visible in figures 5.14 and 5.17.

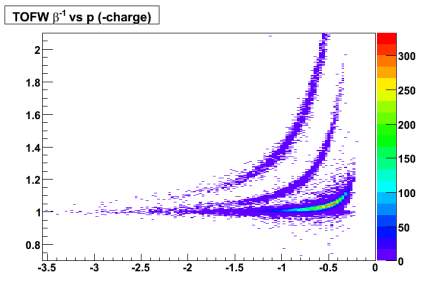

Figure 5.13: Native variable $\frac{1}{\beta}$ vs p in TOFW. Setting: 90A700, negatives, p+p $\sqrt{s} = 62.4$ GeV

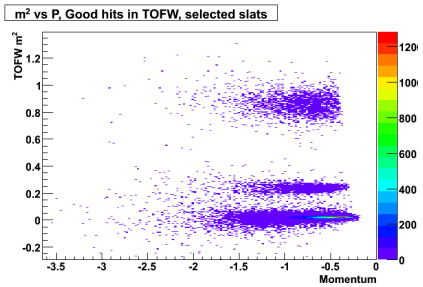

Figure 5.14: m^2 vs p distributions in TOFW for same setting. Setting: 90A700, negatives, p+p $\sqrt{s} = 62.4$ GeV

There are four time of flight devices in BRAHMS: H1, H2 in the FS and TOFW and TFW2 in the MRS. Of these, TOFW and H2 is used in this analysis. The m^2 vs p distribution is used for doing PID in this thesis. In a perfect world, all particles would line up at their theoretical m^2 values.

Pion m^2 (GeV^2/c^4)	Kaon m^2 (GeV^2/c^4)	Proton m^2 (GeV^2/c^4)
0.01948	0.2347	0.8804

Table 5.8: Theoretical m^2 of pions, kaons and protons.

In a real world, they have a Gaussian distribution with a strongly p-dependent width around a measured mean value equal to the theoretical m^2 plus some offset dm^2.

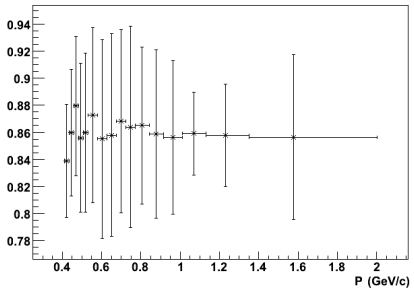

Figure 5.15: Gaussian centroids in m^2 for p slices. Protons, setting 90A700, p+p $\sqrt{s} = 62.4$ GeV

The m^2 distribution is divided into momentum slices and a combination of three Gaussians are used to fit the three particle distributions for each slice. For a candidate to be identified as a given species, it must satisfy the following criteria:

- Its m^2 value must be within 3σ from its measured mean m^2 value at the given slice in p. This limits the width in m^2 of PID at lower momenta.
- For a given slice, a PID limit in m^2 is set when the amplitude of the neighboring Gaussians reaches a given percentage of the amplitude of the species of interest. This limits the width in m^2 of PID at higher momenta. A limit of 5% contamination was used in this analysis.
- For the particle yield in a slice to be fittable, the uncontaminated region must contain at least $\frac{1}{3}$ of the total integrated yield for a given species at that momentum slice. As the contamination usually increases monotonically for increasing

momenta, this constitutes a momentum cutoff for the PID.

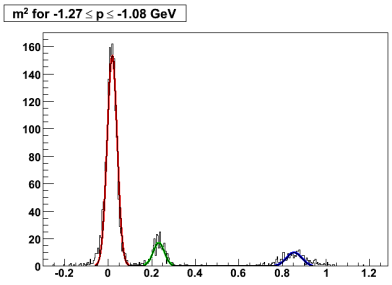

Figure 5.16: A momentum slice with fitted gaussians for pion (red), kaon (green) and proton (blue) distributions in m^2. Setting: MRS90A700, negatives, p+p $\sqrt{s} = 62.4$ GeV

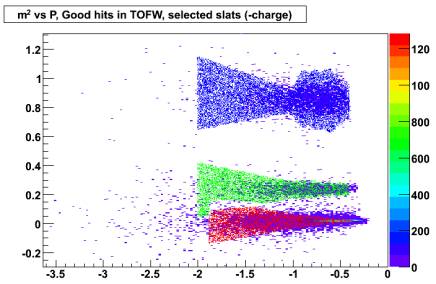

Figure 5.17: m^2 vs p with overlaid test particles (colored areas) to test the PID algorithm. Setting: 90A700, negatives, p+p $\sqrt{s} = 62.4$ GeV

Now, with a maximum contamination specified, one can do PID even if the distributions intersect slightly. To test the fits, simulated particles are overlaid the m^2 vs P distributions, seen in figure 5.17. This procedure demands corrections for particle losses, described in section.

5.6.3 Particle identification with H2 and RICH

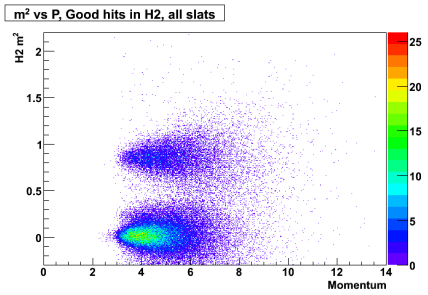

Figure 5.18: m^2 vs p in H2. Pions and protons are clearly visible, while kaons are contaminated heavily with pions. Setting: 4B608, p+p $\sqrt{s} = 62.4$ GeV

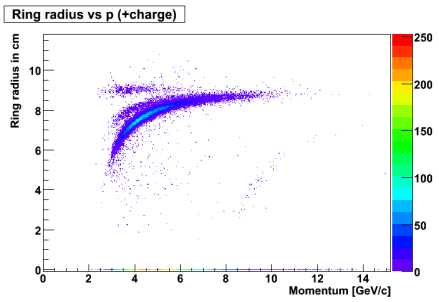

Figure 5.19: Ring radius vs p plotted for 4B608, p+p $\sqrt{s} = 62.4$ GeV. Notice electrons and muons visible above the pion distribution, and ring-0 kaons and protons.

In the low field settings at 4 and 6 degrees, the particle momenta are too low for most particles other than pions to be directly identified in the RICH by the standard

procedure. In H2, pions/kaons can be separated from protons with the procedure from the previous section. To also identify kaons, the PID from H2 and RICH are combined. Protons and kaons will generate ring-0 hits in RICH. A ring-0 track not identified as a proton in H2 will be identified as a kaon. The ring-0 kaons are contaminated by ring-0 pions and protons not identified in H2 and this contamination is estimated and subtracted. For obvious reasons, no attempt to identify kaons directly in H2 has been done for this analysis.

Species	Low limit (GeV/c)	High limit (GeV/c)
Pions	4	20
Kaons	4	6.8
Protons (H2)	4	6.8

Table 5.9: PID limits for H2 in combination with RICH

Because of possible muon contamination, the pion PID is started at 4 GeV/c., where muons are getting scarcer. The PID momentum range for the two other species was restricted to $4 - 6.8\ GeV/c$, in order to extract the best possible spectra.

5.7 Acceptance

No experimental setup detects all particle species at all momenta at all angles. A purely geometrical correction, the acceptance is a function of these variables (p, θ), and it is critical in using measurements to reconstruct physical reality. Large acceptance detectors like the ATLAS at LHC are often called 4π detectors, as they cover nearly the entire solid angle. Such detectors can reasonably completely reconstruct entire events. BRAHMS is on the opposite end of the scale, it is like looking through a keyhole (small solid angle) with a magnifying glass (high precision measurements) at the reaction zone from many different angles. Statistical averages over many collisions can then be obtained. Each spectrometer will often only see a single particle or even no particles in an event. BRAHMS can identify charged particles at more forward angles, i.e. higher pseudorapidities, than the other detectors at RHIC and is in that fashion unique.

To describe the geometric coverage of the detector, i.e. the probability of pions, kaons, protons and their antiparticles to hit a detector and physically traverse it to allow registration at a certain momentum and angle, an acceptance map is used. The map is usually constructed in the physically interesting variables (y, p_T) or (y, m_T), which can be trivially computed from (p, θ) From this map, the numbers of particles seen in BRAHMS runs translate into the complete statistical yield of a number of reactions. The map is generated from a simulation of the detector, where test particles are "thrown" over a solid angle $\Delta\phi$ that is known to be somewhat larger than the sensitive areas of the detector. No physical effects are included, except deflection in the magnets. The particles that make it through and pass all fiducial cuts in magnets and detectors are registered as "accepted". The acceptance is then defined as:

$$Acc(y, p_T) = \frac{\Delta\phi}{2\pi} \frac{Accepted(y, p_T)}{Thrown(y, p_T)} \tag{30}$$

It is important to note that collisions occur over an extended range in the z-direction. Some limits are set at where from to include tracks. These are called vertex limits, and need not be symmetrical around 0. The acceptance is not the same for different vertex z-values. This fact is remedied by introducing narrow vertex bins with different acceptance $Acc(y, p_T)_{v,s}$. Events inside each z-interval are then treated as if seeing a constant acceptance correction, which is a good approximation to the real acceptance which changes continuously with z.

Mean accuracy	2%
Vertex bins	5 cm
Vertex limits (Z)	$\pm$30 cm
p_T bins	25 MeV
Rapidity slices Δy	0.01

Table 5.10: Acceptance maps

A finite number of test particles are thrown, resulting in a finite statistical accuracy in the bins of the acceptance map. The mean value of this accuracy is quoted in percents. The acceptance will stay relatively constant in "central" regions of the map and fall off at the edges. A cut to remove bins with worse accuracy than a given limit is imposed.

5.8 Corrections

The number of reconstructed and identified particle tracks must be corrected for a large number of physical effects and also some mathematical/numerical inefficiencies. A thorough discussion follows.

5.8.1 Weak in-flight decays, multiple scattering and absorption

Weak decays, multiple scattering with materials and absorption effects will reduce the number of observed particles. These effects cannot be evaluated independently and factorization gives incorrect results. The combined effect of taking all processes into account simultaneously is evaluated using GEANT simulations. The physical effects considered are most significant for low-momentum particles, and will also depend on the path length of the track. FS tracks will therefore have larger corrections than MRS tracks at the same momentum. Pions and kaons have close to identical behavior with their antiparticles, while proton and antiprotons have slightly different interactions with materials, due to annihilation of antiprotons. Knock-out protons from trigger slats and beam pipe are assumed to give a contribution negligible in the p_T region measured by BRAHMS [33]. GEANT simulations have been done and correction graphs $C_{GEANT}(p)$ (or histograms $C_{GEANT}(y, p_T)$, any correction as a function of p can be transformed into

a function of (y, p_T) when the angle θ is known) are available for different spectrometer settings, particle species and momenta. In figures 5.20-5.26, GEANT corrections are shown for all species in MRS and FS. Settings shown are 90A700 for MRS and 2B1723 (2A1723 for antiprotons) for FS, both p + p $\sqrt{s} = 62.4$ GeV.

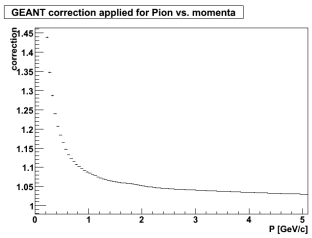

Figure 5.20: GEANT correction for pions in MRS.

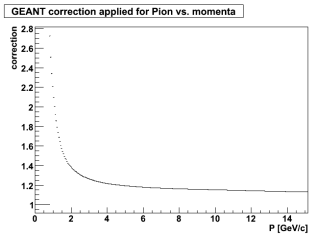

Figure 5.21: GEANT correction for pions in FS.

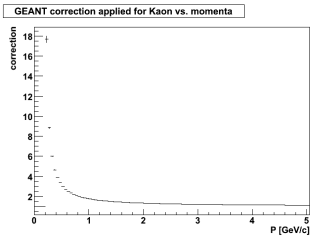

Figure 5.22: GEANT correction for kaons in MRS. Setting: 90A700, p + p $\sqrt{s} = 62.4$ GeV

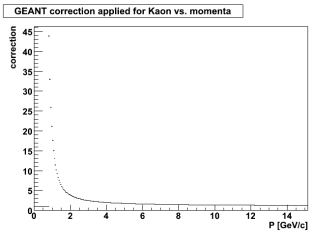

Figure 5.23: GEANT correction for kaons in FS. Setting: 2B1723, p + p $\sqrt{s} = 62.4$ GeV

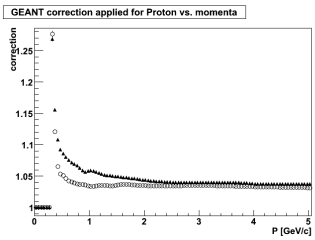

Figure 5.24: GEANT correction for protons (circles) and antiprotons (triangles) in MRS. Setting: 90A700, p + p $\sqrt{s} = 62.4$ GeV

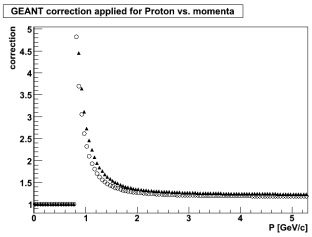

Figure 5.25: GEANT correction for protons (circles) and antiprotons (triangles) in FS. Setting: 2A1723 & 2B1723, p + p $\sqrt{s} = 62.4$ GeV

5.8.2 Tracking efficiency

Neither the MRS nor the FS are 100% efficient in reconstructing tracks. In the MRS, this inefficiency has been studied by inserting simulated tracks from GEANT into real events on the raw data level and looking at the reconstructing ratio.

$$\varepsilon_{TREFF} = \frac{N_{reconstructed}}{N_{inserted}} \tag{31}$$

The tracking efficiency in the MRS is the product of the tracking efficiencies in the two TPMs.

$$\varepsilon_{TrMRS} = \varepsilon_{TPM1} \times \varepsilon_{TPM2} \tag{32}$$

The MRS efficiency is parametrized as function of hit density, which is low for p+p collisions. The efficiency ε_{TrMRS} is about 95%. Further information about MRS tracking efficiency can be found in [34].

In the FS, either T2 or T3 can be used to match tracks with T4. In this analysis, T2 is used. Tracking and matching efficiencies for each tracking station in the FS were calculated by constructing full tracks using only three stations and evaluating the efficiency of the fourth station. The overall efficiency, calculated as:

$$\varepsilon_{TrFS} = \varepsilon_{T1} \times \varepsilon_{T2} \times \varepsilon_{T4} \times \varepsilon_{T5} \tag{33}$$

is about 80-90%. Histograms with tracking efficiencies for different settings are available as a correction for the FS. The local x-position in a tracking station and the track entrance angle α_y are used as variables. For each observed track, the efficiency is evaluated and the track momentum is recorded. A distribution of tracking efficiency vs

momentum is constructed and parametrized into a momentum dependant efficiency correction $\varepsilon_{TREFF}(p)$. A more comprehensive treatment of FS tracking efficiencies can be found in [35].

5.8.3 PID detector inefficiency

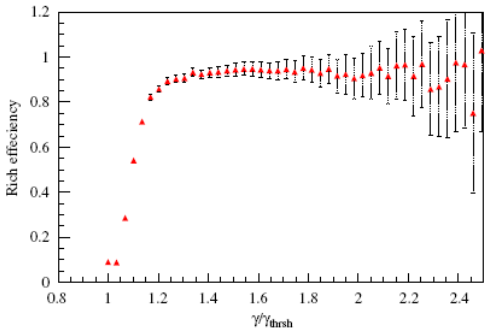

Figure 5.26: Measured efficiency for RICH. Figure from [32].

As mentioned, the RICH detector is known to be $\varepsilon_{RICH} = 0.97$ effective in detecting Cherenkov cones from particles with momenta a few GeV/c over the threshold value. Direct PID yields will have to be multiplied with $C_{DET.EFF} = \frac{1}{\varepsilon_{RICH}} = \frac{1}{0.97}$ as a correction. For the transition region, the response is parametrized [32], but the parametrization is not used in PID in this analysis, since RICH only is used for PID for momentum well above threshold in this thesis for pions and kaons. For the protons, everything under the curve upper proton curve can be taken as a candidate proton, and RICH contamination (see section 5.8.5) subtracted.

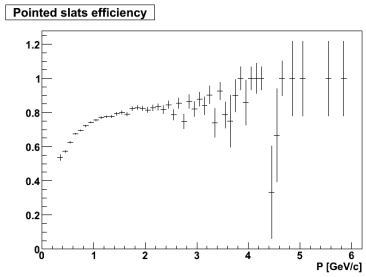

Figure 5.25: Slat efficiency for TOFW. Setting: 45B1050, negatives.

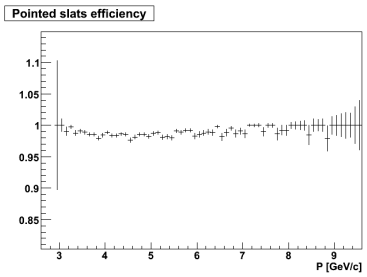

Figure 5.26: Slat efficiency for H2. Setting: 4B608.

Also, H2 and TOFW are not fully efficient in generating a good signal when a slat is struck by a particle. This efficiency is not constant, but momentum dependant. For

p+p, H2 has an efficiency of about 0.98. TOFW has a strongly momentum dependant effiency. Two corrections corresponding to the pointed slat cut and the pointed slat Δy coordinate must be done. The slat Δy correction is usually very small (3σ), while the pointed slat correction can be substantial, especially in TOFW at low momenta. Tracks giving multiple hits in same slat are also discarded, which has to be corrected for, but this is a very small correction in p+p. All these corrections are combined into the Slat Efficiency $\varepsilon_{SLAT:EFF}(p)$, and the PID detector inefficiency is given by $C_{DET.EFF} = \frac{1}{\varepsilon_{SLAT:EFF}(p)}$.

5.8.4 PID algorithm inefficiency

A mathematical correction, the algorithms used for doing TOF PID are not 100% efficient, as the true number of identified particles of a species is different from the counts inside the area overlaid test particles in figure (5.17). First, it is noted the total number of particles measured (here denoted $N_\pi(m^2) + N_K(m^2) + N_P(m^2)$) in a slice in (m^2, p) are not equivalent to sum of fitted Gaussian functions $(f_\pi(m^2) + f_K(m^2) + f_P(m^2))$, and therefore integrals also differ. This ratio, which is a function of p, is expressed in the *"FitCorrection"*

$$FitCorrection(p) = \frac{\int_{m^2_{low}}^{m^2_{high}} (N_\pi(m^2) + N_K(m^2) + N_P(m^2))dm^2}{\int_{m^2_{low}}^{m^2_{high}} (f_\pi(m^2) + f_K(m^2) + f_P(m^2))dm^2} \tag{34}$$

where m^2_{high} the highest and m^2_{low} are the lowest m^2 taken into consideration in the fit (example: $m^2 = [-0.5, 2]$). Furthermore, the tail is cut when the amplitude of another Gaussian reaches an arbitrary percentage (in this analysis 5%) of the amplitude for the particle species of interest and the Gaussians are contaminated by other Gaussians. This reasoning gives the following loss/contamination *Correction*, a function of p, for all species, exemplified with pions:

$$Correction_\pi(p) = \frac{\int_{m^2_{low}}^{m^2_1} f_\pi(m^2)dm^2 + \int_{m^2_2}^{m^2_{high}} f_\pi(m^2)dm^2 - \int_{m^2_1}^{m^2_2} \left[f_K(m^2) + f_p(m^2)\right] dm^2}{\int_{m^2_1}^{m^2_2} N_\pi(m^2)dm^2} \tag{35}$$

where $m^2_1 = Max\left[(m^2_\pi - 3\sigma), m^2_{\pi,low}\right]$, where $m^2_{\pi,low}$ is the lowest uncontaminated pion m^2 and $m^2_2 = Min\left[(m^2_\pi + 3\sigma),\ m^2_{\pi,high}\right]$, $m^2_{\pi,high}$ being the highest uncontaminated pion m^2.The final corrected yield for pions is then given by

$$Y_{\pi,corrected}(p) = (1 + Correction_\pi(p) \times FitCorrection(p)) \times Y_{\pi,uncorrected} \tag{36}$$

where $y_{\pi,uncorrected}$ is equal to the denominator in eq.(35).

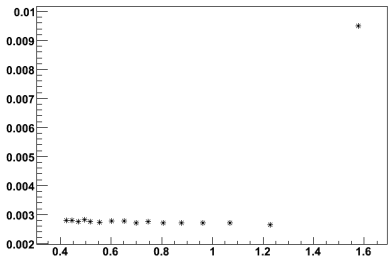

Figure 5.27: $Correction(p)$, for protons. Setting: 90A700, p+p $\sqrt{s} = 62.4$ GeV

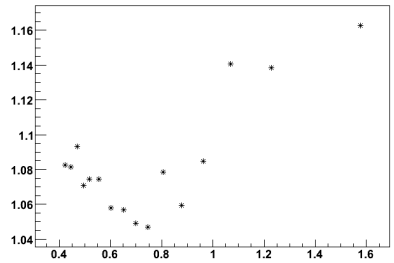

Figure 5.28: $FitCorrection(p)$. Setting: 90A700, p+p $\sqrt{s} = 62.4$ GeV

A multiplicative correction for the yields is then:

$$C_{PID.ALG}(p) = \frac{Y_{\pi,corrected}(p)}{Y_{\pi,uncorrected}(p)} = (1 + Correction_{\pi}(p) \times FitCorrection(p)) \quad (37)$$

5.8.5 RICH contamination

As mentioned, three percent of directly identified kaons and pions above the K threshold will not generate a ring and be misidentified as protons. These will have to be removed from the indirect protons. In the first analysis iteration, RICH PID (ring radius vs momentum) is done for pions and kaons for each setting. The contamination in the indirect proton region is found by taking 3% of the pion and kaon momentum spectra (uncorrected for RICH inefficiency). In the following figures, the contamination relative to indirectly identified protons (all ring zero particles - contamination) is plotted.

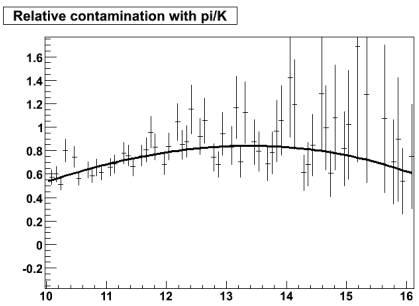

Figure 5.29: Parametrised RICH contamination, antiprotons with 3-degree polynomial fit. Setting: 2A1723, p+p $\sqrt{s} = 62.4\ GeV$. This setting sees the fragmentation peak, where antiprotons are very scarce.

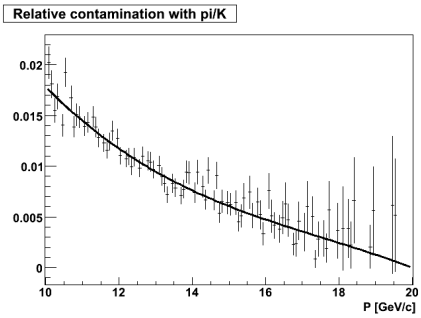

Figure 5.30: Corresponding positive setting with 3-degree polynomial fit. As protons are are abundant in the fragmentation region, the relative contamination is small. Setting: 2B1723, p+p $\sqrt{s} = 62.4\ GeV$

$$Cont_R(p) = \frac{0.03N_\pi(p) + 0.03N_K(p)}{N_{Ring-0}} \tag{38}$$

This quantity is parametrized as a function (3-degree polynomial has been used), and $(1 - Cont_R(p))$ is used as a multiplicative correction for the total yields.

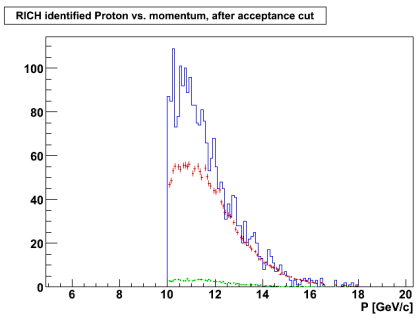

Figure 5.31: Momentum dependant absolute contamination of indirect $\bar{p}$, plotted together with $\bar{p}$ yield (blue), assuming 3% inefficiency. π^- contamination in red, K^- contamination in blue. The corrected $\bar{p}$ yield is the upper curve minus the two lower curves. Setting: 2A1723, p+p $\sqrt{s} = 62.4$ GeV

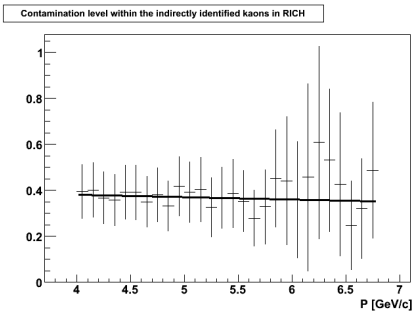

Figure 5.32: Kaon contamination by ringless pions in RICH. Setting: 4B608, p+p $\sqrt{s} = 62.4$ GeV

In settings where H2 and RICH are used together, the RICH contamination of indirect kaons by ring-0 pions is estimated in a similar way and parametrized with a linear function in the interval $p = 4 - 6.8$ GeV/c. One also have to subtract protons not identified in H2. The probability of detection is 98%, thus 2% of identified protons in H2 must be subtracted from the kaons ("identified" includes the measured protons times the PID algorithm correction). The kaon contamination is thus given by the equation:

$$Cont_R = \frac{0.03N_\pi(p) + 0.02N_{H2protons}(p)}{N_{Ring-0}} \tag{39}$$

It is well fit by a linear function, and $(1-Cont_R)$ is used as a multiplicative correction for the total yields.

5.8.6 CC inefficiency

In order to extract the differential invariant yields per event $\frac{d^2n}{2\pi p_T dp_T dy}$, the p+p spectra must be normalized. This normalization is done relative to the total inelastic cross section σ^{pp}_{Inel}, which is extracted from PYTHIA simulations. However, the measured invariant yields per CC event are not identical to the true invariant yields per inelastic collision, as the physical layout of the CC minimum bias trigger disfavors low multiplicity events. A correction can be deduced the following way, as in [36]:

The measured number of counts in the spectrometer in a (y, p_T) interval is

$$n(y, p_T) = L\sigma(y, p_T)Acc(y, p_T)P_{TrCC} \tag{40}$$

where L denotes the luminosity, $\sigma(y, p_T)$ is the measured differential cross section in the spectrometer, $Acc(y, p_T)$ the acceptance and P_{TrCC} the probability that a track registered has a CC vertex.

The measured number of counts in the CC detectors is:

$$N_{cc} = L\sigma^{pp}_{Inel}P_{CC} \tag{41}$$

where P_{CC} is the probability for an inelastic collision to produce a valid CC trigger. Interesting here is the ratio between spectrometer and CC measured cross sections:

$$\frac{\sigma(y, p_T)}{\sigma^{pp}_{Inel}} = \frac{n(y, p_T)}{N_{cc}} \frac{P_{CC}}{Acc(y, p_T)P_{TrCC}} \tag{42}$$

Simplifying, the CC inefficiency correction C_{CC} to be multiplied with normalized and acceptance corrected yields per event, is:

$$C_{CC} = \frac{P_{CC}}{P_{TrCC}} \tag{43}$$

A near constant (in species, y and p_T) $C_{CC} = 0.87$ for the $p + p$ $\sqrt{s} = 200$ GeV collisions. The σ^{pp}_{Inel} (41 mb) and the P_{CC} $(70 \pm 5)\%$ can be found from PYTHIA simulations, and the P_{TrCC} has been estimated from reconstructed data to be 80%. A multiplicative correction $C_{CC} = \frac{0.70}{0.80} = 0.87$ is deduced.

The situation is more complicated in the $p+p$ $\sqrt{s} = 62.4$ GeV dataset, due to a non-negligible energy-momentum conservation effect for the higher-p_T particles at forward rapidities. The CCs are here measured to see 12 mb of the σ^{pp}_{Inel} (36 mb, from PYTHIA), so $P_{CC} = (33 \pm 3)\%$. A similar analysis as in $p+p$ $\sqrt{s} = 200$ GeV gives a P_{TrCC} of 0.40 in MRS and in the FS at $p_T < 1$ GeV, so a flat $C_{CC} = \frac{P_{CC}}{P_{TrCC}} = \frac{0.33}{0.40} = 0.82$ can be used here. At forward rapidities and higher transverse momenta, there are specie-dependant deviations from this correction due to a dropping P_{TrCC}. In this dataset, however, only protons are believed to be significantly affected in the FS. Most pions and kaons have $p_T < 1$ GeV at forward rapidities, where the corrections are small. Only a constant C_{CC} of 0.82 has been applied in this thesis since reliable (y, p_T) dependent correction factors for the forward region were not available before the deadline.

5.8.7 Feeddown corrections

BRAHMS detectors are situated several meters away from the interaction region and most hadrons except pions, kaons and protons/antiprotons will have decayed within

reaching them. The most important reactions, leading to secondary contributions to the yields of measured identified hadrons are

$$\begin{aligned} K_S^0 &\rightarrow \pi^+\pi^- \\ \Lambda &\rightarrow p\pi^- \\ \bar{\Lambda} &\rightarrow \bar{p}\pi^+ \end{aligned}$$

These reactions will increase the proton and pion yields in the final spectra. No attempt to correct for these effects has been done, since yields of K_s^0 and Λ are not available as a function of y and p_T and corrections would be heavily model dependant. It has been estimated that at midrapidity in p+p at $\sqrt{s} = 200$ GeV that at most 25% [37] of the protons seen are feed-down from lambdas, while the feed-down contribution to the pion spectra is of the order of a few percent. Secondary protons/antiprotons will have a similar rapidity and p_T distribution as the primary hadrons.

5.9 Assembling datamaps and merging settings

When the most significant corrections are known and handeled, they can be applied on the raw data, which exists in the form of different settings. It is not obvious how to correct and merge these settings into a final spectra, but a procedure commonly agreed on is discussed in this subchapter. The following subcapter closely parallells the discussion in [37].

- For a given $y - p_T$ range within a setting s and a vertex bin v, one has the acceptance correction $Acc(y, p_T)_{v,s}$ and the raw number of recorded counts for a species $n(y, p_T)_{v,s}$.
- There should be no data outside the acceptance and no unphysical irregularities

in the data inside the map.

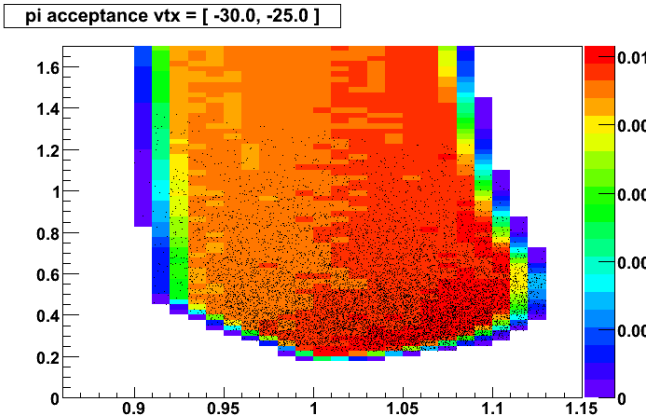

Figure 5.33: Measured π^- (black dots) plotted onto the acceptance map for vertex bin (-30.0 cm, -25.0 cm). Setting: 45B1050, p+p $\sqrt{s} = 62.4$ GeV

- The normalization factor $S_{norm\ v,s}$ from eq. (13) and corrections discussed earlier in this chapter are first combined into a correction histogram for a vertex bin v and a setting s:

$$\begin{aligned} corr(y,p_T)_{v,s} &= S_{norm\ v,s} \times C_{GEANT}(p) \times \frac{1}{\varepsilon_{TR.EFF(P)}} \times C_{DET.EFF}(p) \\ &\quad \times C_{PID.ALG}(p) \times (1 - Cont_R(p)) \times C_{CC} \end{aligned}$$

  Note that not all settings and particle species have all corrections, and if the correction is not relevant for a setting, it is set to 1 (obviously, $Cont_R(p)$ is zero then). Also, a momentum independent $C_{DET.EFF}$ is used for RICH PID.

- This histogram is multiplied with $\frac{1}{2\pi\Delta p_T \Delta y}$ times the acceptance correction for that vertex bin $Acc(y,P_T)_{v,s}$ into the total correction:

$$CORR(y,p_T)_{v,s} = \frac{corr(y,p_T)_{v,s}}{2\pi\Delta p_T \Delta y Acc(y,p_T)_{v,s}}$$

  Δp_T and Δy is the width of transverse momentum and rapidity bins, respectively.

- All correction histogram vertex bins are merged as follows:

$$CORR(y,p_T)_s = \frac{1}{\sum_v \frac{1}{CORR(y,p_T)_{v,s}}}$$

- All raw counts histogram vertex bins are merged as follows:

$$n(y, p_T)_s = \sum_v n(y, p_T)_{v,s}$$

- The total yield $N(y, p_T)_s$ for this setting can now be deduced

$$N(y, p_T)_s = n(y, p_T)_s \times CORR(y, p_T)_s = \frac{\sum_v n(y, p_T)_{v,s}}{\sum_v \frac{1}{CORR(y,p_T)_{v,s}}}$$

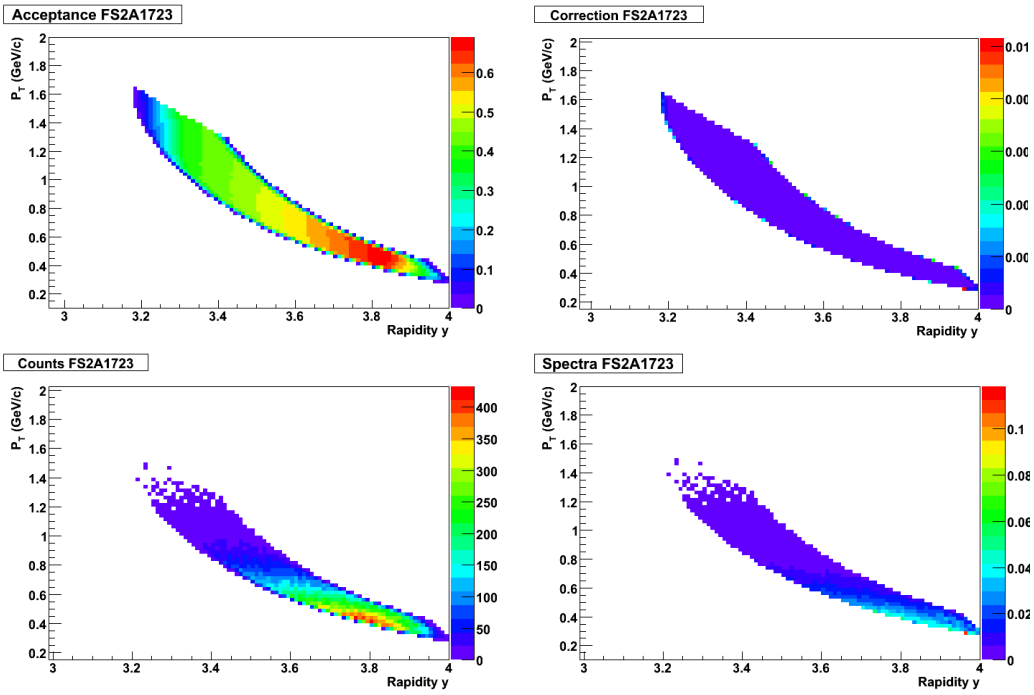

Figure 5.34: π^- acceptance, corrections, counts and spectra.
Setting 2A1723, p+p $\sqrt{s} = 62.4\ GeV$

- The settings s can now be merged together in the same fashion as the vertex bins were merged

$$N(y, p_T) = n(y, p_T) \times CORR(y, p_T) = \frac{\sum_s n(y, p_T)_s}{\sum_s \frac{1}{CORR(y,p_T)_s}}$$

- Some edge effects are inevitable, but the settings should fit smoothly together. If (y, p_T) regions with substantial disagreement between settings or unphysical

behavior are seen, these can be excluded from the fit.

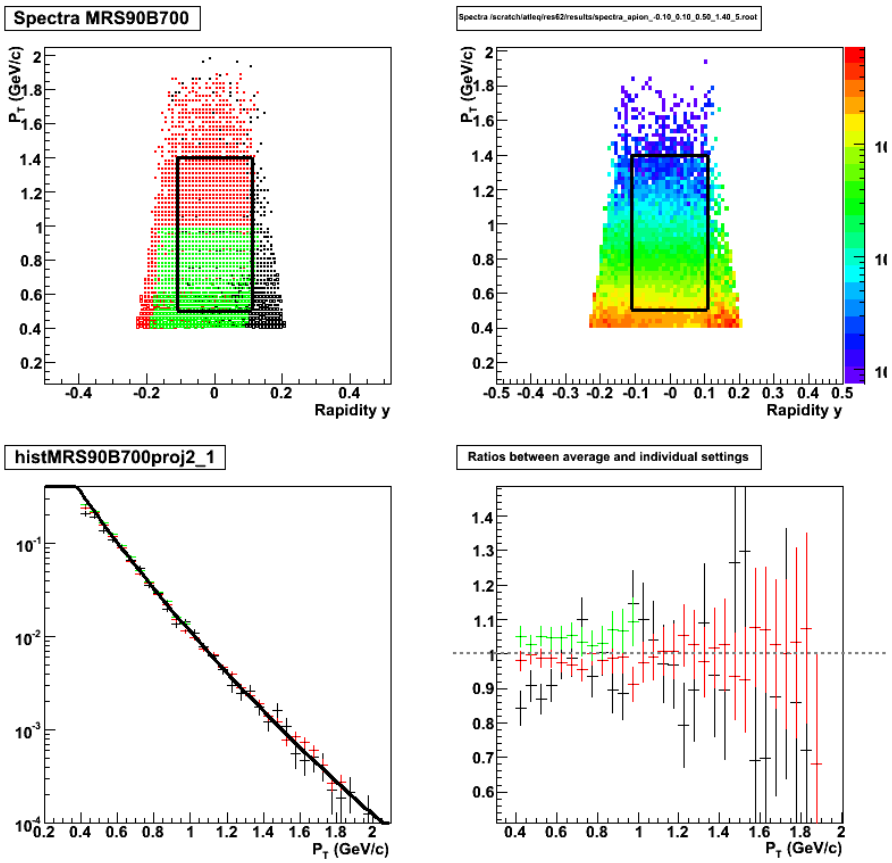

Figure 5.35: Upper left: Counts from three individual settings with MRS in 90°. Upper right: Settings corrected and merged into a invariant spectrum. Lower left: Fitted spectra in p_T, within y-limits $-0.1 < y < 0.1$. Lower right: Ratio between individual settings and average. π^- fit with power law at $-0.1 < y < 0.1$ and $0.5 < p < 1.4$ GeV/c

- Finally, to extract p_T spectra, two rapidity limits are set. All points inside these limits and a given p_T are summed up.

$$N(p_T) = \frac{\sum_{y=y_{low}}^{y_{high}} n(y, p_T)}{\sum_{y=y_{low}}^{y_{high}} \frac{1}{CORR(y,p_T)}} \tag{44}$$

- The spectra are now divided by a factor p_T to become invariant spectra $\frac{1}{2\pi p_T}\frac{d^2N}{dydp_T}$. In the MRS, spectra are slowly changing with rapidity at the same p_T and intervals $\Delta y = 0.20$ or even $\Delta y = 0.40$ can very well be used. In the FS, spectra change rapidly and $\Delta y = 0.1$ should be used as a max interval.

6 Extraction of results

After corrected spectra are obtained, physics can be extracted from them. Obviously, the limited phase space coverage requires extrapolations and approximations. Different choices can greatly affect the final results, and a good, critical physicist must therefore know the limitations of these methods. A discussion of the procedures on extracting yields, ratios and mean p_T is therefore included. The statistical and systematic uncertainties are also discussed at the end of this chapter.

6.1 Hadron $\frac{d^2N}{dydp_T}$maps, p+p $\sqrt{s} = 62.4\ GeV/c$

To show the phase space coverage in y and p_T, the final $\frac{d^2N}{dydp_T}$ maps are shown for all species at both energies.

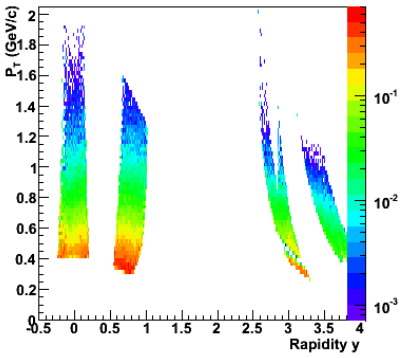

Figure 6.1: π^+ spectrum

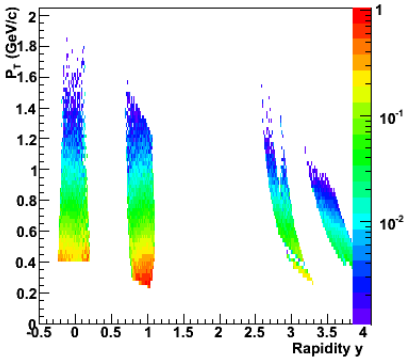

Figure 6.2: π^- spectrum

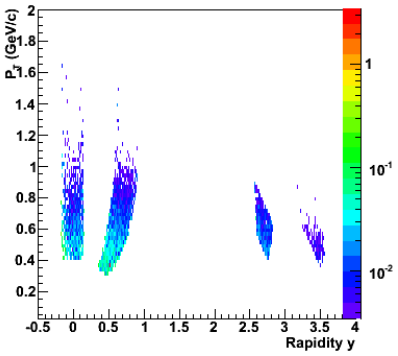

Figure 6.3: K^+ spectrum

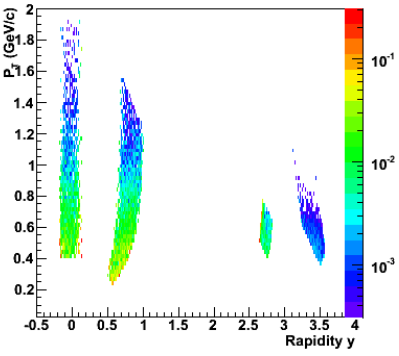

Figure 6.4: K^- spectrum

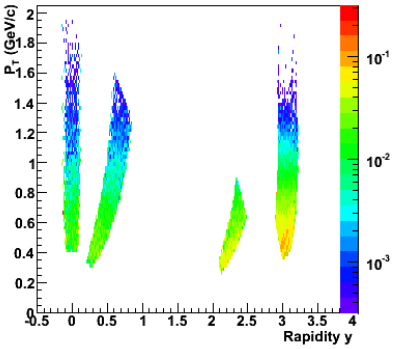

Figure 6.5: p spectrum

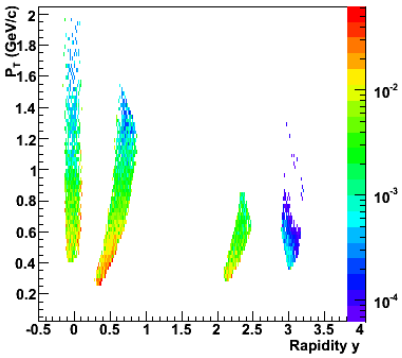

Figure 6.6: $\bar{p}$ spectrum

The different settings appear to fit smooth together and there are no abrupt discontinuities.

6.2 Hadron $\frac{d^2N}{dydp_T}$maps, p+p $\sqrt{s} = 200\ GeV/c$

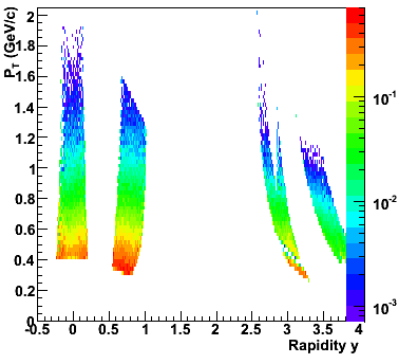

Figure 6.7: π^+ spectrum

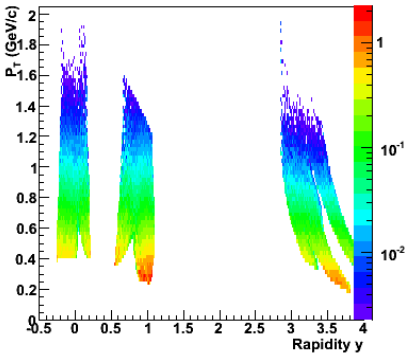

Figure 6.8: π^- spectrum

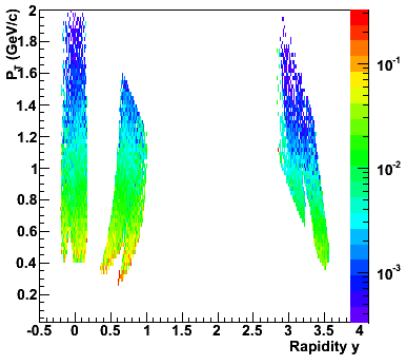

Figure 6.9: K^+ spectrum

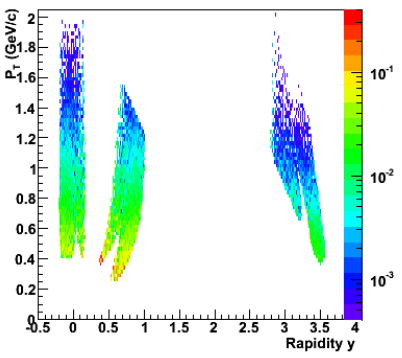

Figure 6.10: K^- spectrum

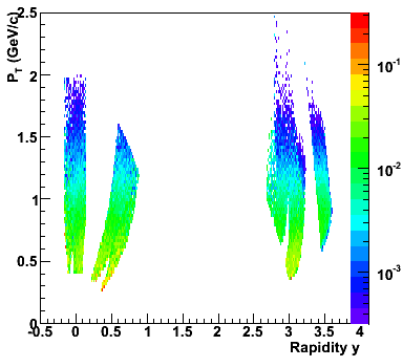

Figure 6.11: p spectrum

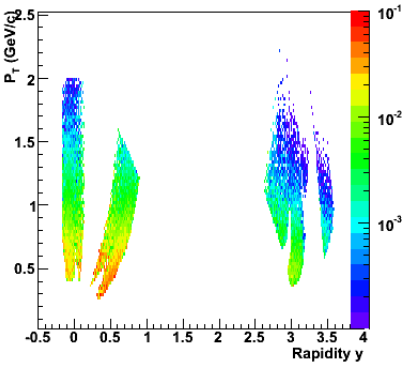

Figure 6.12: $\bar{p}$ spectrum

The p+p $\sqrt{2}$ = 200 GeV/c also look smooth and continous. A larger coverage in especially the forward region can also be seen, due to data taken at more settings.

6.3 Fitting spectra

As the data p_T coverage is not complete, the spectra cannot be directly integrated in p_T in order to obtain the total yield within a rapidity interval. Rather, a fit must be made to a theoretically motivated function.

$$\frac{1}{2\pi p_T}\frac{d^2N}{dydp_T} = f(p_T) \tag{45}$$

This function can then be integrated in order to deduce the actual yield in that rapidity interval.

$$\frac{dN}{dy} = \int \frac{d^2N}{dydp_T}dp_T = \int 2\pi p_T dp_T f(p_T) \tag{46}$$

Different particle species will fit better with different functions. An optimum fit should be found by taking into account the χ^2 of the fit, the p_T coverage and the errors of the fit parameters. If the fit parameters themselves are completely out of the meaningful ranges, the fit should not be used.

Below $p_T \simeq 500MeV/c$ the spectra may have an unphysical dip, which has not been fitted in this analysis. This is a recurrent problem in BRAHMS data analysis and still unresolved.

6.3.1 Exponential in p_T

A p_T exponential is the simplest fit $f(p_T)$ from a thermal source. Note that the inverse slope should not be interpreted directly as the "temperature" of the p+p collision. Exponential spectra are seen even in e^+e^- collisions, which cannot be "thermal" in any ordinary sense. A possible explanation is that the exponential behavior is related to the statistical nature of fragmentation.

$$\frac{1}{2\pi p_T}\frac{d^2N}{dydp_T} = A_1 e^{\frac{-p_T}{T}} \tag{47}$$

6.3.2 Exponential in m_T

An exponential in m_T usually gives better fits than an exponential in p_T, as it takes into account the different masses of the identified hadrons and therefore behaves more realistically at low p_T. It will consistently fit the low-p_T region of most identified particle distributions with a low χ^2. In this analysis, kaons are fit with an exponential in m_T.

$$\frac{1}{2\pi p_T}\frac{d^2N}{dydp_T} = A_2 e^{\frac{-m_T}{T}} \tag{48}$$

Double exponentials in p_T or m_T might be used to describe a system with two sources with different temperatures, however no attempt has been made to do so in this thesis.

6.3.3 Boltzmann distribution

The Boltzmann distribution is a classical thermal distribution that fits proton spectra well.

$$\frac{1}{2\pi p_T}\frac{d^2N}{dydp_T} = A_3 m_T e^{-\frac{m_0 - m_T}{T}} \tag{49}$$

6.3.4 Power law

A power law is used for pions, where the low-p_T spectrum is heavily contaminated from resonance decays. Low-p_T pions will fit well with an exponential in m_T. The high-p_T part is dominated by pQCD processes, which cause a power law tail. A power law fits the entire spectrum well. Unlike the other fit functions discussed here, the power law has three free parameters.

$$\frac{1}{2\pi p_T}\frac{d^2N}{dydp_T} = A_4(1 + \frac{p_T}{p_0})^{-n} \tag{50}$$

6.3.5 Gaussian

At forward rapidities ($y > 2.0$) in p+p $\sqrt{s} = 62.4\ GeV$, there is no hard scattering component causing the power law behavior for pions. Both pion and kaon spectra are best described by a Gaussian in p_T at these FS settings.

$$\frac{1}{2\pi p_T}\frac{d^2N}{dydp_T} = A_5 e^{-\frac{p_T^2}{B^2}} \tag{51}$$

where B^2 is $2\sigma^2$.

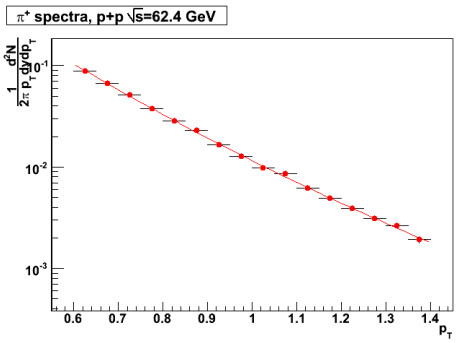

Figure 6.13: π^+ spectrum in p_T at $-0.2 < y < 0.2$, fitted with power law in the interval 0.6 $GeV/c < p_T < 1.5$ GeV/c.

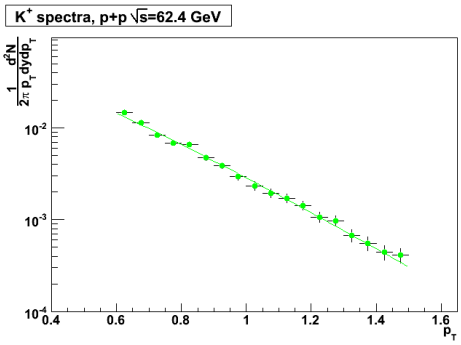

Figure 6.14: K^+ spectrum in p_T at $-0.2 < y < 0.2$, fitted with m_T exponential in the interval 0.6 $GeV/c < p_T < 1.4$ GeV/c.

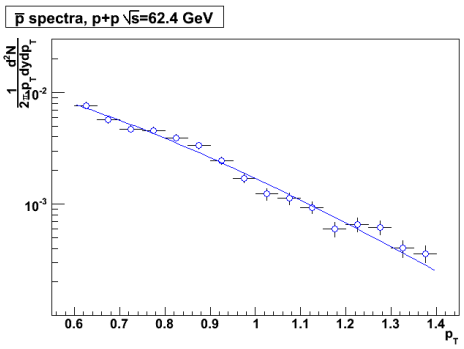

Figure 6.15: $\bar{p}$ spectrum in p_T at $-0.2 < y < 0.2$, fitted with Boltzmann distribution in the interval 0.6 $GeV/c < p_T < 1.4$ GeV/c.

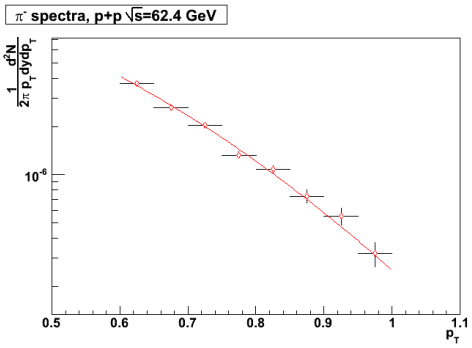

Figure 6.16: π^- spectrum in p_T at $2.85 < y < 2.95$, fitted with power law in the interval 0.6 $GeV/c < p_T < 1.0$ GeV/c. Note the change from power law to gaussian shape.

6.4 Taking like-particle ratios

Maybe the most obvious way to take a ratio between two particle species or particles and antiparticles of same species is to fit them over the same y-bin and divide the extrapolated p_T- integrated yields. Care should be taken in doing so, as 1) the fitting procedure has errors and shortcomings and 2) information is lost in the process. One solution is simply to divide the p_T spectra on each other and take the average. In this

way, one can also examine the evolution of the ratio in p_T. In many cases, the ratio is not constant in p_T and this is seen in particular closer to the fragmentation region. For consistency, all ratios in this thesis have been fitted with a constant after inspection in an interval between $p_T = [0.6, 1.5]$ GeV/c, where most of the yield seen in the well-behaved part of the acceptance resides. Away from the fragmentation region, most ratios are relatively constant within statistical error bars in this interval. The p_T dependence is most pronounced for the $\frac{\bar{p}}{p}$ ratios at forward rapidities in p+p $\sqrt{s} = 62.4$ GeV, but this ratio is very small anyway. In p+p $\sqrt{s} = 200$ GeV the ratios antiparticle/particle ratios are higher and the p_T dependence weaker within the studied acceptance interval.

6.5 Extraction of mean p_T

To extract the mean p_T of a particle distribution of p_T, the *first moment* of the distribution is taken. It is defined as

$$< p_T >= \frac{\int_{p_T Low}^{p_T High} N(p_T) p_T dp_T}{\int_{p_T Low}^{p_T High} N(p_T)} \tag{52}$$

In this thesis, the limits are $p_T High = 1.5$ GeV/c and $p_T Low = 0.0$ GeV/c. It is tricky to extract the statistical error of this quantity, so the same relative errors of the yield is simply taken and scaled to the mean p_T.

6.6 Estimation of uncertainty

It is a formidable task to estimate the systematic uncertainty of an experimental setup and a data analysis chain. Statistical uncertainties are handled by the ROOT framework utilized by BRAHMS analysis software, while systematic uncertainties must somehow be estimated. Important sources for uncertainty are:

- Choice of fit function (irrelevant for p_T-averaged ratios)
- Choice of settings
- Choice of p_T fit range (especially for pions, whose power law fit is unstable).
- Choice of rapidity fit range and bin width
- y and p_T dependance of CC correction for protons.
- Normalization uncertainty for yields

In Au+Au systematic errors of the order 10-15 % is estimated in the MRS analysis [38], and 15-20 % in the FS analysis [39]. The author believes that these are representative also for p+p data analysed, and a systematic error of 15% will be taken for the MRS points and 20% for the FS points in this thesis

7 Basic observables for p+p $\sqrt{s} = 62.4\ GeV$ and $\sqrt{s} = 200\ GeV$

After reviewing the theory of proton collisions, the experimental setup and the data analysis methods used, basic measurable quantities in p+p collisions studied in the BRAHMS experiment can be meaningfully discussed. The following chapter contain plots with fitted spectra, yields, like-particle ratios, inverse slope parameters and mean p_T for both studied CM energies. Some discussion of physics directly visible in the plots is also included. In this subchapter all points only have statistical error bars. The reason for this is twofold: First, no time was available for a thorough study of the systematic errors, and second, systematic errors are depicted in the form of gray rectangular boxes around the points. For systematic errors in the range 10-20 %,plots with multiple graphs quickly become unreadable.

7.1 Fitted hadron spectra in p_T, p+p $\sqrt{s} = 62.4\ GeV$

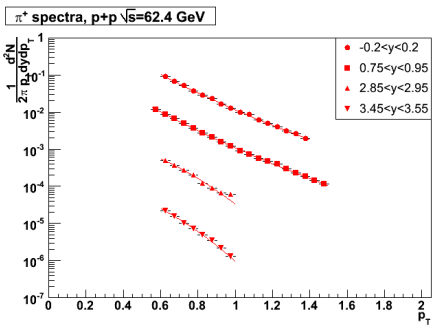

Fig 7.1: π^+ spectra in p_T

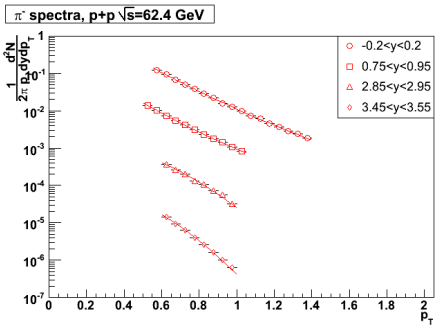

Fig 7.2: π^- spectra in p_T

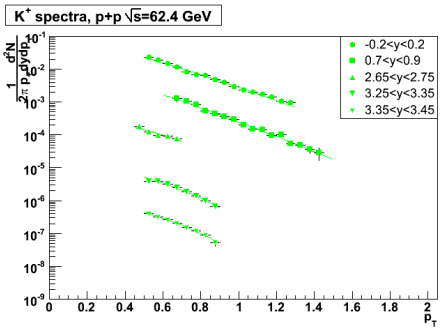

Fig 7.3: K^+ spectra in p_T

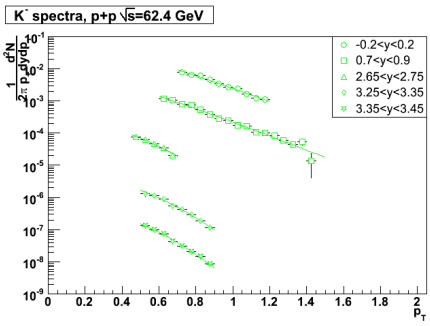

Fig 7.4: K^- spectra in p_T

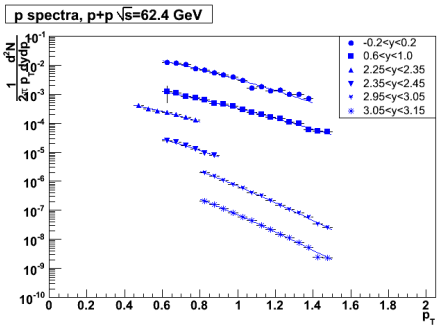

Fig 7.5: p spectra in p_T

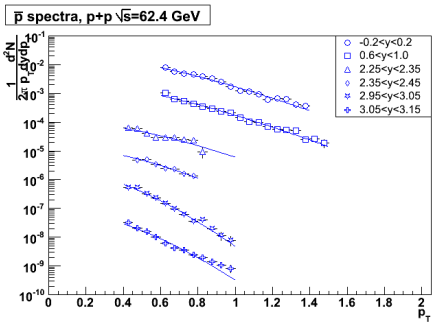

Fig 7.6: $\bar{p}$ spectra in p_T

Shown above are fitted spectra (with statistical error bars only) for all species resulting from the p+p $\sqrt{s} = 62.4$ GeV analysis. This is a thesis about soft physics and the higher p_T tails where uncertainties and statistics are not favorable, have not been included in the fits, as their contributions to the yields are minimal. The topmost spectra are not multiplied by any factor, while other spectra are offset by a multiplicative factor 0.1 from the spectra above (except $\bar{p}$ at $y = 3.0$ and $y = 3.1$, which are offset by 0.001 and 0.0001, respectively, from the topmost spectra) to increase the readability of the plot. In this plot, pions are fit with power law at midrapidity ($y \leqslant 1$ in the following discussions) and Gaussian at forward rapidity ($y > 2$; there are no settings in the region $1 < y < 2$ in this thesis). Kaons are fit with a m_T exponential in midrapidity and Gaussian in forward rapidity. Protons and antiprotons are fit with a Boltzmann distribution at all rapidities. The spectra in general appear smooth and have the expected physical behavior. For both CM energies studied, there are some differences in where optimum fits could be obtained e.g some angles where only one polarity (A/B) was available, therefore different species can have different fit ranges.

7.2 Fitted hadron spectra in p_T, p+p $\sqrt{s} = 200$ GeV

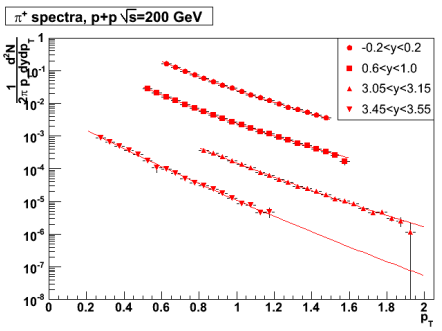

Fig 7.7: π^+ spectra in p_T

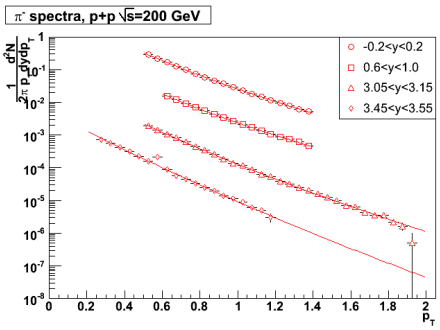

Fig 7.8: π^- spectra in p_T

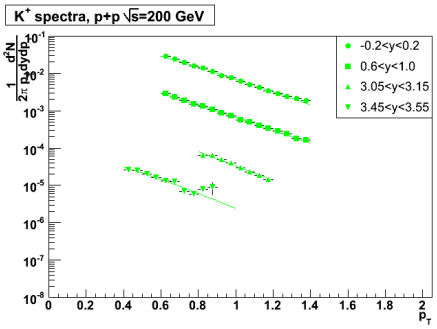

Fig 7.9: K^+ spectra in p_T

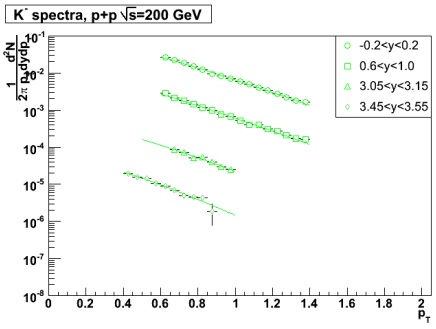

Fig 7.10: K^- spectra in p_T

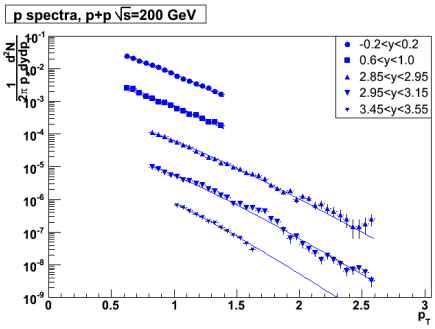

Fig 7.11: p spectra in p_T

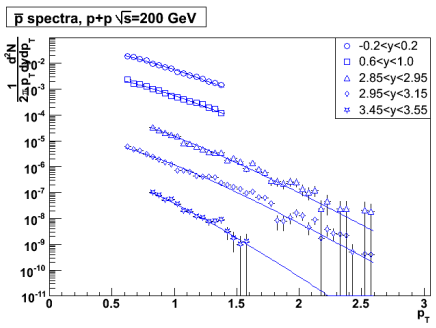

Fig 7.12: $\bar{p}$ spectra in p_T

The analysis of the p+p $\sqrt{s} = 200$ GeV data largely parallels the p+p $\sqrt{s} = 62.4$ GeV dataset. A higher beam rapidity ($y = 5.36$ vs $y = 4.20$) causes the detectors to see less of the fragmentation region, displaced by a larger midrapidity region. Spectra (with statistical error bars only) from the p+p $\sqrt{s} = 200$ GeV data are fitted with a power law for pions, m_T-exponential for kaons and a Boltzmann distribution for protons over the entire rapidity region. "Reference fits", pions fit with an m_T-exponential, have also been performed. A larger p_T-coverage with good fits for all species, resulting from higher beam energy and higher statistics than the p+p $\sqrt{s} = 62.4$ GeV dataset, is clearly visible from the plots above.

7.3 Integrated hadron yields vs y, p+p $\sqrt{s} = 62.4\ GeV$

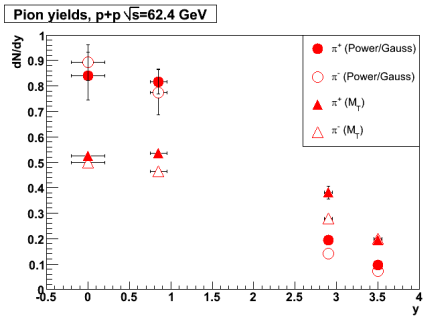

Figure 7.13: Integrated π^+ and π^- yields.

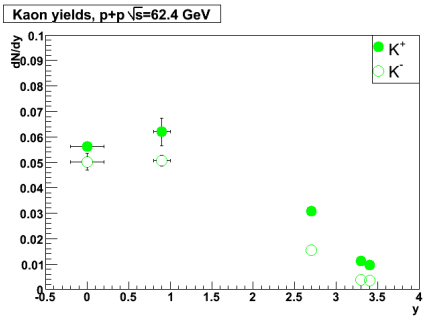

Figure 7.14: Integrated K^+ and K^- yields.

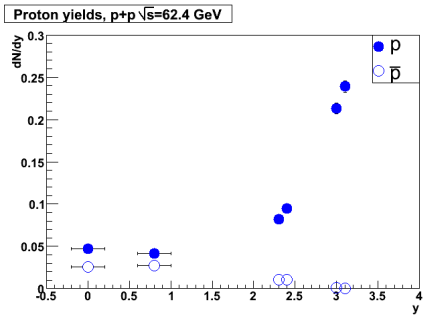

Figure 7.15: Integrated p and $\bar{p}$ yields.

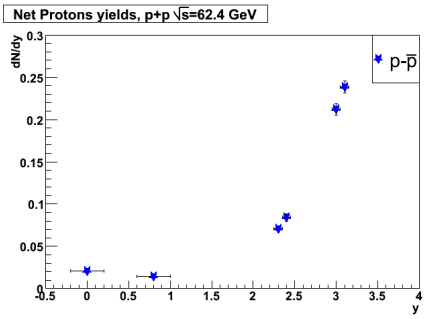

Figure 7.16: Integrated $p - \bar{p}$ yields.

Integrated yields of all species are shown, together with the net-proton distribution $\frac{dN}{dy}(p - \bar{p})$. Pions are in this plot shown with both a power law/Gaussian fit ("physical fit") and a m_T -exponential fit ("reference fit") in sligthly differnt intervals between $p_T = [0.6, 1.2]$ GeV/c. As the power law often gives a high and unstable fit for pions, this reference fit is done to ensure the sanity of the results of these analysis and to illustrate the strong sensitivity in choice of fit function for extracted yields. Also, it is needed to extract the inverse slope, the "temperature", of the distribution. The power law fit will give a higher yield than the "reference fit" in midrapidity, while in the forward rapidity, the "reference fit" gives higher yields. An approximately Gaussian shape is seen in the "physical fit" rapidity distribution consistent with a string fragmenting into mainly pions. Kaons also look approximately Gaussian in $\frac{dN}{dy}$. Protons, fit with Boltzmann distributions, have a very different behavior from the mesons. The fragmentation peak is clearly seen in forward rapidity for protons, while the antiprotons become very scarce at high rapidities. This phenomenon is highlighted by the net proton distributions, showing

even clearer the overweight of baryon number from projectiles in the fragmentation region. It is easily visible in the net proton distribution that substantial amounts of baryon number also have been transported into midrapidity, as the net-proton have a clear offset from zero (assuming that other undetected baryons have a similar distribution as the net protons). All species have a rather constant behavior at midrapidity. One should note that at 45 degree settings, particles and antiparticles have slightly different $< y >$ ($\Delta y \approx 0.1$). At $y \approx 1$ in p+p $\sqrt{s} = 62.4$ GeV, data was only taken with B settings at this angle and this seems to have caused some systematic error between positives and negatives at y in the interval $[0.6, 1.0]$. At 90 degrees in both datasets and 45 degrees in p+p $\sqrt{s} = 200$ GeV, both A and B settings were recorded, and this error is small, if even present.

7.4 Integrated hadron yields vs y, p+p $\sqrt{s} = 200$ GeV

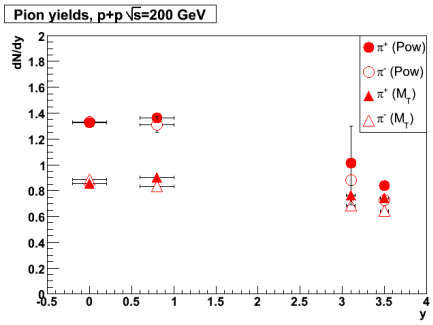

Figure 7.17: Integrated π^+ and π^- yields.

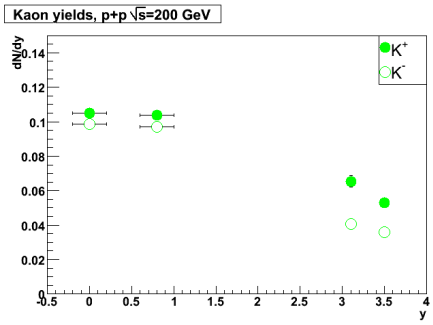

Figure 7.18: Integrated K^+ and K^- yields.

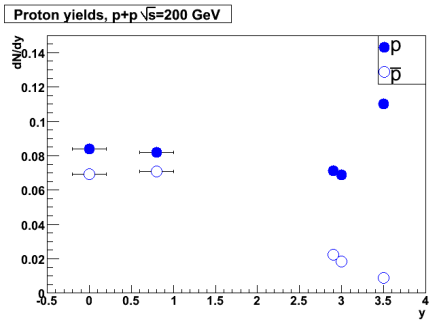

Figure 7.19: Integrated p and $\bar{p}$ yields.

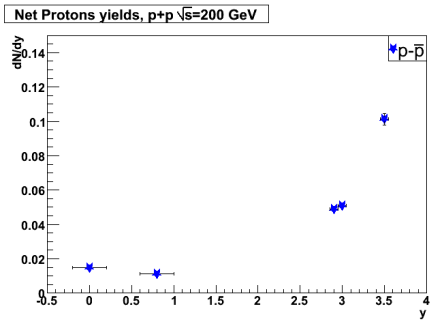

Figure 7.20: Integrated $p - \bar{p}$ yields.

From the plots above, the flat behavior in midrapidity, consistent with the Bjorken picture of an extended boost-invariant region, of a p+p collision is clearly visible. The

discussion from the p+p $\sqrt{s}$ = 62.4 GeV $\frac{dN}{dy}$ mostly applies here also, with a larger midrapidity region with constant behavior and less fragmentation region effects on yields are seen. One also sees that the proton and net proton peaks are less pronounced within the acceptance.

7.5 Like particle ratios vs p_T, p+p $\sqrt{s} = 62.4\ GeV$

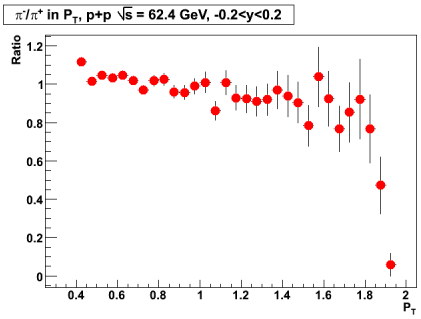

7.21: Midrapidity $\frac{\pi^-}{\pi^+}$ ratio in p_T

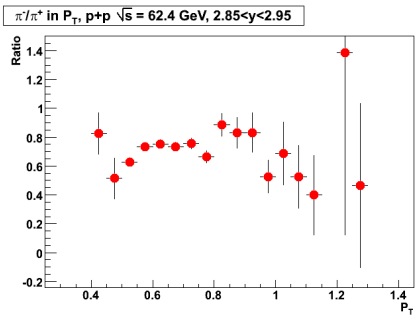

Figure 7.22: Forward rapidity $\frac{\pi^-}{\pi^+}$ ratio in p_T.

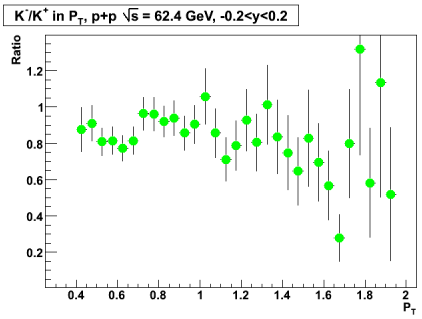

7.23: Midrapidity $\frac{K^-}{K^+}$ ratio in p_T.

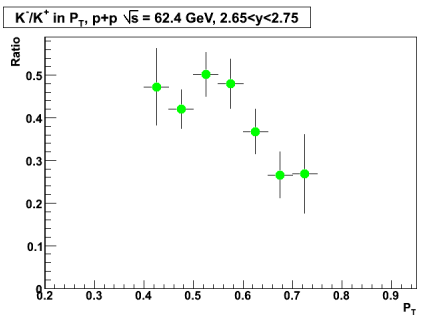

Figure 7.24: Forward rapidity $\frac{\pi^-}{\pi^+}$ ratio in p_T.

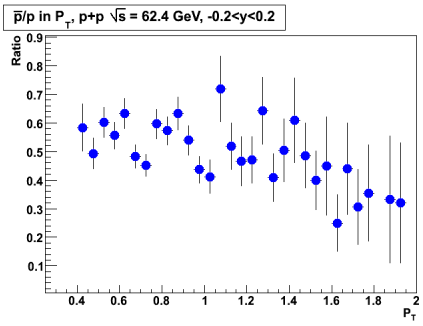

Figure 7.25: Midrapidity $\frac{\bar{p}}{p}$ ratio in p_T.

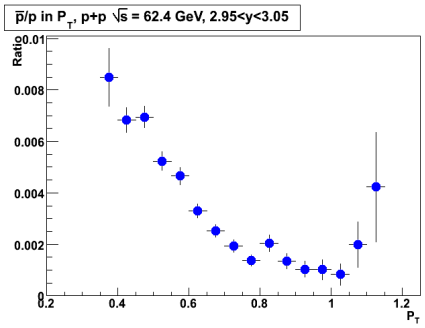

Figure 7.26: Forward rapidity $\frac{\bar{p}}{p}$ ratio in p_T.

It is clearly visible that the like-particle ratios have a near-constant behavior at $y = 0$, while all are falling at higher p_T at $y = 3$. This is a consequence of valence quark fragmentation dominating at the highest p_T values.

7.6 Like particle ratios vs p_T, p+p $\sqrt{s} = 200\ GeV$

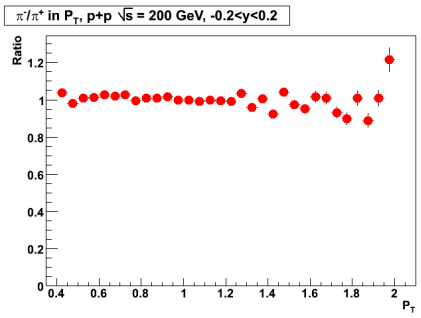

7.27: Midrapidity $\frac{\pi^-}{\pi^+}$ ratio in p_T.

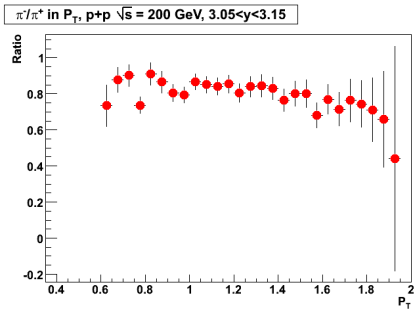

7.28: Forward rapidity $\frac{\pi^-}{\pi^+}$ ratio in p_T.

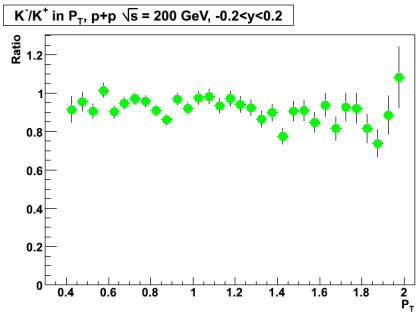

7.29: Midrapidity $\frac{K^-}{K^+}$ ratio in p_T.

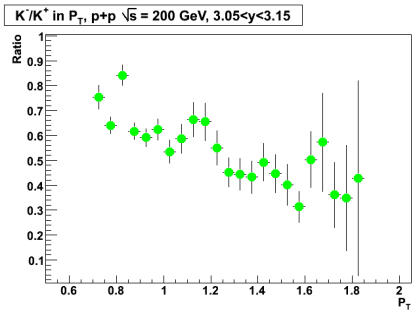

7.30: Forward rapidity $\frac{K^-}{K^+}$ ratio in p_T.

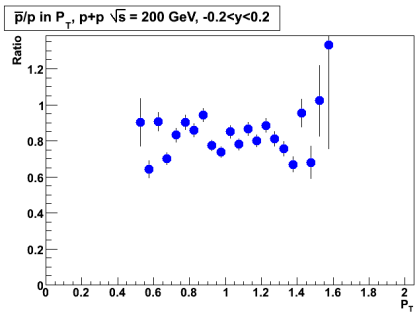

7.31: Midrapidity $\frac{\bar{p}}{p}$ ratio in p_T.

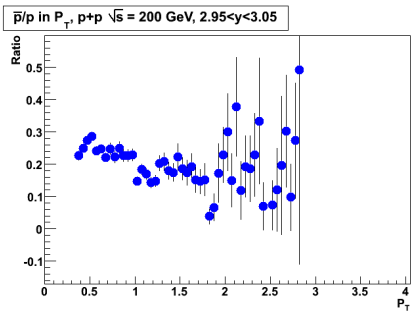

7.32: Forward rapidity $\frac{\bar{p}}{p}$ ratio in p_T.

In the higher-energy data, the ratios at $y = 0$ have an even closer to constant behavior than in the lower energy dataset. At $y = 3$, they are slightly falling in p_T, due to valence quark fragmentation. At $y = 3.5$ (not plotted), this trend is more pronounced.

7.7 Like particle ratios vs y, p+p $\sqrt{s} = 62.4\ GeV$

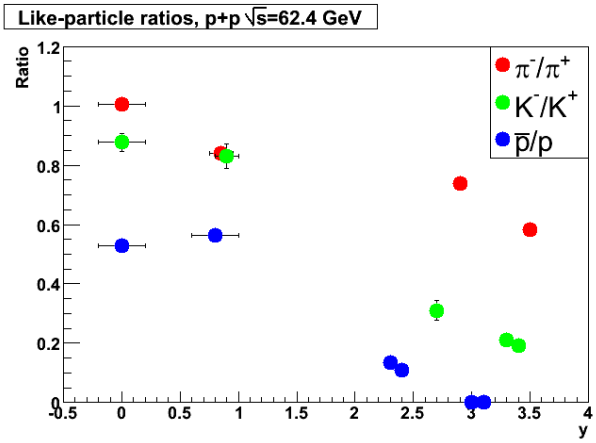

Figure 7.33: Mean of ratios in (low) p_T part of spectra projected as a function of y.

All like-particle ratios are falling at higher rapidity. The $\frac{\pi^-}{\pi^+}$ ratio is close to 1 at midrapidity, which is indicative that pair production from string fragmentation is the dominant particle production mechanism here. $\frac{K^-}{K^+}$ is about 0.9 at $y = 0$, showing that pair production is dominant also for kaons here. The $\frac{\bar{p}}{p}$ is about 0.5 at midrapidity and falling at higher y, for reasons discussed in the section above about $\frac{dN}{dy}$. The disrepancy between positive and negative pions and maybe also kaons is visible at $y \approx 1$, and an artificially low $\frac{\pi^-}{\pi^+}$ can possibly be traced to the fact that only B-polarity settings was available at 45 degrees. This causes poor overlap between π^- and π^+, as the centroids of their distributions are slightly offset from each other in y.

7.8 Like particle ratios vs y, p+p $\sqrt{s} = 200\ GeV$

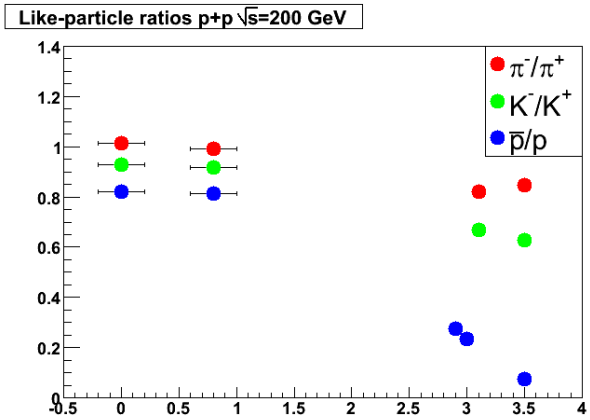

Figure 7.34: Mean of ratios in (low) p_T part of spectra projected as a function of y.

Ratios in p+p $\sqrt{s} = 200$ GeV are seen to behave analogously to p+p $\sqrt{s} = 62.4$ GeV, also here with a larger, approximately flat, midrapidity region. $\frac{K^-}{K^+}$ and $\frac{\bar{p}}{p}$ are higher at all rapidities in p+p $\sqrt{s} = 200$ GeV than in p+p $\sqrt{s} = 62.4$ GeV. These ratios are close to what seen in an earlier work on the RHIC 2001 p+p run [40].

7.9 Particle inverse slopes vs y, p+p $\sqrt{s} = 62.4\ GeV$

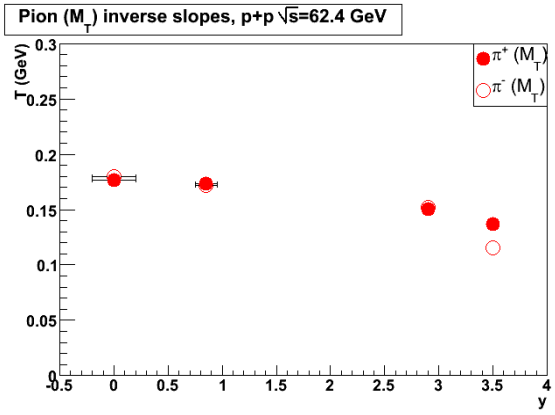

Figure 7.35: π^+ and π^- inverse slopes.

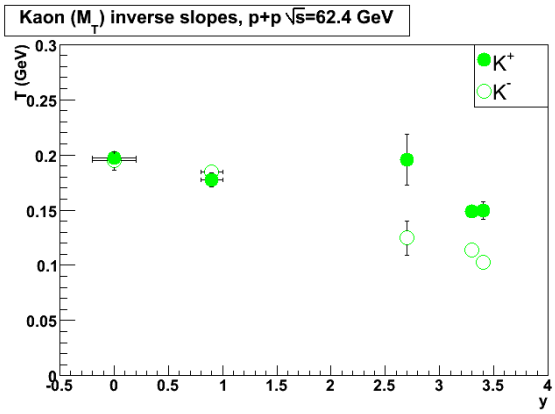

Figure 7.36: K^+ and K^- inverse slopes.

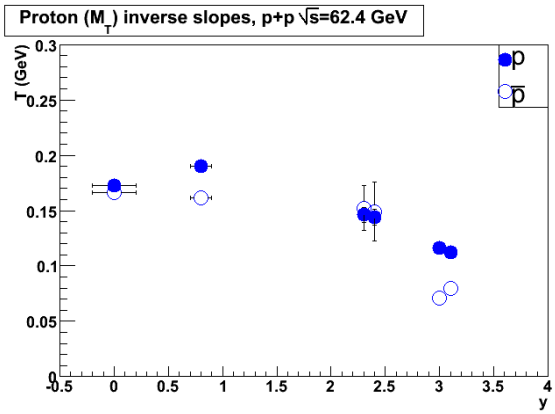

Figure 7.37: p and $\bar{p}$ inverse slopes.

For all species, the inverse slopes of their distributions are plotted. "Reference fits" with m_T- exponentials have been done for both pions and kaons at all rapidities, as the more "physical fits" as power law and Gaussian do not have a "temperature" like parameter. For the mesons, the fit is cut at higher p_T where pQCD power-like tails start to appear, while protons are fit over the same range with m_T -exponential and Boltzmann. The pions show about the same behavior for positives and negatives in the midrapidity, while at forward rapidity, the inverse slope of the negatives drop below the positives. Kaons exhibit a similar behavior, and have slightly higher inverse slopes. The protons, here fit with a m_T -exponential somewhat unexpectedly appear "colder" than the kaons. Antiprotons are also "colder" than protons at higher rapidities. This is a consequence of particles having harder spectra than antiparticles (also seen as p_T dependant like particle ratios), due to dominance of valence quarks at increasing p_T.

7.10 Particle inverse slopes vs y, p+p $\sqrt{s} = 200\ GeV$

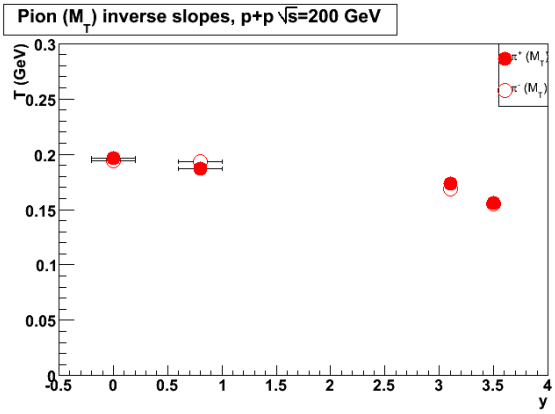

Figure 7.38: π^+ and π^- inverse slopes.

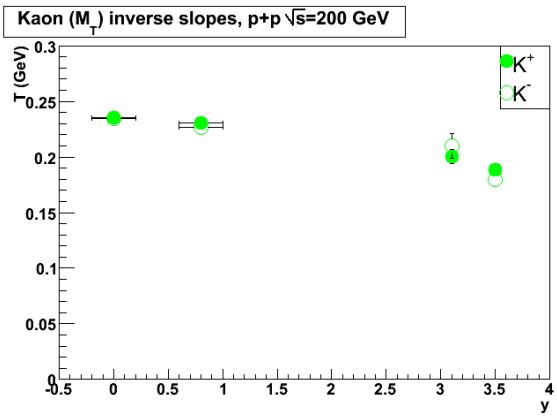

Figure 7.39: K^+ and K^- inverse slopes.

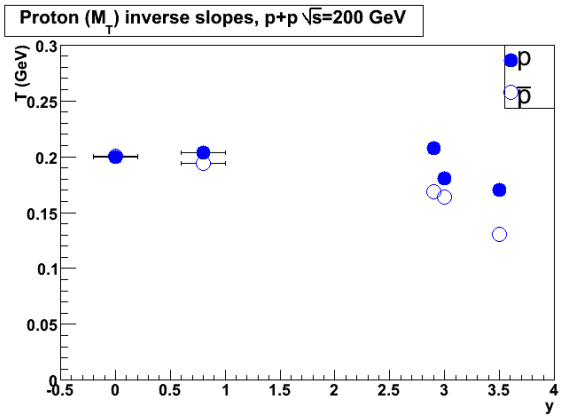

Figure 7.40: p and $\bar{p}$ inverse slopes.

In this plot, inverse slopes are shown. All fits are with m_T exponentials. It looks much like the lower energy dataset, but two features can be noted; Consistent with a more pronounced midrapidity region, even smaller variation between positives and negatives are seen than in p+p $\sqrt{s}$ = 62.4 GeV. All species also have higher inverse slopes, which should be expected from a higher beam energy.

7.11 Mean p_T, p+p $\sqrt{s} = 62.4\ GeV$

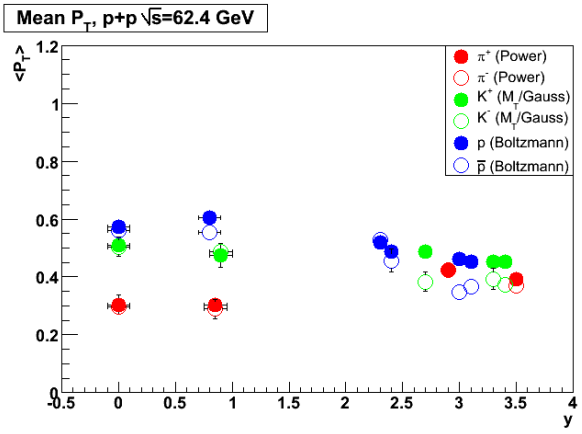

Figure 7.41: Mean p_T, all species.

The mean p_T plot is done by taking the first moment of the same distributions used in the yield plot. At midrapidity, it exhibits the usual mass hierarchy, i.e. heavier particles have a higher mean p_T. In this plot, pions are at midrapidity fit with a power law, kaons with an m_T exponential and protons with a Boltzmann distribution. At

forward rapidities, the situation is more unclear, but that is probably due to the use of Gaussians as fits for the mesons, instead of power law for pions and m_T exponential for kaons. Protons have a remarkably low p_T compared to kaons in midrapidity.

7.12 Mean p_T, p+p$\sqrt{s} = 200$ GeV

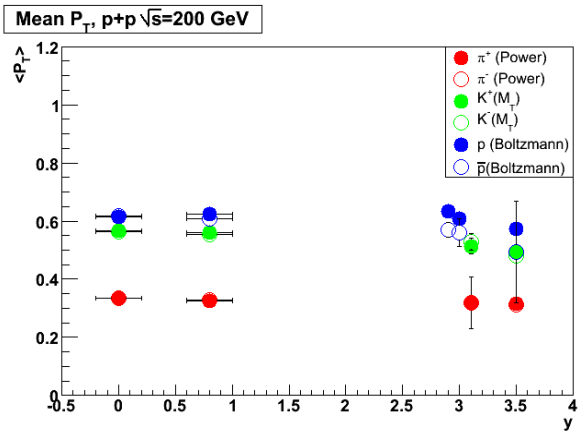

Figure 7.42: Mean p_T, all species.

The mean p_T plot in p+p $\sqrt{s} = 200$ GeV shows somewhat higher mean p_T, as expected. Also, one can see that the mean p_T is approximately constant in y, only protons and antiprotons differ somewhat at forward y. The midrapidity $< p_T >$ values are excellently in agreement with corresponding STAR results [41] for pions, while the kaon and proton $< p_T >$ values differ more than for these data. It should however be noted that star have used blast wave fits to their p+p data.

8 Systematics in p+p collisions in $\sqrt{s}$ and y

The previous chapter dealt with the direcly observable quantities at each CM energy. In the following chapter, these quantities will be compared with each other and with lower energy p+p ISR and p+p SPS data, and also with higher energy p+$\bar{\text{p}}$ TEVATRON data. The aim is to study how the system behaves over a wide range of $\sqrt{s}$, especially how midrapidity and fragmentation region physics behave at different $\sqrt{s}$.

8.1 Increase in midrapidity yields from $\sqrt{s} = 62.4$ GeV to $\sqrt{s} = 200$ GeV

Parametrization of charged particle yields at midrapidity in p+p collisions, $\frac{dN}{d\eta}|_{\eta=0}$ [42] predict $\frac{dN}{d\eta}|_{\eta=0}$ values from 1.9-2.2 for $\sqrt{s} = 62$ GeV and $2.4 - 2.8$ for $\sqrt{s} = 200$ GeV, with ratios between yields (200/62) of 1.2-1.35. Charged particle yields at midrapidity in this analysis can be found by adding the $\frac{dN}{dy}$ for all species corrected with an average Jacobian $\frac{dy}{d\eta} \approx 0.9$, gives $\frac{dN}{d\eta}|_{\eta=0} \approx 1.7$ for $\sqrt{s} = 62.4$ GeV and $\frac{dN}{d\eta}|_{\eta=0} \approx 2.7$ for $\sqrt{s} = 200$

GeV. This increase in particle production with $\sqrt{s}$ is somewhat steeper than the smooth rise displayed by p+p (p+$\bar{\text{p}}$) data from earlier experiments. Direct comparisation of identified particle yields to NA27 data (next section) and of midrapidity p_T spectra to ISR spectra (not shown here,see [43]) indicate that this work perhaps underestimates slightly the yields at $\sqrt{s} = 62.4$ GeV.

8.2 Limiting fragmentation of hadron and net proton yields

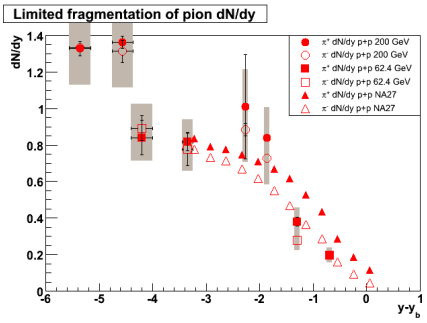

Figure 8.1: Limited fragmentation of π^+ and π^- yields.

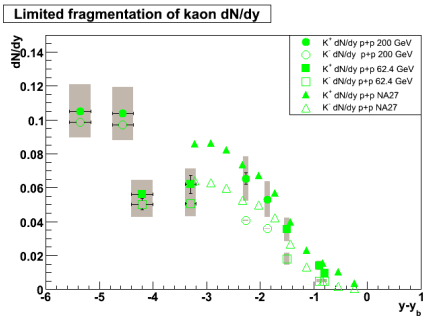

Figure 8.2: Limited fragmentation of K^+ and K^- yields.

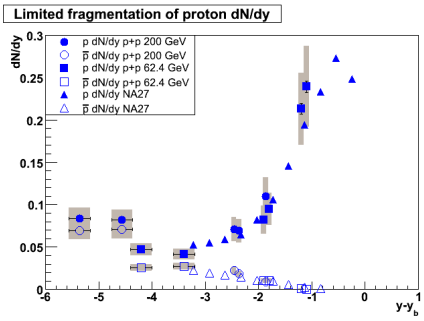

Figure 8.3: Limited fragmentation of p and $\bar{p}$ yields.

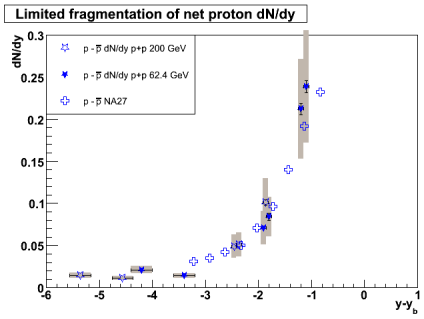

Figure 8.4: Limited fragmentation of $p - \bar{p}$ yields.

As mentioned, the expression *limited fragmentation* was introduced to denote the phenomenon that new physics in p+p collisions occurs at midrapidity, and that the fragmentation region shows a rather constant behavior at different $\sqrt{s}$.

In the plots above, $\frac{dN}{dy}$ is plotted as a function of $(y - y_{beam})$ to see whether this holds. In this thesis, limited fragmentation for ratios and yields will be checked between the two beam energies analyzed and SPS data at $\sqrt{s} = 27.5$ GeV, from the experiment NA27 [44]. It must be stated that such an analysis is prone to systematic errors between experimental setups and data analysis methods. Systematic errors (15 % in MRS and

20 % in FS) are therefore shown (the SPS data was read of a figure and the error bars was so small that they were impossible to read correctly off, therefore no error bars are shown on them). For the mesons, the plots are not so instructive. The two energies analyzed in this thesis do not overlap directly in $(y - y_{beam})$, and the SPS data taken at lower $\sqrt{s}$ seems to have relatively more mesons than this analysis. Mesons, especially pions are however prone to have unstable fits and the choice of fit function will greatly influence the yield. In the kaon plot, the lower energy BRAHMS data at midrapidity are not agreeing very well with the NA27 data, but the tendency of scaling towards beam rapidity can be seen. The proton and net proton plots are the most interesting. First, note the decline after the fragmentation peak in the NA27 data, a feature too forward to be seen in BRAHMS for the two energies studied. Second, note that $\sqrt{s} = 27.5$ GeV, 62.4 GeV and 200 GeV data match approximately in the fragmentation region, for both protons and antiprotons. This tells us that, at least for protons and antiprotons, the fragmentation region in a p+p collision shows approximately constant behavior for a fixed $(y - y_{beam})$ over an order of magnitude in $\sqrt{s}$.

8.3 Limiting fragmentation of like-particle ratios

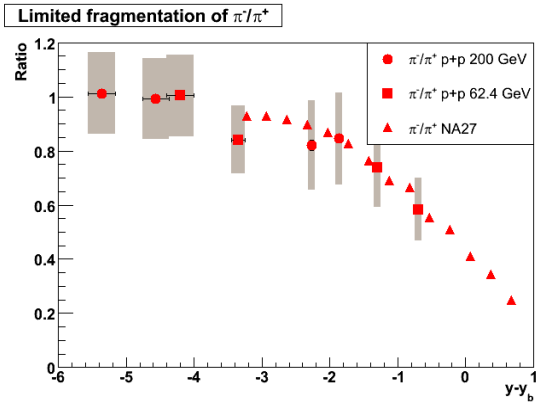

Figure 8.5: Limited fragmentation of $\frac{\pi^-}{\pi^+}$

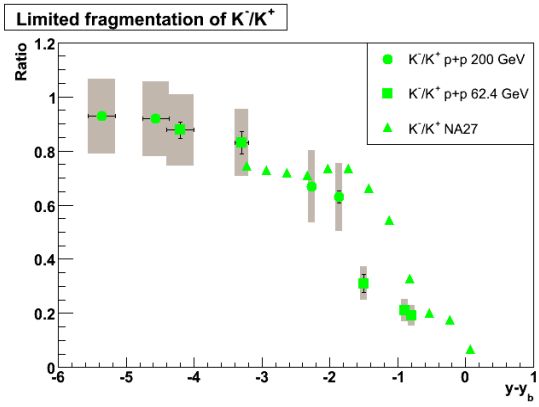

Figure 8.6: Limited fragmentation of $\frac{K^-}{K^+}$

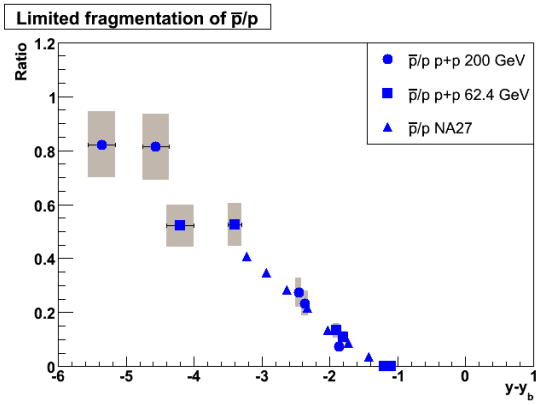

Figure 8.7: Limited fragmentation of $\frac{\bar{p}}{p}$

Systematical errors between experiments and analysis methods tend to cancel out when like-particle ratios are taken. This seems indeed to be the case for this comparisons of BRAHMS data and the NA27 data, as they agree better in ratios than the standard systematic errorbars may indicate. Both $\frac{\pi^-}{\pi^+}$, $\frac{K^-}{K^+}$ and $\frac{\bar{p}}{p}$ scales with beam rapidity. The kaon ratio from NA27 has an abrupt transition from a plateau at $\frac{K^-}{K^+} \approx 0.75$ to a steeply falling slope around $(y - y_{beam}) \approx -1.5$. ISR data at $p_T = 0.4$ GeV/c (not shown here, can be found in [45]) displays a qualitatively similar behavior. This analysis does not have rapidity coverage or precision to confirm or contradict this behavior.

8.4 Unlike particle ratios vs $\sqrt{s_{NN}}$

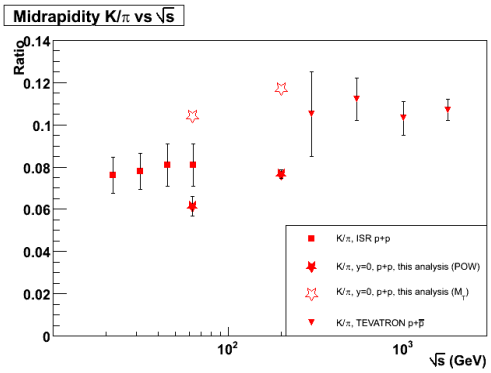

Figure 8.8: Midrapidity $\frac{K}{\pi}$ ratio at ISR, this analysis and TEVATRON. Error bars are statistical only.

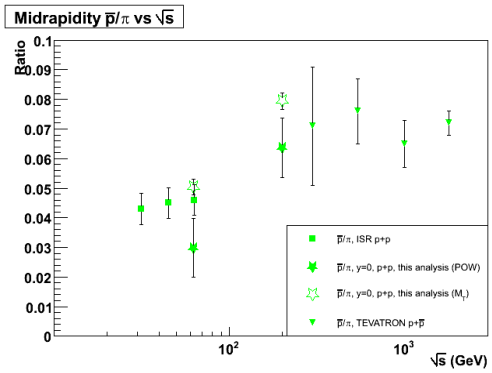

Figure 8.8: Midrapidity $\frac{\bar{p}}{\pi}$ ratio at ISR, this analysis and TEVATRON. Error bars are statistical only.

Unlike particle ratios has for this thesis only been evaluated at $y = 0$, where the integrated yields have been directly divided on each other. The integrated yields were used, as the different species can have different fit ranges and also may have strongly p_T dependant ratios. Shown above are the $\frac{K}{\pi}$ ratios and the $\frac{\bar{p}}{\pi}$ ratios (K and π averaged over positives and negatives, so $\frac{K}{\pi} = \frac{K^+ + K^-}{\pi^+ + \pi^-}$ and $\frac{\bar{p}}{\pi} = \frac{\bar{p}}{\frac{1}{2}(\pi^+ + \pi^-)}$) obtained in p+p $\sqrt{s} = 62.4$ GeV and $\sqrt{s} = 200$ GeV analysis, together with ISR p+p and TEVATRON p+$\bar{\text{p}}$ data at several different energies [46]. The plot is done both with power law and m_T exponential fit pions, where the power law is probably the most realistic fit. If the geometric mean of the these two extremes are taken, there seems to be a substantial increase of $\frac{K}{\pi}$ and (even steeper) $\frac{\bar{p}}{\pi}$ ratios, though the exact behavior is hard to tell with the error bars present and ambiguities with fit functions. At $\sqrt{s} = 200$ GeV, the $\frac{\bar{p}}{\pi}$ ratio presented by STAR in [47] (based on blast wave fits) is close to this analysis (using power law for the pions), while their $\frac{K}{\pi}$ ratio is closer to the higher estimate using a m_T exponential for the pions.

8.5 Correlation between like-particle ratios

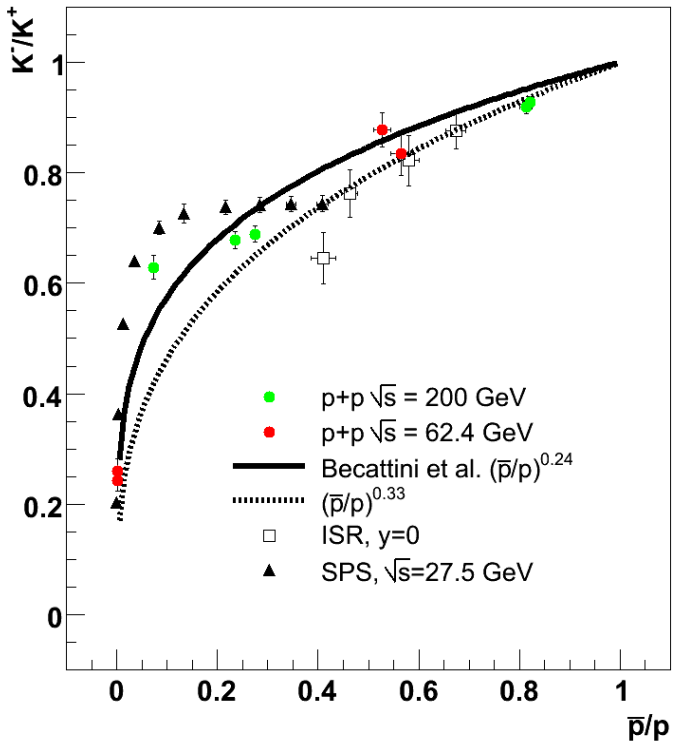

Figure 8.9: Ratio correlations in the two analysed datasets, ISR data and SPS data. Modified figure from [40].

In relativistic collisions between heavy nuclei, a *grand canonical* model well reproduces most particle ratios. Independent parameters for an isospin-neutral system are the temperature T and the baryochemical potential μ_B, while the strangeness chemical potential μ_S is fixed by conservation of strangeness. Expressing the like-particle ratios in terms of chemical potentials, the $\frac{K^-}{K^+}$ and $\frac{\bar{p}}{p}$ ratio should be strongly correlated and follow the relation

$$\frac{K^-}{K^+} = \left(\frac{\bar{p}}{p}\right)^{\alpha} \tag{53}$$

with $\alpha = \frac{\mu_S}{\mu_B}$. For not too high μ_B and high enough T (typical RHIC conditions) $\frac{\mu_S}{\mu_B} \approx$ *constant* for a given temperature. The solid curve ($\alpha = 0.24$) corresponding to $T \approx 170$ MeV describes well Au+Au data at all rapidities and SPS Pb+Pb data at least at midrapidities. The dashed curve ($\alpha = 0.33$) well reproduces midrapidity ratios from p+p collisions for RHIC, ISR and SPS energies, but does not describe the $\sqrt{s} = 27.5$ data as a function of rapidity. The data from this analysis has considerable

uncertainties and are scattered in rapidity, but seem to favour the same trend seen at lower energies with agreement with the $\alpha = 0.33$ curve for $y = 0$ and deviations away from midrapidity. It can be concluded that the grand-canonical model fails to describe the rapidity dependence of ratios in p+p, which is not suprising for such a small system.

8.6 Rough estimate of the Bjorken energy density

This analysis will end with a very speculative calculation. Mentioned in chapter 3, the Bjorken energy density is given as:

$$\epsilon = \frac{1}{\pi R^2 \tau} \frac{d\langle E_T \rangle}{dy} = \frac{1}{\pi R^2 \tau} \sum_i \langle m_T \rangle_i \frac{dN_i}{dy} \tag{54}$$

where i runs over all particle species. A proton has a radius $R_p = 0.8\ fm$ and a dimensional estimate gives a "formation time" of $c\tau_0 = 1\ fm$.The $\frac{dN}{dy}$ for all charged particles are known and $< m_T >= \sqrt{< p_T >^2 + m^2}$, where $< p_T >$ is known. Neutral pions are not detected and are assumed to be produced in equal amounts as each of the charged pions, therefore a factor $\frac{3}{2}$ is multiplied on each pion $\frac{dN}{dy}$. Also, two neutral kaons species requires a muliplicative factor of two applied on the measured charged kaon yield. Applying these formulae on both datasets results in an $\epsilon = 0.7\ GeV/fm^3$ for $p+p$ $\sqrt{s} =$ 62.4 GeV/c and $\epsilon = 1.1\ GeV/fm^3$ for $p+p$ $\sqrt{s} = 200$ GeV. In comparisation, $\epsilon_{crit} = 1.0$ GeV/fm^3, so this very speculative estimate of energy densities in p+p collisions at RHIC is actually of the order of energy densities where deconfinement in principle can occur!

9 Summary and outlook

In this thesis, identified particle production has been measured for two CM energies and compared to older experimental results. Several trends are can be seen in the results:

- Midrapidity particle production scales with approximately the parametrization between $\sqrt{s} = 62.4$ GeV and $\sqrt{s} = 200$ GeV [42].
- Particle yields and like-particle ratios as a function of y behaves as expected from the qualitative considerations in chapter 2.
- There is a significant transport of net protons from the beam rapidity to midrapidity in both datasets.
- Like-particle ratios obey limiting fragmentation over the range $\sqrt{s} = 27.5$ GeV to $\sqrt{s} = 200$ GeV. The agreement is excellent for $\frac{\pi^-}{\pi^+}$ and $\frac{\bar{p}}{p}$. It is not so clear whether our $\frac{K^-}{K^+}$ shows the same behavior as the NA27 data, with an abruptly ending plateau, or fall more gradually.
- The trends for pion and kaon yields are not so clear, but the behavior is not far from limiting fragmentation.

- Proton and net proton yields also obey limiting fragmentation, so the mechanisms of baryon transport are probably similar within this range of $\sqrt{s}$. If the net proton distribution is assumed to be similar to the distributions of undetected baryons, the degree of stopping must be about the same for these $\sqrt{s}$, with the fragmentation peaks containing most of the net baryons, being located at a fixed $(y - y_{beam})$.

- Unlike particle ratios at midrapidity are consistent with the trend shown by ISR and TEVATRON data. An increase in both $\frac{K}{\pi}$ and $\frac{\bar{p}}{\pi}$ is seen.

- Mean p_T and inverse slopes are increasing slowly with increasing $\sqrt{s}$. The expected mass hierarchy exists in $< p_T >$, while the kaon and proton inverse slopes and $< p_T >$ are closer to each other than naively expected.

- Within uncertainties, a grand-canonical statistical model for the $\frac{K^-}{K^+}$ ratio as a function of the $\frac{\bar{p}}{p}$ ratio seems to approximately describe the p+p data well at midrapidities, while the data disagrees with the grand-canonical model away from midrapidity over the studied range of $\sqrt{s}$. The behavior of the data is qualitatively reproduced in PYTHIA simulations.

- A very rough calculation of the Bjorken energy density reveals that at RHIC energies, proton collisions have sufficient energy densities to approach the energy density required for deconfinement.

If some conclusion can be drawn on basis of these results, it must be that proton-proton collisions behave similarly over a very wide range of $\sqrt{s}$. It is not quite clear whether the evolution is entirely smooth or whether "fine structure" can be found in excitation functions, for instance a flattening of kaon production above NA27 energies and a new rise between higher and lower RHIC energy. Also, the physics appearing at midrapidity at higher $\sqrt{s}$ are very interesting. It can be speculated in that the system is getting more "thermal"/"statistical" in this region than in the fragmentation region. Do we have deconfinement in a p+p collision, and if so, at which $\sqrt{s}$? Do we have flow-like phenomena in proton collisions, as the $< p_T >$ mass hierarchy first pointed out in [46] can indicate? Experimentation at the soon-running LHC will open the opportunity to study proton collisions at $\sqrt{s}$ two orders of magnitude higher than at RHIC with the dedicated heavy-ion detector ALICE. Further light can then be shed on these questions.

10 Appendix

The appendix contains three sections to contain background information that did not fit in well other places in this thesis. Section A explain kinematical quantities used, section B simply shows the standard model of elementary particles and section C provides background on how quantum electrodynamics (QED) differs from quantum chromodynamics (QCD) on a theoretical level.

10.1 Appendix A: Kinematics in relativistic collisions

The more general high-energy nuclear collision is not completely central, i.e. the nuclei only partly overlap. As the strong nuclear force has a short range of about 1 fm and a typical nucleus is up to about 7 fm, the part of the nucleus not hitting the other will just fly off. These are called the spectator nucleons. The ones involved in the collision are called the participant nucleons, and the distance between the centres of the nuclei or nucleons orthogonal to the beam direction is called the *impact parameter*, denoted b.

Another quantity much used and related to the impact parameter is the *centrality.* It related to as the area overlap between the two incoming slabs of nuclear matter, and can be expressed as a function of the impact parameter. If nuclei were disks with sharp boundaries, the formula would look like this:

$$c = \frac{\int_0^{b_c} 2\pi b db}{\int_0^{2R} 2\pi b db} \times 100\% = \frac{b_c^2}{4R^2} \times 100\% \tag{55}$$

where R is the nuclear radius and b_c is the impact parameter corresponding to centrality c.

Experimentally, nuclei are known to have a smoothly falling matter density at the edges and the centrality is usually defined from the multiplicity distribution of produced particles, since impact parameters cannot be measured directly.

$$c = \frac{\int_{Mc}^{M_{max}} P(m) dm}{\int_0^{M_{max}} P(m) dm} \times 100\% \tag{56}$$

The centrality is 0 for a fully head on collision and 1 (100%) for a grazing collision where collision partners barely touch each other. Centrality and impact parameter are more subtle quantities in a proton-proton collision, but at high enough energies, protons appear full of gluons and sea quarks and the concepts regain some of their meaning. Still, the low multiplicity in a p+p collision makes the "centrality" difficult to measure experimentally.

When heavy ion collisions are studied, variables that scale simply between different reference frames are used. At hadron colliders, the transverse momentum is much used.

$$p_T = p sin\theta \tag{57}$$

where θ is the angle relative to the beam direction. It is invariant under Lorentz transformations along the beam axis. The longitudinal momentum is then defined as

$$p_L = p cos\theta \tag{58}$$

Instead of velocity, the rapidity is used, defined as:

$$y = tanh^{-1}(\frac{v}{c}) = \frac{1}{2}\ln\frac{E + p_L}{E - p_L} \tag{59}$$

Rapidity is additive under Lorentz transformations and simple to work with. Often, $\beta = \frac{v}{c}$ is used to describe the velocity of an object, as the fraction of the velocity of light. For $\frac{v}{c} < 0.40$, $\beta \approx y$ as follows from the properties of the function $tanh^{-1}(\beta)$.

Very useful is also the pseudorapidity. It does not require the particle to be identified, only the angle of emission from vertex must be known.

$$\eta = \frac{1}{2}\ln\frac{p + p_L}{p - p_L} = -\ln(\tan\frac{\theta}{2}) \tag{60}$$

For ultrarelativistic particles where the mass can be disregarded and $E \approx p$, the pseudorapidity approaches the rapidity as seen from above equations.

Another useful variable is the transverse mass m_T. Starting from the relativistic energy

$$E^2 = p^2 + m^2 \tag{61}$$

$$p^2 = p_L^2 + p_T^2 \tag{62}$$

follows from the Pythagorean identity, we can expand the energy in longitudinal and transverse momentum

$$E^2 = p^2 + m^2 = p_L^2 + p_T^2 + m^2 = p_L^2 + m_T^2 \tag{63}$$

where the transverse mass is defined as

$$m_T^2 = p_T^2 + m^2 \tag{64}$$

The energy and the longitudinal momentum can be expressed as:

$$E = m_T sinhy \tag{65}$$

$$P_L = m_T sinhy \tag{66}$$

The Mandelstam variables are important for describing $2 \rightarrow 2$ processes. They are defined in the language of four-vectors $p_\mu = (\vec{p}, E)$.

$$s = -(p_1 + p_2)^\mu (p_1 + p_2)_\mu \tag{67}$$

$$t = -(p_1 - p_3)^\mu (p_1 - p_3)_\mu \tag{68}$$

$$u = -(p_1 - p_4)^\mu (p_1 - p_4)_\mu \tag{69}$$

where particles 1 and 2 interact and particles 3 and 4 emerge from the collision zone. s is more general than t and u and does only require two incoming particles to be defined, i.e a large number of particles can appear in the final state.

Their sum is invariant:

$$s + t + u = \sum_i m_i^2 \tag{70}$$

Mandelstam variables have not be used much in this text, however $\sqrt{s}$ will appear numerous places. It measures the total energy measured in the center-of-mass system, i.e. the theoretical upper limit of energy used for particle production.

At a stationary target accelerator:

$$\sqrt{s} = \sqrt{2m_{Target}c^2 E_{Beam}} \tag{71}$$

while at a beam-beam collider.

$$\sqrt{s} = 2E_{Beam} \tag{72}$$

A fixed target experiment will thus waste a large amount of the beam energy for even a heavy target nucleus.

10.2 Appendix B: The standard model of elementary particles

Fermions						Bosons	
Electron neutrino	υ_e	Muon neutrino	υ_μ	Tau neutrino	υ_τ	Photon	γ
Electron	e	Muon	υ	Tau	τ	Weak carriers	$W^{\pm}$, Z^0
Up quark	u	Charm quark	c	Top quark	t	Gluons	g
Down quark	d	Strange quark	s	Bottom quark	b	Higgs	h

10.3 Appendix C: QED vs QCD

For the theoretically minded reader, a short quantum field theoretical discussion of QED and QCD follows. Emphasis is put on how different symmetries cause the coupling in these theories to behave in an opposite fashion. Dramatic effects absent in QED, like asymptotic freedom and confinement, results in QCD. More theoretical details on QCD can be found in [1] or [48].

10.3.1 Lagrangian formalisms

Quantum electrodynamics was the first quantum theory to be produced. Within its reign of applicability, it has never been showed incorrect. The QED Lagrangian is obtained from applying local $U(1)_Q$ symmetry (Q denoting electromagnetic charge) on a Dirac Lagrangian, since the matter particles, electrons and positrons are fermions.

$$\mathcal{L}_{QED} = \bar{\psi}(i\gamma^\mu \partial_\mu - m)\psi - e(\bar{\psi}\gamma^\mu \psi)A_\mu - \frac{1}{4}F_{\mu v}F^{\mu v} \tag{73}$$

where ψ is a four component spinor describing electrons and positrons with spin up and down. ∂_μ is the four-divergence $(\frac{1}{c}\frac{\partial}{\partial t}, \nabla)$, γ^μ are Dirac matrices, A_μ is the vector potential and

$$F_{\mu v} = \partial_\mu A_v - \partial_v A_\mu \tag{74}$$

is the electromagnetic field tensor. $U(1)_Q$ is a commutative group and the resulting quantum field theory is Abelian. A group is commutative when the commutator of any two group operations is zero. The terms in (73) is the kinetic energy and mass terms of electrons and positrons, the interaction between the photon field and electromagnetic current and the free photon field energy. Electromagnetism is a vector force that conserves charge and flavour (but the unified electroweak force violates flavour).

The QCD Lagrangian results from applying local $SU(3)_C$ symmetry on the Dirac Lagrangian (C denotes color), as quarks are fermions. $SU(3)_C$ is a non-Abelian group, the group operations being noncommutative, in contrast with the $U(1)_Q$ symmetry of quantum electrodynamics (QED).

$$\mathcal{L}_{QCD} = \sum_{f=0}^{N_f} \left[\bar{\Psi}_f(i\gamma^\mu\partial_\mu - m)\Psi_f - g(\bar{\Psi}_f\gamma^\mu T_a \Psi_f)G_\mu^a\right] - \frac{1}{4}G_{\mu v}^a G_a^{\mu v} \tag{75}$$

where

$$G_{\mu v}^a = \partial_\mu G_v^a - \partial_v G_\mu^a - g f_{abc} G_\mu^b G_v^c \tag{76}$$

and

$$G_{\mu v}^a = \partial_\mu A_v^a - \partial_v A_\mu^a \tag{77}$$

The spinors Ψ_f are now 12-component objects describing for each flavour f quarks of three colors, spin up and down and the corresponding antiquarks, g is the color charge, γ^μ are Dirac matrices and $T_a = \frac{\lambda_a}{2}$, λ_a being the eight Gell-Mann matrices which generate $SU(3)_C$. The QCD Lagrangian have the same structure as the QED Lagrangian: A kinetic energy and mass terms for quarks, the interaction between gluon fields and quark currents and the free gluon field energy.

Most interesting is the gluon field tensor $G_{\mu v}^a$. It looks much like its electromagnetic equivalent, but the last term is new. It describes the self-interaction of gluon fields with each other. In total we have $3^2 - 1 = 8$ gauge fields, the gluon octet (a $SU(N)$ symmetric theory will have $N^2 - 1$ vector bosons). More popularly, 8 gluons carry non-neutral combinations of color-anticolor, while the 9th combination, the singlet is color neutral.

The commutators of two generators

$$[T_a, T_b] = i f_{abc} T_c \tag{78}$$

are the structure constants of $SU(3)_C$. In the QCD Lagrangian, the gluon field tensor is squared to obtain the free field energy of the gluons. Obviously, it will contain a

three-gluon term proportional to g and a four-gluon term proportional to g^2. New self-coupling gluon diagrams occur, and the force behaves completely differently from the electromagnetic force. The color force is pure vector and conserves flavour. Strong CP violation has not been observed.

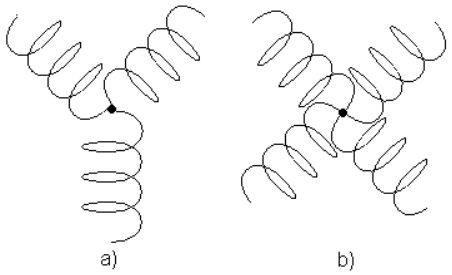

Figure 10.1: Gluon self-coupling vertices: a) Three-gluon vertex, b) Four-gluon vertex

10.3.2 Running couplings, confinement and asymptotic freedom

Due to virtual particle effects, all the coupling "constants" of the three fundamental forces, strong, weak and electromagnetic, are functions of the momentum transferred, corresponding to spatial resolution. All particles surround themselves with a cloud of virtual particle-antiparticle pairs. A "naked"/mathematical electron will set up a field and generate virtual photons around itself, which then generate virtual electron-positron pairs in the vacuum. The electron-positron pairs screen the electron charge, and the coupling is observed to be stronger when probes penetrate deeper into the cloud at higher momenta. Thus, $\alpha_{EM} = \frac{1}{128}$ at the Z_0 mass of 91.2 GeV/c^2, while it is $\frac{1}{137}$ at atomic energy scales. Electromagnetism grows stronger as momentum transfer increases.

For quarks, a similar picture could be thought to apply. A mathematical quark surrounds itself with virtual quarks and gluons. While quark/antiquark pairs shield the color charge, the self coupling of the gluons provide an antiscreening effect that turns out to be stronger than the screening. The color charge is effectively smeared out in space so a decreasing fraction of the charge is seen at higher energies, permitting the use of perturbation theory and causing quarks to scatter like free particles at high enough momentum transfers. At low energies, the coupling is getting very strong. Perturbation theory breaks down and confinement trap quarks and gluons together in colorless units. Free partons have never been discovered. This does not mean that quarks cannot be separated, but during the separation the color field energy increases. When it is energetically favourable over stretching the gluon field further to create a new quark/antiquark pair, the field energy goes into creation of a quark-antiquark pair which combine with the two already present quarks to form hadrons. From the figure below, it is seen that QED and QCD have opposite behaviours when these functions are plotted.

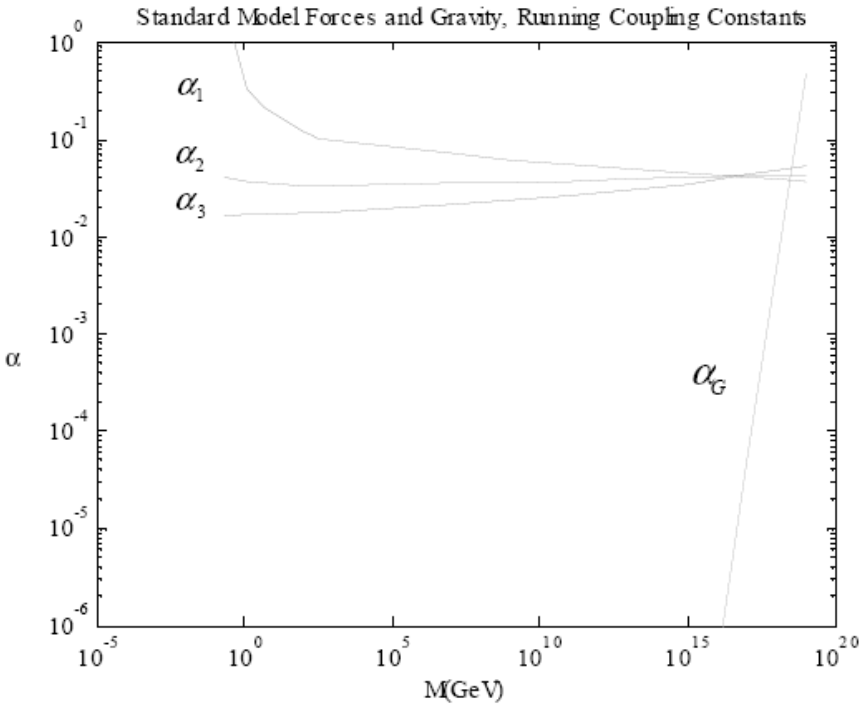

Figure 10.2: Running couplings in the standard model. α_3 is the color coupling, α_2 the weak coupling and $\alpha_1$the electromagnetic coupling. Gravity is shown as α_G. Figure from [3]

References

[1] Halzen, Francis; Martin, Alan. Quarks & Leptons: An Introductory Course in Modern Particle Physics. John Wiley & Sons (1984)

[2] C.Y Wong. "Introduction to high energy heavy ion collisions". Singapore, World Scientific (1994)

[3] D. Green: "High P_T Physics at Hadron Colliders", Camebridge University Press (2005)

[4] Particle Data Group webpage, http://pdg.lbl.gov/2005/listings/qxxx.html

[5] Tevatron Electroweak Working Group , arXiv:hep-ex/0603039v1

[6] Povh, B., Rith, K., Scholz, C., Zetsche, F. "Particles and Nuclei:An Introduction to the Physical Concepts", Springer (1999)

[7] A. Donnachie, H. G. Dosch, P. V. Landshoff and O. Nachtmann, "Pomeron Physics and QCD", Cambridge University Press, 2002

[8] A.E.Brenner, et al., Phys Rev D26 (1982) 1497

[9] G.C. Rossi & G. Veneziano, Nucl. Phys. B123(1977)507

[10] W.Thomé et al, Nucl. Phys. B129 (1977) 365.

[11] G.J. Alner, et al., (UA5), Z. Phys. C 33 (1986) 1.

[12] B.Z Kopeliovich & B.G. Zakharov, Z.Phys. C43 (1989) 241

[13] F.Videbaek & O.Hansen, Phys. Rev C52 (1995) 2684

[14] BRAHMS Collaboration, I.G. Bearden, et al., Phys. Rev. Lett. 93 (2004) 1020301; P. Christiansen, Ph.D. Thesis, University of Copenhagen, June 2003.

[15] J.Nystrand, Presentation IRTG Lecture Week, Oslo, 6-10 March 2006

[16] C. R. Allton et al, Phys. Rev. D 68, 014507 (2003) [arXiv:hep-lat/0305007]. F. Karsch, E. Laermann and A. Peikert, Phys. Lett. B 478, 447 (2000) [arXiv:hep-lat/0002003]. F. Karsch, Lect. Notes Phys. 583, 209 (2002) [arXiv:hep-lat/0106019].

[17] R.Karabowicz, Ph.D. Thesis, Jagiellonian University, (2006)

[18] J.D. Bjorken, Phys. Rev. D 27 (1983) 140;

[19] M. Gyulassy et al., "Jet Quenching and Radiative Energy Loss in Dense Nuclear Matter", in R.C. Hwa & X.-N. Wang (eds.), Quark Gluon Plasma 3 (World Scientific, Singapore, 2003).

[20] G.Løvhøiden: "Heavy Ion Collisions at High Energies".

[21] STAR Collaboration, J.Adams et al. PRL91, 072304,2003

[22] PHENIX collaboration, S.S.Adler et al. nucl-ex/0611007

[23] BRAHMS Collaboration, I. Arsene, et al., Phys. Rev. Lett. 91 (2003) 072305.

[24] RHIC homepage, http://www.bnl.gov/rhic/heavy_ion.htm

[25] BRAHMS Collaboration: I. Arsene et al: "Quark–gluon plasma and color glass condensate at RHIC? The perspective from the BRAHMS experiment", Nuclear Physics A 757 (2005) 1–27

[26] J. Adams et al. STAR Collaboration, Phys. Rev Lett 95 (2005) 122301

[27] B.B Back. et al. (PHOBOS Collaboration), nucl-ex/0407012

[28] M.C Abreau et al. (NA50 collaboration), Phys. Lett B477 (2000) 28

[29] H.Hahn et al. Nucl. Instrum. Meth., A999:245-263, 2003.

[30] M. Adamczyk et al: "The BRAHMS experiment at RHIC", *Nuclear Instruments and Methods in Physics Research A 499 (2003) 437–468*

[31] D.Ouerdane, Ph.D. Thesis, University of Copenhagen.

[32] R. Debbe et al. Nucl. Instr. Meth A570 216 (2007)

[33] I.Arsene et al, PRC 72, 014908(2005).

[34] T. M. Larsen, Master thesis, University of Oslo (2003)

[35] R. Karabowicz, Master thesis, Jagiellonian University (2002)

[36] F.Videbaek, Internal BRAHMS note:"Corrections to pp cross sections due to trigger counter acceptance", 2007

[37] B.Samset, Ph.D. Thesis, University of Oslo (2006)

[38] I.Arsene et al, Phys. Rev. C72, 014908 (2005)

[39] I.Arsene et al, nucl-ex/0610021 (2006)

[40] I.G.Bearden et al., PLB607 42-50 (2005)

[41] R.Witt et al. (STAR collaboration), J.Phys G31(2005)5863

[42] ALICE Collaboration, PPR I J.Phys G30 (2004) 1517 and references therein

[43] B.Alper et al. Nucl.Phys. B.100 (1975) 287

[44] M.Aguilar-Benitez et al. Z.Phys. C50 (1991) 405

[45] P. Capiluppi et al., Nucl. Phys B79, (1974) 189

[46] T.Alexopoulos et al.,"Mass-identified particle production in proton-antiproton collisions at $\sqrt{s}$ = 300, 540, 1000 and 1800 GeV, Phys.Rev D, volume 48, number 3, 01.08 August 1993

[47] L.Molnar et al. (STAR COLLABORATION). Poster, Quark Matter 2004, nucl-ex/0403015

[48] R.K.Ellis, W.J.Stirling and B.R Webber: "QCD and Collider Physics", Camebrigde Universty Press(1996)